

Colloidal Interactions of Quantum Dots  
in Apolar Liquids



Universiteit Utrecht

Desigend by: Marijke van Rijssel  
Printed by: Gildeprint Drukkerijen

ISBN 978-90-393-6055-2

Subject headings: Colloidal Interactions/Interface Adsorption/Self assembly/Cryo-  
TEM/AGM/Infrared Spectroscopy.

# Colloidal Interactions of Quantum Dots in Apolar Liquids

Colloïdale Wisselwerkingen van Quantum Dots in Apolaire  
Vloeistoffen

(met een samenvatting in het Nederlands)

Proefschrift

ter verkrijging van de graad van doctor aan de  
Universiteit Utrecht op gezag van de rector magnificus,  
prof.dr. G. J. van der Zwaan, ingevolge het besluit van het  
college voor promoties in het openbaar te verdedigen  
op woensdag 4 december 2013 des middags te 4:15

door

**Jozef van Rijssel**

geboren op 24 september 1986 te Utrecht

**Promotor:** Prof. dr. A. P. Philipse  
**Co-promotor:** Dr. B. H. Erné

This work is part of the research programme ‘Functional Nanoparticle Solids’ of the Foundation for Fundamental Research on Matter (FOM), which is part of the Netherlands Organisation for Scientific Research (NWO).

# Contents

Chapter 1	Introduction	1
Chapter 2	Free Energy, Enthalpy, and Entropy of Nanoparticle Association from Temperature-Dependent Cryo-TEM	21
Chapter 3	Adsorption of Nanoparticles at the Liquid/Air Interface Studied with Cryogenic Electron Tomography	43
Chapter 4	Second Virial Coefficient of Colloidal PbSe Nanoparticles	63
Chapter 5	Non-Regularized Inversion Method from Light Scattering Applied to Ferrofluid Magnetization Curves for Nanoparticle Size Distribution Analysis	87
Chapter 6	Synthesis of Monodisperse Cobalt Nanoparticles for their Self-Assembly into Binary Superlattices	111
Chapter 7	In Situ Infrared Spectroscopy of Ligand Adsorption on Colloidal Nanoparticles	129
	Summary	153
	Samenvatting in het Nederlands	157
	Dankwoord	165
	List of Publications	167
	Curriculum Vitae	169



CHAPTER 1

**Introduction**

## 1. Colloidal Nanoparticles

It is well known that the material properties of crystals become a function of size and shape when their dimensions are in the nanometer size range, 1-100 nm. Depending on the material, two mechanisms can be distinguished for the size-dependent properties [1, 2]. First, for particles of a smaller size, the fraction of surface atoms is larger, and because these atoms have a different coordination number than bulk atoms, they have different properties. These effects are visible through the decreased melting temperature of nanoparticles [2] or the presence of a non-magnetic surface layer in the case of magnetic nanoparticles [3]. The second mechanism consists of so-called quantum confinement effects, particularly present in semiconductor nanoparticles (quantum dots). These confinement effects start to play a role when the dimensions of the nanoparticle become of the same order as the exciton Bohr radius, the length scale of the spatial extension of electron-hole pairs [4]. This gives rise to size-dependent optical and electronic changes [1] such as a shift from red to blue luminescence color for CdSe nanocrystals when the particle size is decreased from 6 nm to 2 nm (see examples in ref. [4]). Both effects enable the tuning of material properties via the particle size, shape, and composition.

The tunable properties of quantum dots give rise to new applications, such as field effect transistors [5], or high density magnetic storage [6, 7]. Also in the biomedical field, nanoparticles have great potential in the treatment of cancer [8, 9] or for techniques such as magnetic particle imaging [10]. For these applications, particles are required with well-defined properties, and therefore various colloidal synthesis methods are developed that provide monodisperse nanoparticles with homogeneous properties [11, 12]. However, for use of these particles in solid-state optical and electronic applications, they typically have to be immobilized on a substrate in so-called nanoparticle solids [13]. As the nanoparticles in these solids are in close contact, the nanoparticles begin to influence each other, and as a consequence the properties of the solids are determined by their collective properties as well as those of the single nanoparticles. For example, an insulator to conductor transition is observed in compressed layers of silver nanoparticles when the particle-particle separation become small enough to enable electronic coupling between the nanoparticles [14, 15]. Similarly for magnetic particles it is reported that the magnetic properties of a solid formed from these particles depend on the structure of this solid [7]. For a good control over the properties of the solid, it is therefore necessary to control its structure and to ensure that

---



it is the same everywhere in the solid. This can be achieved by the formation of so-called nanoparticle superlattices, which resemble atomic crystals but are built from nanoparticles [16].

For a full understanding of the formation of these superlattices, the colloidal interactions between the individual nanoparticles have to be known. In this thesis, these interactions are investigated using cryogenic transmission electron microscopy (cryo-TEM), complemented by more standard colloidal techniques. In section 2 an overview of the most common colloidal interactions between nanoparticles is presented. The basics of the cryo-TEM method are discussed in section 3, and finally the scope and structure of this thesis are described in section 4.

## 2. Colloidal Interactions

A good understanding of the interactions between nanoparticles in liquid media is necessary to develop theories that describe the behavior of the nanoparticles both on a microscopic as well as on the macroscopic level [17]. Although many interactions are known that could play a role, the magnitude of these interactions is less known. In this section several possible interactions are discussed and, if possible, their interaction energy is estimated and compared with other interactions.

**2.1. Hard Sphere Interaction.** The most basic, and mainly theoretical, interaction is the hard sphere interaction potential:

$$(1.1) \quad \phi_{\text{HS}} = \begin{cases} \infty & r \leq \sigma \\ 0 & r > \sigma \end{cases}$$

Here,  $\phi_{\text{HS}}$  is the interaction energy,  $r$  is the center-to-center distance of the particles, and  $\sigma$  is the diameter of the particles. Despite its simple nature, the hard sphere interaction is sufficient to explain macroscopic phenomena such as phase behavior [18]. Several colloidal model systems have been design to approach this potential as closely as possible and were used to test the theoretical predictions [19].

**2.2. Steric Interaction.** The nanoparticles used in the experiments discussed in this thesis are dispersed in an apolar liquid. To prevent aggregation of the nanoparticles, the surface is covered with adsorbed ligands that cause a repulsion if two particles come in contact. A ligand is an amphiphilic molecule, which consists of a hydrophilic head group and one or more hydrophobic tails. The hydrophilic head group adsorbs on the nanoparticle surface, and the hydrophobic

---

tails, which mix well with apolar liquids, are on the outside of the ligand layer. The repulsion is due to an increase in the osmotic pressure of the region where the ligand layers overlap. This repulsive potential can be written as [20]:

$$(1.2) \quad \frac{\phi_{\text{Steric}}}{k_B T} = 4\pi R \Gamma^2 \frac{v_2^2}{v_1} \left( \frac{1}{2} - \chi \right) \left( 1 - \frac{r - 2R}{2\delta} \right)^2$$

Here,  $R$  is the radius of a nanoparticle,  $\Gamma$  the adsorption density of the ligands,  $v_{1,2}$  is the volume of the ligand (1) and the solvent molecules (2),  $\chi$  is the dimensionless ligand-solvent interaction parameter,  $r$  is the center-to-center distance between the particles, and  $\delta$  is the thickness of the ligand layer. The interaction parameter  $\chi$ , known from Flory-Huggins theory of polymer solubility, describes the difference between the interaction energy  $U_{LS}$  of a ligand segment with a solvent molecule and the average of the interaction energies of two ligand-segments  $U_{LL}$  and of two solvent molecules  $U_{SS}$ . If  $\chi < 1/2$ , the particles are dispersed in a good solvent and the ligand layers repel, while if  $\chi > 1/2$ , the ligand layer collapses and the stabilization of the nanoparticles is lost.

In fig. 1.1 this interaction potential is plotted using typical values for  $R = 3$  nm,  $\Gamma = 2$  nm<sup>-2</sup>,  $v_1 = 0.53$  nm<sup>3</sup> (oleic acid),  $v_2 = 0.26$  nm<sup>3</sup> (decalin),  $\chi = 0$ , and  $\delta = 1.8$  nm. For comparison, a hard sphere potential is plotted as well with an effective particle diameter equal to the experimentally observed average particle-particle separations ( $2R + 3$  nm, see chapter 2). The steric interaction between the ligands gives a strong repulsion, and the repulsive energy becomes already more than 1 k<sub>B</sub>T if the capping layers are overlapping only 0.5 nm. For most practical cases, sterically stabilized nanoparticles can be considered as hard spheres, without affecting the results significantly.

**2.3. Van der Waals Interaction.** Always present between nanoparticles is the Van der Waals interaction, originating from the interactions of the atoms in one nanoparticle with the atoms in another particle. In fact, the Van der Waals interaction is a combination of three particular types of atomic interactions, named after Keesom, Debye, and London [21]. The Keesom interaction is that between the permanent dipole moments of molecules. The second type, the Debye interaction, is that of a molecule that possesses a permanent dipole moment with an induced dipole moment in another molecule. Since the direction of induced dipole is the same as the permanent dipole, this results in an attraction between the molecules. The last type of Van der Waals interactions has a purely quantum mechanic origin, as it originates from the spontaneous fluctuations of the charge distribution in

---

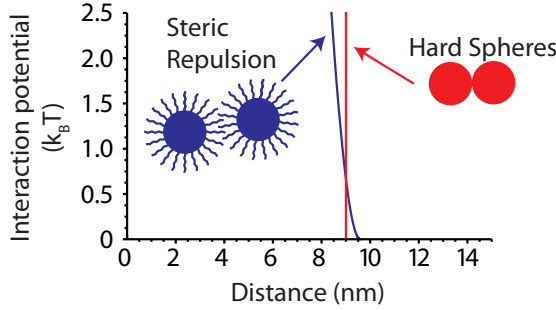


FIGURE 1.1. The interaction potential of sterically stabilized nanoparticles (for details see text). The red vertical line represents a hard sphere potential with an effective diameter to match the sterically stabilized potential.

the atom, which appears as a constantly fluctuating dipole moment. In close proximity, the charge distribution of one atom influences that of the other atom and vice versa, which gives rise to attraction. All these interactions can be written in the following mathematical form:

$$(1.3) \quad \phi_{\text{vdW}} = -C \frac{1}{r^6}$$

where the constant  $C$  is the so-called Van der Waals constant.

The Van der Waals interaction between two nanoparticles, which consist of many atoms, is given by the sum of the interactions between all atoms in one nanoparticle with those in the other nanoparticle. Assuming a continuous distribution of matter in the nanoparticles, the summation can be replaced by an integral over the volume of the particles. This integral was solved for two spheres by Hamaker giving the Hamaker potential [22]:

$$(1.4) \quad \phi_{\text{vdW}} = -A \frac{1}{6} \left( \frac{2R_1 R_2}{r^2 - (R_1 + R_2)^2} + \frac{2R_1 R_2}{r^2 - (R_1 - R_2)^2} + \ln \left[ \frac{r^2 - (R_1 + R_2)^2}{r^2 - (R_1 - R_2)^2} \right] \right)$$

Here,  $A$  is the Hamaker constant,  $R_1$  and  $R_2$  the radii of the spheres 1 and 2, and  $r$  the center-to-center distance of the spheres. The Hamaker constant is related to the Van der Waals coefficient  $C$  via:

$$(1.5) \quad A = \pi^2 \rho^2 C$$

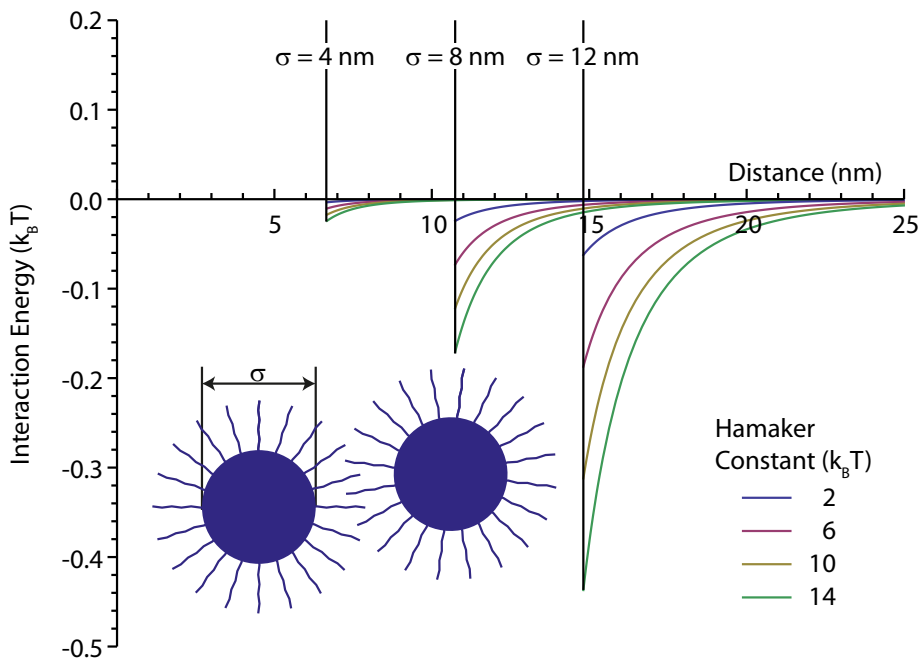


FIGURE 1.2. The Van der Waals interaction plotted as function of the center-to-center distance between the particles calculated with the Hamaker equation (eq. 1.4) for two equal-sized spheres with varying diameters and Hamaker constants. A hard sphere potential is added at the average center-to-center distance seen in experiments.

where  $\rho$  is the number density of the atoms in a nanoparticle.

This treatment of the Van der Waals interaction via integration has two shortcomings. First, it is inaccurate in the description of the interaction at small particle-particle separations, as there the discrete nature of the particles becomes important. Second, it does not take into account the interactions between more than two atoms at a time, the multi-body contributions of the interaction potential. Lifshitz derived an alternative expression for the Hamaker constant [21], where the material still was treated as continuous, such that integration remains possible, but where the many-body effects were taken into account by deriving the Hamaker constant from bulk electronic properties rather than atomic Van der

TABLE 1.1. Hamaker constants for several materials

Material	Medium	Hamaker	
		constant ( $k_B T$ )	
PbSe	Air	13	[23]
PbSe	Hexane	6	[24]
Magnetite	Hexane	5	[25]
Hexane	Air	10	[26]
Decalin	Air	15	[27]

Waals constants. In table 1.1 the Hamaker constants are listed for several materials used in this thesis. In fig. 1.2, the interaction potentials are shown for two equal-sized spheres of various diameters and Hamaker constants. A hard sphere potential is added to mimic the steric repulsion of the nanoparticles. The maximum attraction strength between the particles increases with increasing diameter and Hamaker constant but never becomes larger than  $1 k_B T$  for the investigated systems. This interaction is therefore weak and can be neglected when compared to other attractive interactions.

**2.4. Coulomb Interaction.** Although the nanoparticles are dispersed in an apolar medium, an electric charge might be present on these nanoparticles and therefore the particles might interact via a screened Coulomb potential:

$$(1.6) \quad \phi_{\text{Coulomb}} = \frac{q_1 q_2}{4\pi\epsilon_0\epsilon_1} \frac{\exp[-\kappa r]}{r}$$

where  $q_i$  is the charge of particle  $i$ ,  $\epsilon_0$  is the vacuum permittivity,  $\epsilon_1$  is the relative permittivity of the medium in which the charges reside,  $\kappa$  is the inverse Debye-Hückel screening length, and  $r$  is the distance between the charges.

The thermodynamic fraction of particles with a charge  $q = \pm e$ , can be calculated from the charging energy  $E_C$  of a dielectric sphere [28, 29]:

$$(1.7) \quad E_C = \sum_{l=0}^{\infty} \frac{e^2 (\epsilon - 1) (l + 1)}{2\epsilon_2 (\epsilon l + l + 1) R} \left(\frac{r}{R}\right)^{2l}$$

Here,  $e$  is the elementary charge,  $\epsilon = \epsilon_2/\epsilon_1$  is the ratio between the dielectric constants of the sphere ( $\epsilon_2$ ) and the medium,  $R$  is the radius of the dielectric sphere, and  $r$  is the distance from the center of the sphere to the charge. Using this relation for the charging energy and following the reasoning of Shim and

Guyot-Sionnest [29] (see chapter 4 for details), the fraction of charged quantum dots is about 1% in apolar liquids. The influence of the interactions between charged particles is therefore negligible.

**2.5. Dipole-Dipole Interaction.** The presence of dipole moments in quantum dots is an important issue because it has a great influence on both the colloidal and the electronic properties of the nanoparticles [29, 30]. The colloidal interaction between two nanoparticles with a dipole moment is described as:

$$(1.8) \quad \phi_{D-D} = k_B T \lambda \left( \frac{\sigma}{r} \right)^3 (\hat{\mu}_1 \cdot \hat{\mu}_2 - 3(\hat{\mu}_1 \cdot \hat{r})(\hat{\mu}_2 \cdot \hat{r}))$$

Here,  $\lambda$  is the coupling parameter,  $\sigma$  is the diameter of a nanoparticle,  $r$  is the distance between the nanoparticles,  $\hat{\mu}$  is a unit vector containing the orientation of the dipole moment, and  $\hat{r}$  is a unit vector that points from one particle to the other. In this formulation the interaction potential is similar for magnetic and electric dipoles, and the coupling parameter is related to the maximum interaction energy at contact via  $\phi_{max} = -2\lambda k_B T$  [31].

The presence of an electric dipole moment in nanoparticles has been shown for CdSe [29], ZnSe [29], and PbSe [30]. The latter two have a crystal lattice with a tetrahedral or cubic symmetry which cannot have an intrinsic dipole moment, and therefore the observed dipole moment has to be related to the finite size of the nanoparticle. Several models have been proposed for the origin of this dipole, like randomly placed charges on a sphere [29] or crystal facets terminated with different ions [32]. A discussion on the origin of the dipole moment taking into account the experiments presented in this thesis is given in chapter 4.

**2.6. Depletion Interaction.** For a stable dispersion of nanoparticles in an apolar liquid, the nanoparticles have to be covered with a shell of adsorbed ligands to prevent clustering and sedimentation. As the binding of these ligands is often reversible, the ligands adsorbed on the nanoparticle surface are in equilibrium with ligands in solution. These dissolved ligands can induce a depletion interaction between the particles. If a particle is dispersed in a liquid containing polymers, these polymers exert an osmotic pressure on the particles. When two particles approach each other, at some point the distance between their surfaces becomes smaller than the size of the dissolved ligands and the concentration of ligands between the particles is reduced. The osmotic pressure exerted by the ligands is now no longer uniform, but is smaller between the particles, which as a consequence

---

pushes the particles together. The strength of this interaction is given by [33]:

$$(1.9) \quad \frac{\phi_{\text{depletion}}}{\Pi} = -\frac{4}{3}\pi R_d^3 \left[ 1 - \frac{3}{4} \frac{r}{R_d} + \frac{1}{16} \left( \frac{r}{R_d} \right)^3 \right]$$

where  $\Pi$  is the osmotic pressure of the ligand solution,  $R_d$  is the depletion radius, and  $r$  is the center-to-center distance between the particles. The depletion radius is defined as the particle radius plus the thickness of the zone depleted from ligand molecules, which is equal to their radius of gyration,  $r_g$ . As a first approximation, the osmotic pressure due to the dissolved ligands can be described using the Van 't Hoff equation  $\Pi = \rho k_B T$  where  $\rho$  is the solute number density and  $k_B T$  the thermal energy.

In solution the ligand oleic acid is present in the form of dimers [34, 35] when the concentration is above the critical micelle concentration (12 mM [36]). Using typical numbers for oleic acid,  $\rho = 75 \times 10^{24} \text{ m}^{-3}$  ( $c = 250 \text{ mM}$ ) and  $r_g = 1 \text{ nm}$ , the interaction energy is  $-1.7 k_B T$ . Although the depletion attraction predicted by this model is relatively strong, this result is valid for hard spheres and non-adsorbing polymers. In this case, the surface of the nanoparticles is covered with a layer of the ligand molecules, which is known to reduce the interaction strength considerably [37]. Although an exact calculation is hard to give, it is expected that the adsorbed ligands can decrease the depletion interaction strength by an order of magnitude and therefore that depletion effects are negligible in our systems.

### 3. Quantitative Cryogenic Electron Microscopy

Electron microscopy is often used to study the nanoscale structure of materials in biology [38], polymer science [39], and physical chemistry [40, 41]. One of the greatest difficulties in the use of electron microscopy to study these structural properties of matter was the necessity of drying the sample before it could be put in the high vacuum of the electron microscope. The structure observed in the electron microscope could therefore not be directly interpreted as being representative for the situation when the sample was in the liquid state.

Originally, it was in the field of biology where the importance of this problem was most felt [42] as the presence of water is unavoidable in biological matter. Freezing of the samples was not sufficient, due to the formation of ice crystals that disturb the local structure of the sample, but cryogenic vitrification of the samples was shown to be possible [43]. In the process of vitrification the sample is cooled sufficiently fast to prevent the nucleation of ice crystals and the liquid retains its amorphous structure. This method is now utilized in all areas of structural

biology ranging from the visualization of the structures of complete cells [44] to that of the structure of single viruses [45] or even proteins [38]. Once it was shown that aqueous samples could be studied in their native state using this technique other solvents were tried as well [46]. It was shown that cryo-electron microscopy could also be utilized to study the colloidal structure of dispersed nanoparticles in a liquid, highlighting the effect of magnetic interactions [47]. The research on the assembly of colloidal nanoparticles started with the observation of the zero field structure of magnetic fluids [40, 47–49] and the influence of magnetic fields on these colloidal structures [50]. It is now possible to use this method as a quantitative measurement tool [30, 40] where thermodynamic parameters, such as the coupling free energy of two attractive nanoparticles, can be obtained from image analysis. This was first shown for magnetite [40] but was also demonstrated for non-magnetic materials, PbSe and CdSe quantum dots [30]. The possibility of quantitative analysis of the cryo-TEM images is extended in this thesis by studying the coupling of PbSe nanoparticles into dipolar chains in two dimensions and by using tomographic reconstruction obtain the sample structure in three dimensions.

Here follows a general discussion of our procedure and a demonstration of the conditions required for the acquisition of good quality cryo-TEM images. The vitrified films are prepared using a vitrobot [51] which automates the formation and subsequent vitrification of the liquid films. The vitrobot is capable of controlling the temperature and humidity of the sample chamber, which allows for a good control over the environment of the sample before vitrification. In fig. 1.3 a schematic representation of the vitrification procedure is shown. The TEM grid with the substrate, a Quantifoil® holey carbon film, is mounted between the tips of a tweezer and inserted into the vitrobot. To enhance the wettability of the carbon film by the apolar solvents, the TEM grids were first treated with an oxygen-free argon plasma for two minutes in a Fischione plasma cleaner model 1020, which reduces the hydrophilicity of the carbon film. The temperature of the sample chamber was set earlier to ensure as homogeneous a temperature as possible. For an environment with controlled vapor composition, a container loaded with the sample solvent is placed in the vitrobot, which is then closed for 15 minutes to obtain a saturated atmosphere. We did not have a method of measuring the vapor composition of the vitrobot chamber with solvent, and the equilibration time was found by optimizing the final samples. After the equilibration period, a drop of 3  $\mu\text{L}$  of the dispersion is added with a pipet on the TEM grid. The sample preparation procedure of the vitrobot is fully automated and consists of two steps. In

---



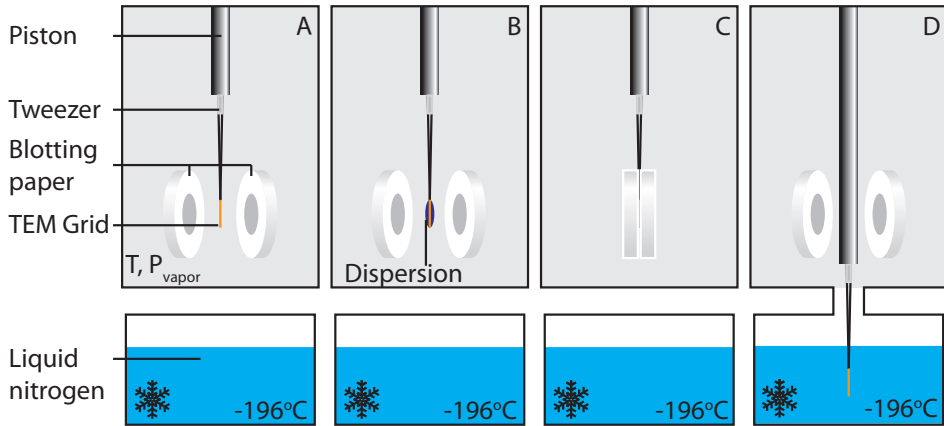


FIGURE 1.3. Overview of the vitrification procedure: (A) the vitrobot is loaded with the TEM grid and let to equilibrate at the desired temperature  $T$  and humidity  $P_{\text{vapor}}$ , (B) the sample is placed on the TEM grid, and (C) the excess liquid is blotted away. (D) The final sample is quickly immersed in a liquid nitrogen bath to vitrify the sample.

the blotting step, most of the dispersion droplet is removed with absorbent paper, and thin films of the dispersion remain in the holes of the carbon film. In the second step, the vitrification step, the TEM grid is plunged into a liquid nitrogen reservoir mounted below the vitrobot. Although liquid ethane is commonly used as coolant for cryo-TEM experiments of aqueous systems, it cannot be used for apolar liquids because these tend to dissolve in the liquid ethane; liquid nitrogen has to be used instead. Both the blotting time and the equilibration time between blotting and vitrification can be adjusted. The samples are stored in liquid nitrogen till they are inserted into the electron microscope.

The samples are placed in a Gatan 626 cryo holder and inserted in the electron microscope. In fig. 1.4 images of a typical sample are shown at different magnifications. At the lowest magnifications (fig. 1.4 A, B), the copper support of the grid is visible as black bars, and on the carbon film in between, the droplets of dispersion can be distinguished. A larger magnification of one of these droplets (fig. 1.4 C) shows holes with a diameter of  $2\ \mu\text{m}$  in the carbon film, of which some are filled with the dispersion and others are empty. In the liquid film in these holes (fig. 1.4 D-F) the PbSe quantum dots can be clearly distinguished.

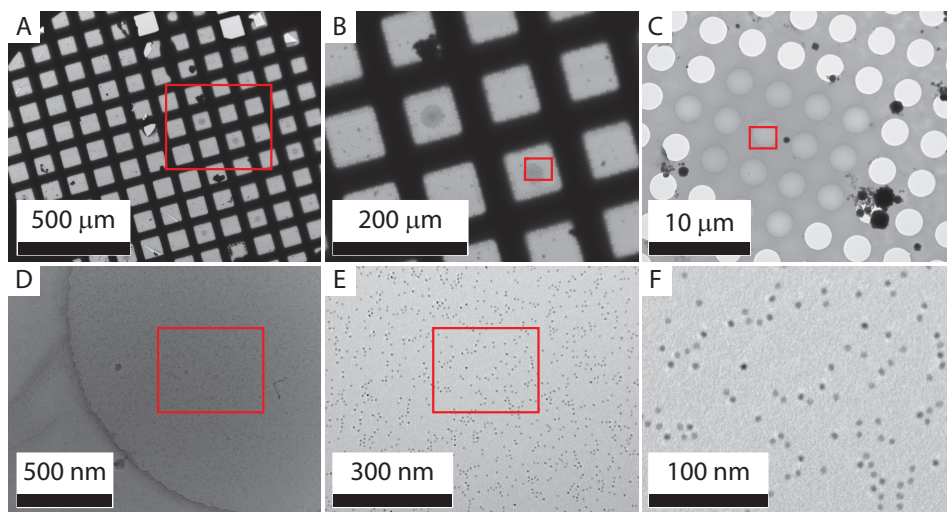


FIGURE 1.4. Images of a typical cryo-TEM sample at different magnifications showing the TEM grid as the black bars in A, via the holey carbon film in C to the single PbSe nanocrystals in F. Each red rectangle gives the approximate region of the next image.

It is of great importance that the atmosphere of the vitrobot is saturated with the solvent vapor to minimize the evaporation of the sample, which can be up to 100 nm per second for water if the atmosphere is not fully saturated [52]. Between blotting and vitrification, the sample consists of a liquid film with a thickness on the order of 100 nm; therefore if the sample atmosphere is not fully saturated, the liquid is evaporated within seconds. In fig. 1.5 TEM images of typical samples are shown with varying equilibration times and atmospheres. If no saturated atmosphere is used (fig. 1.5 A, D), all solvent has evaporated after 5 seconds. In an almost saturated environment (fig. 1.5 B, E), this process is much slower and even after 5 seconds equilibration time the dispersion is still present, although some of the solvent has evaporated, indicating that the atmosphere was not fully saturated. The liquid in the films prepared in a saturated environment was mostly in thick layers close to the copper bars and not suitable for good quality TEM images. However, increasing the blotting time from 2 seconds to 5 seconds (fig. 1.5 C) yields a very homogeneous layer throughout the grid and therefore many holes contain a vitrified film suitable for analysis. With this procedure,

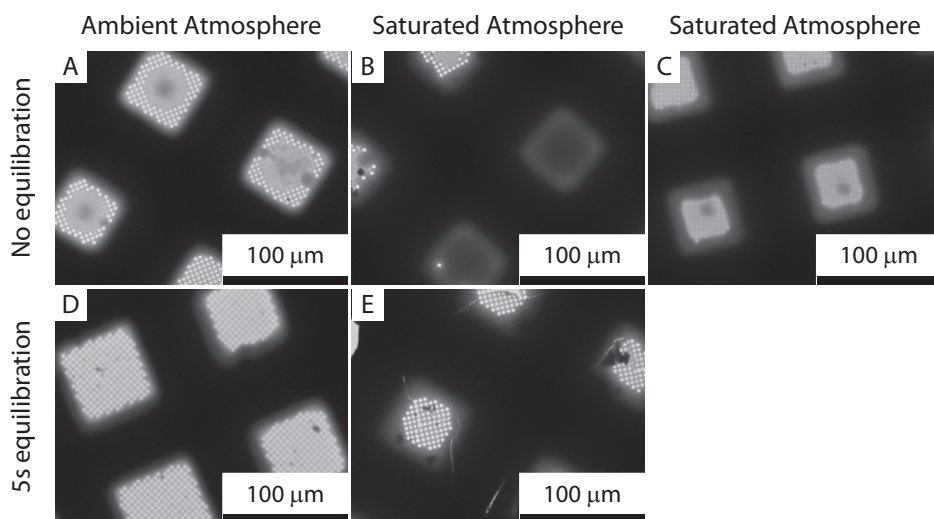


FIGURE 1.5. Typical cryo-TEM images from the same quantum dot dispersion prepared under different conditions. A and D are prepared in a nitrogen atmosphere while B, C, and E are prepared in a saturated decalin atmosphere. A-C are vitrified immediately after blotting while D and E had an equilibration time of 5 seconds.

a large number of individual films could be imaged with good quality and the analysis is performed as described in chapters 2 to 4.

To study a sample in three dimensions, electron tomography is performed, where images are acquired at different tilt angles of the sample and reconstructed to obtain the three-dimensional sample structure. At the basis of all tomographic reconstruction methods is the projection theorem, which states that the Fourier transform of a projection of a three-dimensional object equals the central slice of the Fourier transform of the complete object. Therefore, a slice through the center of Fourier space of a sample is obtained from the Fourier transform of the corresponding projection. If many projections are acquired, the sample can be reconstructed in Fourier space and finally the original object is obtained.

Several algorithms are designed for the reconstruction of the three-dimensional sample structure from two-dimensional projections [53], but here we will use the weighted back projection method (see fig. 1.6). From the object, represented as a two-dimensional image in fig. 1.6 A, projections are acquired at multiple angles,

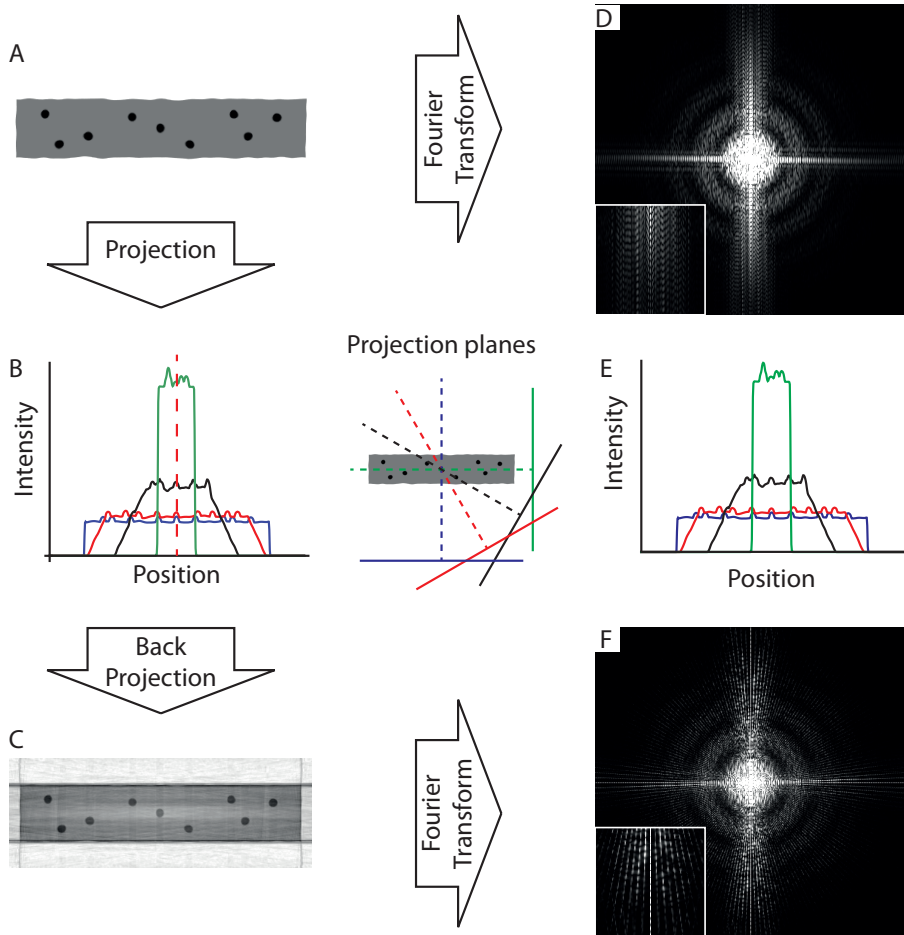


FIGURE 1.6. Basic aspects of electron tomography illustrated for a 2D image. From the image (A) one-dimensional projections (B) are obtained in different projection planes and back projection of 96 of these curves yields the original image (C). In D the Fourier transform of the original image is shown. The inverse Fourier transform of a plane in Fourier space corresponds to the projection of the image in that direction; compare the projections in B with those (E) calculated from the Fourier transform (D). The discrete nature of the reconstruction becomes clear in its Fourier transform (F) where the lines correspond to the projections used for reconstruction (see inset for a higher magnification).

for a typical experiment about 130 angles from  $-65^\circ$  to  $+65^\circ$ . These projections (fig. 1.6 B), calculated directly from fig. 1.6 A, correspond to the inverse Fourier transform from the corresponding central slices of the Fourier transform of the object (fig. 1.6 E). In the weighted back projection, the original images are convoluted with a filter and subsequently back-projected to obtain the reconstructed image (fig. 1.6 C). In the Fourier transform of the reconstruction (fig. 1.6 F), the discrete steps of the used projection angles can be clearly observed from the radial lines. The weighted back-projection algorithm takes this discrete sampling of the Fourier space into account by weighting the Fourier points proportional to their distance to the center.

Due to experimental limitations not all tilt angles can be accessed, and therefore part of the Fourier space cannot be sampled. These limitations are for example the sample holder which blocks the beam at tilt angles above  $70^\circ$  or the thickness of the sample if the transmission is too low. This is called the missing wedge problem, as it causes a wedge in the Fourier space that cannot be sampled, and this limits the observation of features perpendicular to the beam at zero tilt angle. Our samples consist of a film of the vitrified nanoparticle dispersion with the length and width larger than the field of view of the electron microscope and a thickness of approximately 100 nm. Due to the missing wedge, the interfaces of the film cannot be resolved accurately and only the particles are directly visible in the reconstructions. The interfaces of the film were determined via an indirect method based on analysis of density fluctuations in the liquid (see chapter 3).

#### 4. Outline of this Thesis

The main keywords describing the content of this thesis are interactions and nanoparticles. In the first three chapters, the interactions of nanoparticles are studied using cryogenic electron microscopy. In **chapter 2**, the interactions between PbSe nanoparticles are quantified from the concentration distribution of the self-assembled structures. The free energy of the coupling of two nanoparticles is obtained as function of quantum dot size and cluster morphology. From the temperature dependence, the entropic and the enthalpic part of the interaction are obtained. In **chapter 3**, similar samples are studied in three dimensions, and the interaction between the nanoparticles and the liquid/air interface is examined. In the last chapter with cryo-TEM, **chapter 4**, the second virial coefficient is calculated from the radial distribution functions that are obtained from the cryo-TEM

---

images. These results are compared to the second virial coefficients obtained from X-ray scattering and sedimentation equilibrium experiments.

In **chapter 5** the examined interactions are those of magnetic particles with an external magnetic field during magnetization measurements. From the response of the sample to the magnetic field, the distribution of magnetic moments is determined. Previous methods typically assumed a distribution of a specific shape, such as log-normal, and fitted the magnetization curves on that basis. The method presented here does not need such an assumption and the results therefore give an unbiased distribution of the magnetic moments.

The interactions between nanoparticles play an important role in the formation of binary superlattices. In **chapter 6** the synthesis of strongly magnetic cobalt nanoparticles is discussed and the formation of binary superlattices with PbSe nanoparticles is observed. When these superlattices are formed in the presence of a magnetic field, the magnetic nanoparticles are aligned by the magnetic field, forming magnetically aligned superstructures.

The last chapter (**chapter 7**) deals with the surfactant layer on the surface of the nanoparticles. This layer is necessary for the colloidal stability of the nanoparticles in an apolar liquid, but it also has a strong influence on for example the optical properties of the nanoparticles. Using in situ infrared spectroscopy, the binding of ligands on the surface is investigated for two cases. First, changes in the capping layer are correlated to an observed increase in photoluminescence when the quantum dot system is diluted. The second case is the measurement of the adsorption isotherm of oleic acid on magnetite and PbSe nanoparticles.

## Bibliography

- [1] A. P. Alivisatos. Perspectives on the physical chemistry of semiconductor nanocrystals. *J. Phys. Chem.*, 3654(95):13226–13239, 1996.
  - [2] E. Roduner. Size matters: why nanomaterials are different. *Chem. Soc. Rev.*, 35(7):583–92, 2006.
  - [3] R. H. Kodama. Magnetic nanoparticles. *J. Magn. Magn. Mater.*, 200(3):359, 1999.
  - [4] C. de Mello Donegá. Synthesis and properties of colloidal heteronanocrystals. *Chem. Soc. Rev.*, 40(3):1512–46, 2011.
  - [5] D. V. Talapin and C. B. Murray. PbSe nanocrystal solids for n- and p-channel thin film field-effect transistors. *Science*, 310(5745):86–9, 2005.
-

- 
- [6] C. B. Murray, D. Weller, L. Folks, and A. Moser. Monodisperse FePt nanoparticles and ferromagnetic FePt nanocrystal superlattices. *Science*, 287(5460): 1989–1992, 2000.
- [7] J. Chen, A. Dong, J. Cai, X. Ye, Y. Kang, J. M. Kikkawa, and C. B. Murray. Collective dipolar interactions in self-assembled magnetic binary nanocrystal superlattice membranes. *Nano Lett.*, 10(12):5103–5108, 2010.
- [8] Q. A. Pankhurst, J. Connolly, S. K. Jones, and J. Dobson. Applications of magnetic nanoparticles in biomedicine. *J. Phys. D: Appl. Phys.*, 36(13): R167–R181, 2003.
- [9] K.M. Krishnan. Biomedical nanomagnetism: A spin through possibilities in imaging, diagnostics, and therapy. *IEEE Trans. Magn.*, 46(7):2523–2558, 2010.
- [10] B. Gleich and J. Weizenecker. Tomographic imaging using the nonlinear response of magnetic particles. *Nature*, 435:1214, 2005.
- [11] M. V. Kovalenko, D. V. Talapin, M. A. Loi, F. Cordella, G. Hesser, M. I. Bodnarchuk, and W. Heiss. Quasi-seeded growth of ligand-tailored PbSe nanocrystals through cation-exchange-mediated nucleation. *Angew. Chem., Int. Ed.*, 47(16):3029–33, 2008.
- [12] J. V. I. Timonen, E. T. Seppälä, O. Ikkala, and R. H. A. Ras. From hot-injection synthesis to heating-up synthesis of cobalt nanoparticles: observation of kinetically controllable nucleation. *Angew. Chem. Int. ed.*, 50(9): 2080–4, 2011.
- [13] A. Sashchiuk, L. Amirav, M. Bashouti, M. Krueger, U. Sivan, and E. Lifshitz. PbSe nanocrystal assemblies: Synthesis and structural, optical, and electrical characterization. *Nano Lett.*, 4(1):159–165, 2004.
- [14] C. P. Collier, R. J. Saykally, J. J. Shiang, S. E. Henrichs, and J. R. Heath. Reversible tuning of silver quantum dot monolayers through the metal-insulator transition. *Science*, 277(5334):1978–1981, 1997.
- [15] A. Tao, P. Sinsersuksakul, and P. Yang. Tunable plasmonic lattices of silver nanocrystals. *Nature Nanotech.*, 2(7):435–40, 2007.
- [16] G. M. Whitesides and B. Grzybowski. Self-assembly at all scales. *Science*, 295(5564):2418–21, 2002.
- [17] K. J. M. Bishop, C. E. Wilmer, S. Soh, and B. A. Grzybowski. Nanoscale forces and their uses in self-assembly. *Small*, 5(14):1600–1630, 2009.
- [18] P. N. Pusey and W. van Megen. Phase behaviour of concentrated suspensions of nearly hard colloidal spheres. *Nature*, 320:340, 1986.
-

- [19] A. Vrij and R. Tuinier. *Structure of Concentrated Colloidal Dispersions*, chapter 5. Elsevier, 2005.
  - [20] E. Fischer. Elektronenmikroskopische Untersuchungen zur Stabilität von Suspensionen in makromolekularen Lösungen. *Koll. Zeit.*, 160(2):120–141, 1958.
  - [21] J. N. Israelachvili. *Intermolecular and Surface Forces*. Elsevier, Amsterdam, 2011. ISBN 9780123751829.
  - [22] H. C. Hamaker. The London-Van der Waals attraction between spherical particles. *Physica*, 4(10):1058–1072, 1937.
  - [23] J. Tang, G. Ge, and L. E. Brus. Gas-liquid-solid phase transition model for two-dimensional nanocrystal self-assembly on graphite. *J. Phys. Chem. B*, 106(22):5653–5658, 2002.
  - [24] D. V. Talapin, E. V. Shevchenko, C. B. Murray, A. V. Titov, and P. Kral. Dipole-dipole interactions in nanoparticle superlattices. *Nano Lett.*, 7(5):1213–9, 2007.
  - [25] B. Faure, G. Salazar-Alvarez, and L. Bergström. Hamaker constants of iron oxide nanoparticles. *Langmuir*, 27(14):8659–64, 2011.
  - [26] D. B. Hough and L. R. White. The calculation of Hamaker constants from Lifshitz theory with applications to wetting phenomena. *Adv. Colloid Interface Sci.*, 14:3–41, 1980.
  - [27] T. Masuda, Y. Matsuki, and T. Shimoda. Spectral parameters and Hamaker constants of silicon hydride compounds and organic solvents. *J. Coll. Interf. Sci.*, 340(2):298–305, 2009.
  - [28] L. E. Brus. A simple model for the ionization potential, electron affinity, and aqueous redox potentials of small semiconductor crystallites. *J. Chem. Phys.*, 79(11):5566, 1983.
  - [29] M. Shim and P. Guyot-Sionnest. Permanent dipole moment and charges in colloidal semiconductor quantum dots. *J. Chem. Phys.*, 111(15):6955, 1999.
  - [30] M. Klokkenburg, A. J. Houtepen, R. Koole, J. W. J. de Folter, B. H. Ern e, E. van Faassen, and D. Vanmaekelbergh. Dipolar structures in colloidal dispersions of PbSe and CdSe quantum dots. *Nano Lett.*, 7(9):2931–6, 2007.
  - [31] A. P. Philipse and B. W. M. Kuipers. Second virial coefficients of dipolar hard spheres. *J. Phys. Condens. Matter*, 22(32):325104, 2010.
  - [32] K. S. Cho, D. V. Talapin, W. Gaschler, and C. B. Murray. Designing PbSe nanowires and nanorings through oriented attachment of nanoparticles. *J. Am. Chem. Soc.*, 127(19):7140–7, 2005.
-



- 
- [33] H. N.W. Lekkerkerker and R. Tuinier. *Colloids and the Depletion Interaction*. Springer Netherlands, 2011. ISBN 978-94-007-1222-5.
- [34] D. H. Lee and R. A. Condrate. FTIR spectral characterization of thin film coatings of oleic acid on glasses: I. Coatings on glasses from ethyl alcohol. *J. Mater. Sci.*, 4:139–146, 1999.
- [35] D. H. Lee, R. A. Condrate, and W. C. Lacourse. FTIR spectral characterization of thin film coatings of oleic acid on glasses Part II Coatings on glass from different media such as water, alcohol, benzene and air. *J. Mater. Sci.*, 5:4961–4970, 2000.
- [36] V. V. Korolev, A. G. Ramazanova, and A. V. Blinov. Adsorption of surfactants on superfine magnetite. *Russ. Chem. B.*, 51(11):2044–2049, 2002.
- [37] C. M. Wijmans, E. B. Zhulina, and G. J. Fleer. Effect of free polymer on the structure of a polymer brush and interaction between two polymer brushes. *Macromolecules*, 27:3238–3248, 1994.
- [38] L. F. Kourkoutis, J. M. Plitzko, and W. Baumeister. Electron microscopy of biological materials at the nanometer scale. *Annual Rev. Mater. Res.*, 42(1):33–58, 2012.
- [39] A. L. Parry, P. H. H. Bomans, S. J. Holder, N. A. J. M. Sommerdijk, and S. C. G. Biagini. Cryo electron tomography reveals confined complex morphologies of tripeptide-containing amphiphilic double-comb diblock copolymers. *Angew. Chem. Int. Ed.*, 47(46):8859–8862, 2008.
- [40] M. Klokkenburg, R. P. A. Dullens, W. K. Kegel, B. H. Ern e, and A. P. Philipse. Quantitative real-space analysis of self-assembled structures of magnetic dipolar colloids. *Phys. Rev. Lett.*, 96(3):37203, 2006.
- [41] J. J. Crassous, M. Ballauff, M. Drechsler, J. Schmidt, and Y. Talmon. Imaging the volume transition in thermosensitive core-shell particles by cryo-transmission electron microscopy. *Langmuir*, 22(6):2403–6, 2006.
- [42] J. Dubochet. Cryo-EM-the first thirty years. *J. Microsc.*, 245(3):221–224, 2012.
- [43] J. Dubochet and J. Lepault. Cryo-electron microscopy of vitrified water. *J. Physique Colloques*, 45(C7):85–94, 1984.
- [44] M. Osumi. Visualization of yeast cells by electron microscopy. *J. Electron Microsc.*, 61(6):343–65, 2012.
- [45] G. Wang, C. Porta, Z. Chen, T. Baker, and J. Johnson. Identification of a fab interaction footprint site on an icosahedral virus by cryoelectron microscopy and x-ray crystallography. *Nature*, 355:275, 1992.
-

- [46] Y. Talmon. Transmission electron microscopy of complex fluids: the state of the art. *Ber. Bunsenges. Phys. Chem.*, 100(3):364–371, 1996.
  - [47] L. N. Donselaar, P. M. Frederik, P. Bomans, P. A. Buining, B. M. Humbel, and A. P. Philipse. Visualisation of particle association in magnetic fluids in zero-field. *J. Magn. and Magn. Mater.*, 201(1):58–61, 1999.
  - [48] K. Butter, P. H. H. Bomans, P. M. Frederik, G. J. Vroege, and A. P. Philipse. Direct observation of dipolar chains in iron ferrofluids by cryogenic electron microscopy. *Nature Mater.*, 2(2):88–91, 2003.
  - [49] K. Butter, P. H. Bomans, P. M. Frederik, G. J. Vroege, and A. P. Philipse. Direct observation of dipolar chains in ferrofluids in zero field using cryogenic electron microscopy. *J. Phys.: Condens. Matter*, 15:S1451, 2003.
  - [50] M. Klokkenburg, B. H. Ern e, J. D. Meeldijk, A. Wiedenmann, A. Petukhov, R. P. A. Dullens, and A. P. Philipse. In situ imaging of field-induced hexagonal columns in magnetite ferrofluids. *Phys. Rev. Lett.*, 97(18):185702, 2006.
  - [51] P. M. Frederik, P. H. H. Bomans, P. F. J. Laeven, and F. J. T. Nijpels. Device for preparing specimens for a cryo-electron microscope (netherlands industrial property office (ro/nl) pct/nl02/00189), 2002.
  - [52] H. Friedrich, P. M. Frederik, G. De With, and N. A. J. M. Sommerdijk. Imaging of self-assembled structures: Interpretation of TEM and cryo-TEM images. *Angew. Chem. Int. Ed.*, 49(43):7850–7858, 2010.
  - [53] J. M. Carazo, G. T. Herman, C. O. S. Sorzano, and R. Marabini. *Algorithms for Three-dimensional Reconstruction From the Imperfect Projection Data Provided by Electron Microscopy*, chapter 7, pages 217–244. Springer, New York, 2005.
-

## CHAPTER 2

# Free Energy, Enthalpy, and Entropy of Nanoparticle Association from Temperature-Dependent Cryo-TEM

### ABSTRACT

Quantum dots form equilibrium structures in liquid dispersions, due to thermodynamic forces that are often hard to quantify. Analysis of these structures, visualized using cryogenic electron microscopy, yields their formation free energy. Here we show that the nanoparticle interaction free energy can be further separated into the enthalpic and entropic contributions, using the temperature dependence of the assembly structures. Monodisperse oleic acid capped PbSe nanoparticles dispersed in decalin were used as a model system, and the temperature-dependent equilibrium structures were imaged by cryo-TEM, after quenching from different initial temperatures. The interaction enthalpy and entropy follow from Van 't Hoff's exact equation for the temperature dependence of chemical equilibria, now applied to associating nanoparticles. The enthalpic component determines the magnitude of the contact interaction, which is crucial information in understanding the energetics of the self-assembly of nanoparticles into ordered structures.

## 1. Introduction

Nanoparticles of inorganic materials differ in their optical, electrical, and magnetic properties from bulk phase, and by self-assembly into ordered structures, new materials can be prepared with properties derived from those of the nanoparticles [1].

Fundamental aspects of the self-assembly process are of great current interest, in particular the effect of interactions between nanoparticles [2], but often quantitative information is missing. Contributions to the interactions between nanoparticles include Van der Waals dispersion interactions, electrostatic interactions between net nanoparticle charges, interactions between permanent electrical or magnetic dipoles, and sterical interactions due to absorbed organic capping layers [3, 4]. Theories are available to calculate the effects of those interactions [5], but experimental data for the magnitude of the interactions between nanoparticles is scarce. We propose to determine the contact interaction of nanoparticles dispersed in a liquid environment from image analysis of equilibrium association structures. The size of such structures not only depends on the coupling energy of interacting nanoparticles, but also on the effects of nanoparticle coupling on rotational and translational entropy. This is why our approach is to perform temperature-dependent analysis of equilibrium assemblies, to separate the enthalpic and entropic effects of the coupling of two nanoparticles.

To measure the interaction enthalpies of colloidal particles, calorimetry might also be used [6]. However, the determination of number densities of interacting species in colloidal systems is a challenge. For example, reversible dimerisation of nanoparticles can be detected using analytical ultra-centrifugation [7], but resolving separate monomer and dimer concentrations is hardly feasible; the same holds for techniques like light and neutron scattering. We therefore use cryogenic transmission electron microscopy (cryo-TEM) [8] to obtain images of the particle positions in vitrified films of a liquid dispersion. This method has been used to image different types of nanoparticles, for example silica [9], gold [10], magnetite [11], and PbSe and CdSe quantum dots [12]. Although the feasibility of temperature-dependent cryogenic imaging was demonstrated for systems of molecular liquid crystals [13], no previous attempt has been made to study the temperature dependence of nanoparticle clusters.

---

## 2. Experimental

**2.1. Synthesis of PbSe Nanoparticles.** The cryo-TEM experiments were performed on PbSe quantum dots (QDs) synthesized according to the method described by Houtepen et al. [14] with slight modifications. The method is based on the co-injection of Pb and Se precursors in di-phenyl ether (DPE 99%, Aldrich) at high temperature and under inert, nitrogen atmosphere. Pb-precursor was prepared by dissolving 1.7 mmol of lead acetate trihydrate (99.999% Aldrich) in a mixture of 1.5 mL oleic acid (OA, 90% Aldrich), 8 mL of trioctyl phosphine (TOP, 90% Fluka), and 2 mL DPE. This solution was heated at about 120°C under low pressure ( $10^{-3}$  bar) for about 2 hours and then purged with nitrogen at room temperature. A 1 M Se-precursor was prepared by dissolving 0.31 g (3.9 mmol) of Se powder (99.999% Alfa Aesar) in 4 mL of TOP. Next, 1.7 mL of the Se-precursor solution was mixed with the PbSe precursor solution and rapidly injected into a hot bath containing 10 mL DPE at 190°C. Soon after injection, the temperature dropped to about 140-150°C and the solution was kept at this temperature for 1.5 to 20 minutes, to obtain oleic acid capped particles with diameters varying from 5 nm to 12 nm. The reaction was finally quenched by injecting a mixture of 20 mL butanol (99.8% Aldrich) and 10 mL methanol (99.8% Aldrich). Separation of the QDs and purification from unreacted species and excess surfactant were performed by two cycles of precipitation by methanol addition, centrifugation, and redispersion in toluene (99.8% Aldrich). Due to the better vitrification properties of decalin, the nanoparticles were transferred from toluene to decalin by evaporating the toluene under nitrogen flow and redispersing the particles in cis/trans-decalin (98% Merck).

**2.2. Cryogenic Transmission Electron Microscopy.** In a thermostatted Vitrobot [15] 3  $\mu$ L of an approximately 0.4  $\mu$ M QD dispersion was placed on a QuantiFoil TEM grid with 2  $\mu$ m holes. Excess fluid was removed using absorbent paper, resulting in a film with a thickness of a few particle diameters, after which the film was vitrified using liquid nitrogen. We emphasize here that the films were freestanding, without any substrate material above or below the liquid film in the visualized parts of the sample. TEM images of the freestanding films in the 2  $\mu$ m holes were acquired on a Philips Tecnai 12 transmission electron microscope (120 keV) making use of a liquid nitrogen cooled Gatan 626 cryo-holder.

**2.3. Image Analysis.** The so obtained images of the vitrified films (fig. 2.1) clearly show the presence of small assemblies in the liquid dispersion. Using IDL

---

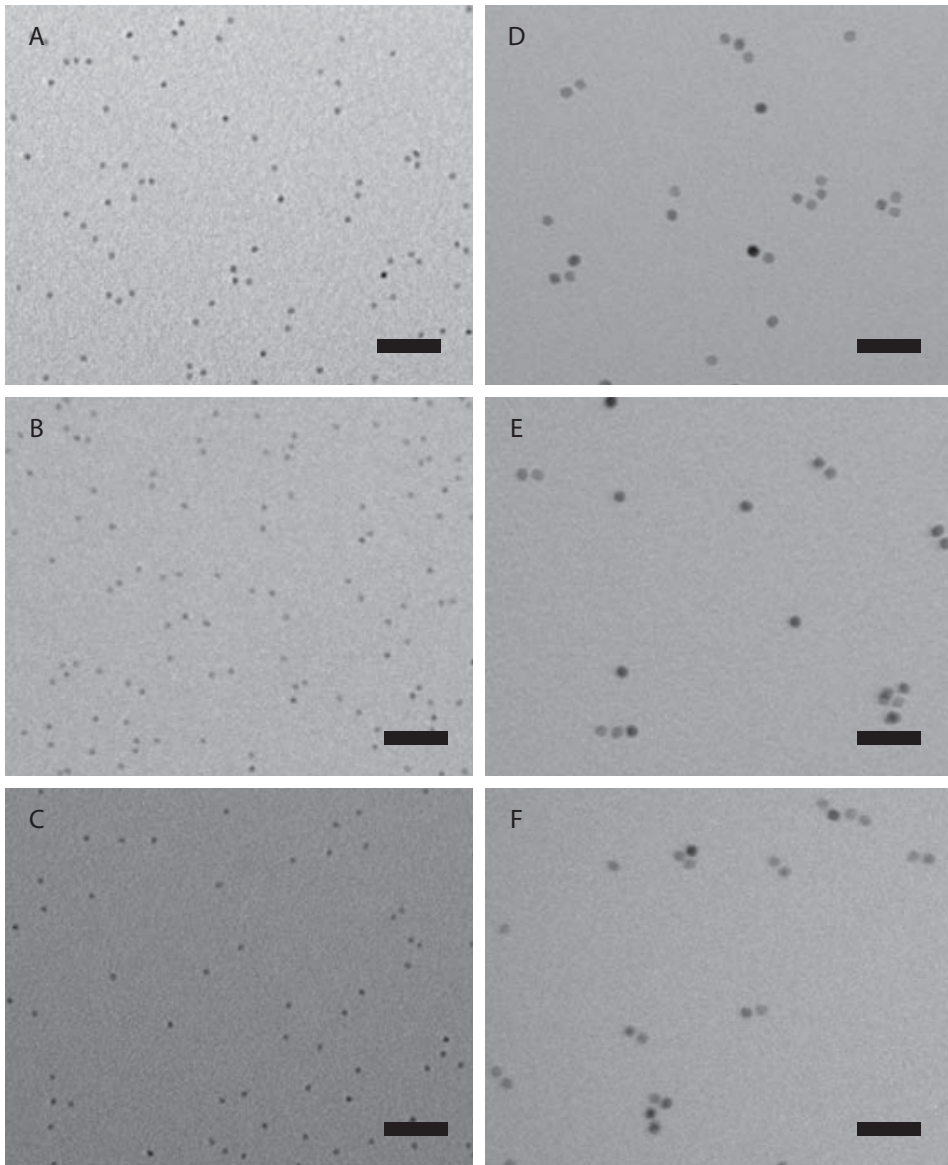


FIGURE 2.1. Representative cryo-TEM images of vitrified films showing structure formation of PbSe quantum dots with average diameters of 6 nm (A-C) and 11 nm (D-F) dispersed in decalin at 10°C (A,D), 20°C (B,E), and 40°C (C,F). The scale bars are 50 nm in each image.

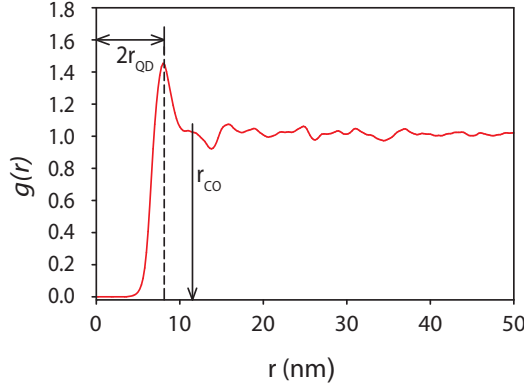


FIGURE 2.2. Radial distribution function of an image containing  $\sim 1700$  quantum dots with a core diameter of 6 nm dispersed in decalin. The arrows show the effective QD diameter ( $2r_{\text{QD}}$ ) and the cut-off distance ( $r_{\text{CO}}$ ) used to distinguish between neighboring and non neighboring particles.

7.0 analysis software (ITT Visual Information Solutions, Boulder, Colorado), the particle coordinates were determined from these images. To characterize the typical separation distances between the particles, the radial distribution function was calculated using:

$$(2.1) \quad g(r) = \frac{1}{\rho 4\pi r^2 dr} \left\langle \sum_{j \neq i} \delta(\mathbf{r}_i - \mathbf{r}_j - r) \right\rangle_i$$

with  $\rho$  the average number density of the system and  $\mathbf{r}_{i,j}$  the position of particle  $i$  or  $j$ . The radial distribution function is the particle number density at a distance  $r$  of particle  $i$  scaled to the average number density of the system. This is measured by counting the number of particles in a shell between  $r$  and  $r + dr$  and dividing that by the number density  $\rho$  and the volume of the shell  $4\pi r^2 dr$ . Particles are part of the same cluster if their center-to-center distance is less than a certain cut-off distance, defined as the far side of the main peak in the radial distribution function  $g(r)$ , see fig. 2.2.

The surface fractions of the chains,  $\phi_n$ , are defined as:

$$(2.2) \quad \phi_n = \frac{A_{\text{QD}} n N_n}{A_{\text{Im}}}$$

where  $A_{\text{QD}}$  is the cross-sectional area of a quantum dot,  $N_n$  the number of chains with length  $n$ , and  $A_{\text{Im}}$  the total area of the cryo-TEM image.  $A_{\text{QD}}$  is defined as a disk with a diameter  $2r_{\text{QD}}$  equal to the nearest neighbor distance obtained from the  $g(r)$ , shown in fig. 2.2. The approximately 3 nm spacing between two particles at this equilibrium distance is less than two times the length of the capping molecules ( $2 \times 2$  nm), indicating a partial overlap between the capping layers of the two nanoparticles. By defining the effective particle diameter this way, we compensate for the permeability of the capping layer.

### 3. Results

**3.1. Room Temperature Observations using Cryogenic Electron Microscopy.** For the interpretation of cryo-TEM images as snapshots of the nanoparticle configurations before vitrification of the film, the quenching time has to be much shorter than the typical diffusion time in the system. The quenching time is defined as the time it takes to cool down from the initial temperature to temperatures below the melting point of the solvent. In the literature, vitrification rates up to  $10^6 \text{ Ks}^{-1}$  are reported for  $1 \mu\text{m}$  thick aqueous samples [16]. For our experimental system, quenching times of 1 ns can be achieved theoretically (appendix 2.A) much shorter than the 500 ns self-diffusion time of 4 nm QDs, the smallest particles considered in this chapter, indicating that particle diffusion is negligible during vitrification.

This preservation of high temperature configurations during quenching was also demonstrated by Crassous et al. [17] in the case of particles consisting of a polystyrene core and a thermal sensitive poly(N-isopropylacrylamide) shell. Upon quenching from different initial temperatures, the shell thickness decreased with increasing temperature and the radii of the particles determined from TEM were in good agreement with those determined from dynamic light scattering.

Another illustrative example of the conservation of high-temperature structures during the quenching process is by Frederik et al. [18] who showed the structure of intermediate species present in the phase transition in lipid assemblies. These intermediate species are only present in a narrow temperature window around the phase transition temperature and therefore provide a good illustration of the temperature-dependent structure conservation in cryo-TEM.

Together these illustrations and calculations show that cryo-TEM images are indeed representative for the situation at the temperature before vitrification and that thermodynamic quantities can be extracted.

---



**3.2. Coupling Free Energy of Nanoparticle Clusters.** To obtain the coupling free energy from the distribution of cluster morphologies, we consider the equilibrium between single particles ( $A_1$ ) and clusters of  $n$  particles ( $A_n$ ):



In a thermodynamic equilibrium, the change in the Gibbs free energy  $\Delta G$  is by definition zero:

$$(2.4) \quad \Delta G = \sum_{i=0}^N \mu_i \nu_i \equiv 0$$

where  $\mu_i$  is the chemical potential of species  $i$  and  $\nu_i$  the stoichiometric coefficient in the reaction equation. For an equilibrium between separate particles and a cluster of  $n$  particles, this results in:

$$(2.5) \quad n\mu_1 = \mu_n$$

Here, the monomers are nanometer sized spherical quantum dots dispersed in an apolar liquid. Because of the size difference between the nanoparticles and the solvent molecules, the chemical potential depends on the volume fraction  $\phi$  rather than the mole fraction [19, 20] (for details see appendix 2.B):

$$(2.6) \quad \mu_n = \mu_n^0 + k_B T \ln(\phi_n)$$

From eqs. 2.5 and 2.6 we can derive an expression relating the ratio of the different cluster morphologies to the difference in standard free energies of these clusters:

$$(2.7) \quad \frac{\phi_n}{\phi_1^n} = \exp\left(-\frac{\Delta G^0}{k_B T}\right); \quad \Delta G^0 = \mu_n^0 - n\mu_1^0$$

The above relation is generally valid, such that the free energy difference between any two cluster morphologies can be calculated from the ratio of the volume fractions of these clusters. This analysis does not take specific pair interactions into account, and therefore the obtained interaction parameters are the sum of all interactions present in the system. To compare the data from our cryo-TEM experiments with this theory, first the free energy difference of only linear chains is examined, clearly the dominant conformation (see fig. 2.1). As our primary interest is the pair formation free energy, the total formation free energy is written as:

$$(2.8) \quad \Delta G^0 = (n-1)\Delta G_2^0$$

assuming the contribution of each bond in a chain to be  $\Delta G_2^0$ , namely the formation free energy of a dimer. This equation neglects the influence of non-nearest

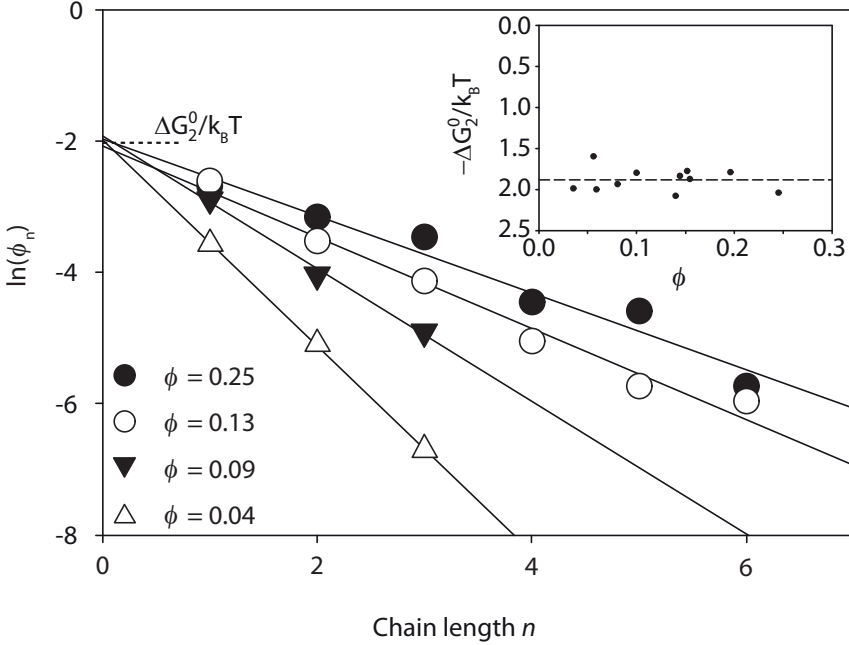


FIGURE 2.3. Chain length distribution plots of different cryo-TEM images of PbSe QDs, dispersed in decalin, with a diameter of 6 nm at different total surface fractions,  $\phi$ . The inset shows the contact free energy as function of surface fraction.

neighbors, which can contribute 10 to 20 % for long-range dipolar interactions [21]. However, the so obtained interaction free energy can be used as an experimental effective free energy that can be compared with an effective free energy obtained from theoretical interaction models. From eqs. 2.7 and 2.8 it follows that:

$$(2.9) \quad \ln(\phi_n) = n \left( \ln(\phi_1) - \frac{\Delta G_2^0}{k_B T} \right) + \frac{\Delta G_2^0}{k_B T}$$

This equation predicts that the natural logarithm of the surface fraction of chains depends linearly on their length,  $n$ , with the y-intercept determined by  $\Delta G_2^0$ . Confirmation of eq. 2.9 also demonstrates that the observed clusters are indeed equilibrium clusters.

In fig. 2.3 the chain length distribution (CLD) plots are shown for different concentrations of 6 nm PbSe QDs; each CLD is calculated from a single image containing 300 to 2000 nanoparticles. Although we started from the same initial

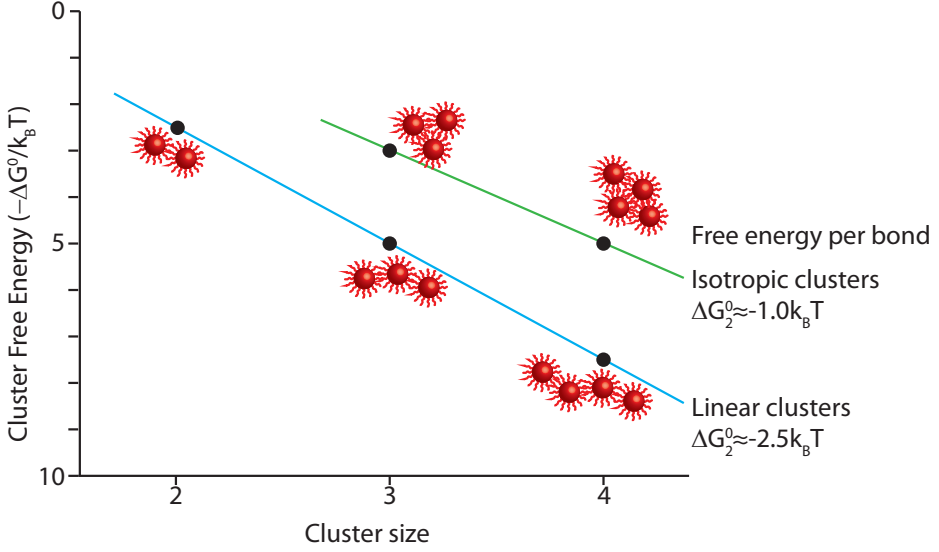


FIGURE 2.4. The total free energy for different cluster morphologies

dispersion in all experiments, the final surface fractions can be very different, partly due to evaporation of the solvent before vitrification (fig. 1.5). Therefore we use the surface fraction of each image as the surface fraction of the thermodynamic system. The linear dependence of  $\ln(\phi_n)$  predicted by eq. 2.9 is clearly observed; the contact free energy follows accordingly from a linear fit of the data. The contact free energy is constant in the observed range from 4% to 25% surface coverage, as shown in the inset of fig. 2.3, which confirms that all samples are in thermodynamic equilibrium. The average coupling free energy,  $\Delta G_2^0$ , is  $-1.8 \pm 0.13 \text{ k}_B\text{T}$ , and the scatter in the data ( $\sim 0.5 \text{ k}_B\text{T}$ ) is indicative of the uncertainty in the measured free energy for a single image. For the 11 nm QDs, a contact free energy of  $-5.0 \pm 0.3 \text{ k}_B\text{T}$  was found.

**3.3. Orientation-Dependent Cluster Free Energy.** In fig. 2.4 the free energy difference between pure monomers and different cluster configurations is shown. Similar as in eq. 2.8, the total cluster free energy is written as the product of the number of bonds in a cluster  $b$  times a constant free energy per bond  $\Delta G_2$ :

$$(2.10) \quad \Delta G^0 = \Delta G_2^0 b$$

For linear clusters, the number of bonds in the cluster is equal to  $n - 1$  where  $n$  is the number of particles, and eq. 2.10 reduces to eq. 2.8.

The number of bonds for isotropic clusters is higher than that of linear clusters. A linear cluster of three particles has two bonds, whereas an isotropic cluster of the same size has three bonds. Similar for a cluster of four particles, the linear and isotropic clusters have three and five bonds, respectively. Although eq. 2.10 predicts a lower cluster free energy for the isotropic clusters, for PbSe nanoparticles the linear clusters have a lower cluster free energy. From this we have to conclude that the particle-particle interaction has a strong anisotropic component. The nature of this anisotropy is discussed in section 3.5.

**3.4. Entropy and Enthalpy of the Nanoparticle Interactions.** The temperature dependence of the free energy is given by the Van 't Hoff equation [22]:

$$(2.11) \quad \frac{d \ln(K)}{d(1/T)} = \frac{d\Delta G^0}{d(1/T)} = \frac{-\Delta H^0}{k_B},$$

where  $k_B$  is the Boltzmann constant,  $T$  the absolute temperature, and  $\Delta G^0$ ,  $\Delta H^0$ , and  $\Delta S^0$  are the changes in, respectively, the Gibbs free energy, enthalpy, and entropy for a reaction under standard conditions. The interaction enthalpy can thus be determined from the slope of a plot of the coupling free energy as function of  $1/T$ , the so-called Van 't Hoff plot. The Haber synthesis of ammonia is a classical example [23] where  $\Delta H^0$  follows from a linear Van 't Hoff plot. Equation 2.11 is an exact thermodynamic relation [22] which is also valid when  $\Delta H^0$  and  $\Delta S^0$  are temperature dependent, resulting in a non-linear Van 't Hoff plot. Due to this generality, the Van 't Hoff equation is not restricted to chemical equilibria, including those involving biomolecules [24], but should also apply to the thermodynamic self-assembly of colloids and nanoparticles.

The CLD-plots of PbSe QDs (fig. 2.5) show that the contact free energy decreases with increasing temperature. Each temperature-dependent  $\Delta G_2^0$  is based on 10 images, about 10000 particles in total. Provided that  $\Delta H_2^0$  and  $\Delta S_2^0$  are temperature independent, the Van 't Hoff equation (eq. 2.11) predicts a linear dependence between the interaction free energy and the inverse temperature, which agrees well with the measured free energies, see inset of fig. 2.5. A linear fit of the data yields for PbSe QDs with a diameter of 6 nm,  $\Delta H_2^0 = -3.9 \pm 0.7 \text{ k}_B\text{T}$  and  $T\Delta S_2^0 = -1.9 \pm 0.7 \text{ k}_B\text{T}$ ; for a diameter of 11 nm we find  $\Delta H_2^0 = -6.4 \pm 1.1 \text{ k}_B\text{T}$  and  $T\Delta S_2^0 = -1.4 \pm 1.0 \text{ k}_B\text{T}$ . The uncertainty in the values of the interaction free energy is smaller than the symbols used in the inset of fig. 2.5 and the uncertainty

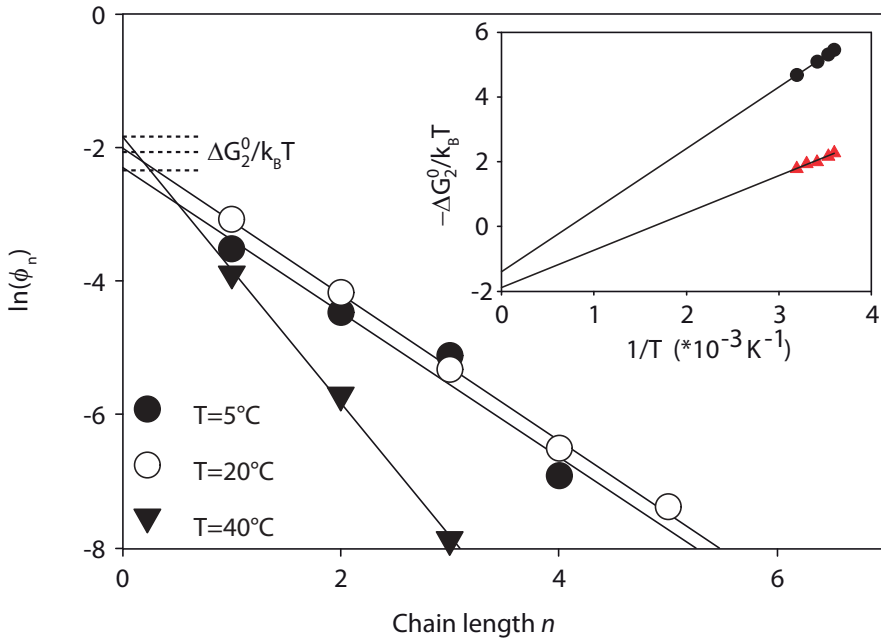


FIGURE 2.5. Chain length distribution plots for different temperatures. In the inset, the contact free energy is plotted as function of inverse temperature for PbSe QDs with a diameter of 6 nm (triangles) and 11 nm (circles) dispersed in decalin.

in the values of the enthalpy and entropy is mainly due to the extrapolation of the Van 't Hoff plot.

The value of  $\Delta S_2^0$  can be compared to the following theoretical prediction, based on the change in the number of degrees of freedom due to the coupling of a particle to a chain. Before coupling, there is a chain which, in two dimensions, has one rotation and two translational degrees of freedom and there is a single particle which has two rotational and two translational degrees of freedom. After coupling, a single chain with one rotational and two translational degrees of freedom remains, so the system loses in total 4 degrees of freedom in this coupling reaction. As follows from the equipartition theorem, each degree of freedom contributes with  $0.5 k_B$  to the entropy, resulting in a net entropy change of  $-2 k_B$ , which is of the same order as the experimental values.

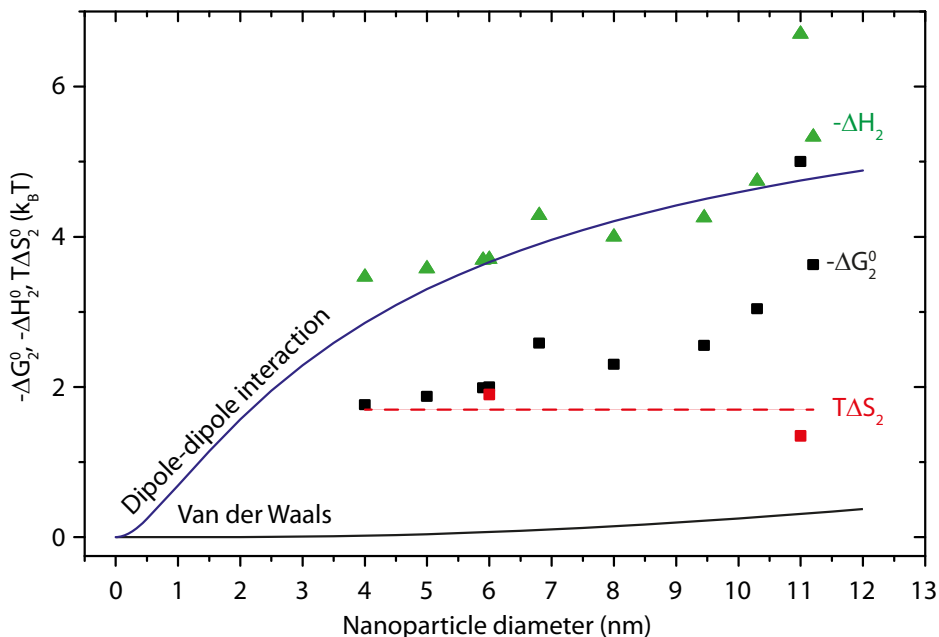


FIGURE 2.6. Coupling free energy from cryo-TEM for different particle sizes (black squares) and coupling enthalpy (green triangles) calculated from an estimated value for the coupling entropy (dashed line). The solid lines gives theoretical predictions for the coupling enthalpy from the Van der Waals interaction (bottom line) and a dipole-dipole interaction (top); for details see text.

**3.5. Size Dependence of the Coupling Free Energy.** In fig. 2.6 the coupling free energy is plotted as function of particle diameter, showing an increase in the coupling free energy as function of particle size from  $\sim -2 k_B T$  for 4 nm quantum dots to  $\sim -5 k_B T$  for 11 nm nanoparticles. The relatively high coupling free energy observed for the 11 nm particles is in line with the decreased colloidal stability compared to the smaller particles. A dispersion of the 11 nm particles forms a clear supernatant and a black sediment after a few months, whereas a dispersion of the 6 nm particles does not show any sign of sedimentation at all. The 11 nm sample with a  $\Delta G_2^0 \approx -5 k_B T$  contains much larger clusters, compatible with the faster sedimentation observed in this sample.

As stated before it is the coupling enthalpy rather than the coupling free energy which should be compared to the interaction potentials. As shown in section 3.4 the coupling entropy is within error independent of particle size, so as a first approximation, we can take the average of the coupling entropy of both systems to be a good estimate for the other particle sizes as well. Using this estimate, the coupling enthalpy can be obtained for the other particle sizes.

To model the results presented in this chapter a few general requirements of the necessary pair potentials can be formulated. From the radial distribution function it is clear that the pair potential has a minimum at a finite distance, typically the particle diameter plus 2-3 nm, with a steep repulsion at shorter distances and an attractive part at larger distances. This repulsive part is due to the interdigitation of the capping ligands which can be described by a hard sphere potential (see chapter 1) with an effective particle diameter equal to the minimal center-to-center distance.

To describe the attractive interaction at larger distances, several options are possible; however, from the orientation-dependent coupling free energy shown in fig. 2.4 it is clear that at least part of the interaction potential has an anisotropic character. One of the typical attractive interactions always present in non index-matched systems is the Van der Waals interaction, which for spheres is described by Hamaker's equation (eq. 1.4 in chapter 1). Different values for the Hamaker constant of PbSe nanoparticles at room temperature are reported in literature, ranging from  $6 k_B T$  [25] to  $12 k_B T$  [2]. In fig. 2.6 the contribution of the Van der Waals energy is plotted, calculated using a Hamaker constant of  $6 k_B T$  and a particle-particle separation of 3 nm. Beside the effect that the Van der Waals contributions are fairly small, they are isotropic and cannot describe the observed orientation dependence.

To explain the linear structures in the cryo-TEM images, a dipolar interaction has been proposed [12] which is based on the presence of net opposite charges on different sides of the nanocrystal. Opposite charges of  $\pm e$  are already sufficient to have an attraction of several  $k_B T$  assuming a surface-to-surface distance of 3 nm, as indicated by the solid line in fig. 2.6. However, this model predicts a flattening of the interaction energy at large nanoparticle diameters, whereas the cryo-TEM results show an increase at large diameters.

A more detailed discussion of the interaction between the quantum dots is presented in chapter 4, where both the size dependence of the coupling free energy and the second virial coefficient are discussed.

---

#### 4. Conclusions

The use of quantitative microscopy to study colloidal interactions is new to nanoparticles but has been applied extensively to fluorescent microparticles, using confocal laser scanning microscopy, with impressive results that inspired our further studies of nanoparticles [26, 27]. Here, we studied the contact free energy  $\Delta G_2^0$  of nanoparticles by direct cryogenic imaging of the equilibrium structures in liquid dispersions, both as function of size and temperature. The interaction free energy difference between linear and isotropic clusters indicates that the interaction potential has an anisotropic component, as the linear configuration has a lower coupling free energy than the isotropic clusters. From the temperature dependence, the separate enthalpic and entropic contributions can be obtained by application of Van 't Hoff's equation to the temperature-dependent contact free energies. The size dependence of the coupling free energy is compared to the predicted free energy from different models. As the thermodynamic basis is model independent, this method can be applied to any type of nanoparticle that can be imaged with cryo-TEM while dispersed in a liquid medium.

#### Bibliography

- [1] A. L. Rogach. Binary superlattices of nanoparticles: Self-assembly leads to “metamaterials”. *Angew. Chem., Int. Ed.*, 43(2):148–149, 2004.
  - [2] W. H. Evers, B. De Nijs, L. Filion, S. Castillo, M. Dijkstra, and D. Vanmaekelbergh. Entropy-driven formation of binary semiconductor-nanocrystal superlattices. *Nano Lett.*, 10:4235–4241, 2010.
  - [3] K. J. M. Bishop, C. E. Wilmer, S. Soh, and B. A. Grzybowski. Nanoscale forces and their uses in self-assembly. *Small*, 5(14):1600–1630, 2009.
  - [4] Y. J. Min, M. Akbulut, K. Kristiansen, Y. Golan, and J. Israelachvili. The role of interparticle and external forces in nanoparticle assembly. *Nat. Mater.*, 7(7):527–538, 2008.
  - [5] L. Filion, M. Marechal, B. van Oorschot, D. Pelt, F. Smallenburg, and M. Dijkstra. Efficient method for predicting crystal structures at finite temperature: Variable box shape simulations. *Phys. Rev. Lett.*, 103:188302, 2009.
  - [6] M. Kanemaru, Y. Shiraishi, Y. Koga, and N. Toshima. Calorimetric study on self-assembling of two kinds of monometallic nanoparticles in solution. *J. Therm. Anal. Calorim.*, 81(3):523–527, 2005.
  - [7] K. L. Planken, M. Klokkenburg, J. Groenewold, and A. P. Philipse. Ultra-centrifugation of single-domain magnetite particles and the De Gennes-Pincus
-



- approach to ferromagnetic colloids in the dilute regime. *J. Phys. Chem. B*, 113(12):3932–3940, 2009.
- [8] P. M. Frederik and N. Sommerdijk. Spatial and temporal. resolution in cryo-electron microscopy - a scope for nano-chemistry. *Curr. Opin. Colloid Interface Sci.*, 10(5-6):245–249, 2005.
- [9] A. P. Philipse and G. H. Koenderink. Sedimentation-diffusion profiles and layered sedimentation of charged colloids at low ionic strength. *Adv. Colloid Interface Sci.*, 100-102:613 – 639, 2003.
- [10] O. Balmes, J. O. Malm, G. Karlsson, and J. O. Bovin. Cryo-tem observation of 3-dimensionally ordered aggregates of 5 nm gold particles in organic solvents. *J. Nanopart. Res.*, 6(6):569–576, 2004.
- [11] M. Klokkenburg, R. P. A. Dullens, W. K. Kegel, B. H. Ern e, and A. P. Philipse. Quantitative real-space analysis of self-assembled structures of magnetic dipolar colloids. *Phys. Rev. Lett.*, 96(3):037203, 2006.
- [12] M. Klokkenburg, A. J. Houtepen, R. Koole, J. W. J. de Folter, B. H. Ern e, E. van Faassen, and D. Vanmaekelbergh. Dipolar structures in colloidal dispersions of PbSe and CdSe quantum dots. *Nano Lett.*, 7(9):2931–2936, 2007.
- [13] P. M. Frederik, M. C. A. Stuart, P. H. H. Bomans, W. M. Busing, K. N. J. Burger, and A. J. Verkleij. Perspective and limitations of cryoelectron microscopy - from model systems to biological specimens. *J. Microsc.*, 161: 253–262, 1991.
- [14] A. J. Houtepen, R. Koole, D. Vanmaekelbergh, J. D. Meeldijk, and S. G. Hickey. The hidden role of acetate in the PbSe nanocrystal synthesis. *J. Am. Chem. Soc.*, 128(21):6792–6793, 2006.
- [15] P. M. Frederik, P. H. H. Bomans, P. F. J. Laeven, and F. J. T. Nijpels. Device for preparing specimens for a cryo-electron microscope (Netherlands Industrial Property Office (ro/nl) pct/nl02/00189), 2002.
- [16] J. Dubochet, M. Adrian, J. J. Chang, J. C. Homo, J. Lepault, A. W. McDowell, and P. Schultz. Cryo-electron microscopy of vitrified specimens. *Q. Rev. Biophys.*, 21(2):129–228, 1988.
- [17] J. J. Crassous, M. Ballauff, M. Drechsler, J. Schmidt, and Y. Talmon. Imaging the volume transition in thermosensitive core-shell particles by cryo-transmission electron microscopy. *Langmuir*, 22(6):2403–2406, 2006.
- [18] P. M. Frederik, K. N. Burger, M. C. Stuart, and A. J. Verkleij. Lipid polymorphism as observed by cryo-electron microscopy. *Biochim. Biophys. Acta*, 1062(2):133–141, 1991.
-

- [19] H. Reiss, W. K. Kegel, and J. Groenewold. Length scale for configurational entropy in microemulsions. *Ber. Bunsen-Ges.-Phys. Chem.*, 100(3):279–295, 1996.
  - [20] M. Björling, G. Pellicane, and C. Caccamo. On the application of Flory-Huggins and integral equation theories to asymmetric hard sphere mixtures. *J. Chem. Phys.*, 111(15):6884–6889, 1999.
  - [21] A. P. Philipse and D. Maas. Magnetic colloids from magnetotactic bacteria: Chain formation and colloidal stability. *Langmuir*, 18:9977–9984, 2002.
  - [22] K. Denbigh. *The Principles of Chemical Equilibrium*. Cambridge University Press, 1957.
  - [23] F. Haber. The representation of ammonia from nitrogen and hydrogen. *Naturwissenschaften*, 10:1041–1049, 1922.
  - [24] J. Tellinghuisen. Van 't Hoff analysis of  $K^\circ(T)$ : How good ... or bad? *Biophys. Chem.*, 120:114–120, 2006.
  - [25] D. V. Talapin, E. V. Shevchenko, C. B. Murray, A. V. Titov, and P. Kral. Dipole-dipole interactions in nanoparticle superlattices. *Nano Lett.*, 7(5): 1213–1219, 2007.
  - [26] A. van Blaaderen. Quantitative real-space analysis of colloidal structures and dynamics with confocal scanning light microscopy. *Prog. Colloid Polym. Sci.*, 104:59–65, 1997.
  - [27] V. Prasad, D. Semwogerere, and E. R. Weeks. Confocal microscopy of colloids. *J. Phys.: Condens. Matter*, 19(11):113102, 2007.
  - [28] D. A. McQuarrie. *Statistical Mechanics*. Harper & Row, New-York, 1976.
-

## Appendix 2.A. Vitrification and Diffusion Rates

An estimate of the quenching time can be calculated using the heat diffusion equation:

$$(2.12) \quad \frac{\partial T(x, t)}{\partial t} = \alpha \frac{\partial^2 T(x, t)}{\partial x^2}$$

where the temperature  $T$  is a function of position  $x$  and time  $t$  and  $\alpha$  is the thermal diffusivity:  $\alpha = k/c_p\rho$  with  $k$  the thermal conductivity,  $c_p$  the heat capacity of the material, and  $\rho$  the mass density of the material. For a one-dimensional system, an analytical solution for this differential equation exists [28]:

$$(2.13) \quad T(x, t) = T_{N_2} + \frac{\Delta T}{2} \left( \text{Erf} \left[ \frac{x+d}{\sqrt{4\alpha t}} \right] - \text{Erf} \left[ \frac{x-d}{\sqrt{4\alpha t}} \right] \right)$$

$$\text{Erf}(x) = \frac{2}{\sqrt{\pi}} \int_0^x e^{-t^2} dt$$

In fig. 2.7 A, a schematic side-view of the liquid film is shown with typical dimensions. For this system, the temperature profiles at different times are shown in fig. 2.7 C and the temperature of the center is plotted as function of time in fig. 2.7 B. For a decalin film with a thickness on the order of a few particle diameters (30 nm) the quenching time is approximately 1 ns, corresponding to a vitrification rate of  $10^9 \text{ Ks}^{-1}$ . Taking into account the much smaller thickness of our samples and lower heat capacity of decalin, this is comparable to the reported quenching rate for aqueous systems.

The self-diffusion time of the particles is defined as the average time for a particle to diffuse its own diameter. For a spherical particle, the average diffusion distance  $r$  is defined as:

$$(2.14) \quad \frac{r^2}{6t} = D = \frac{k_B T}{6\pi\eta R_H}$$

where  $D$  is the diffusion coefficient,  $t$  is time,  $k_B$  Boltzmann's constant,  $T$  the absolute temperature,  $\eta$  the solvent viscosity, and  $R_H$  the hydrodynamic radius of the particle. For a QD with a core of 4 nm and a capping shell of 1.5 nm, the self-diffusion time is about 500 ns. So the quenching time is approximately 500 times shorter than the diffusion time, indicating that the observed images can be considered as room temperature snapshots.

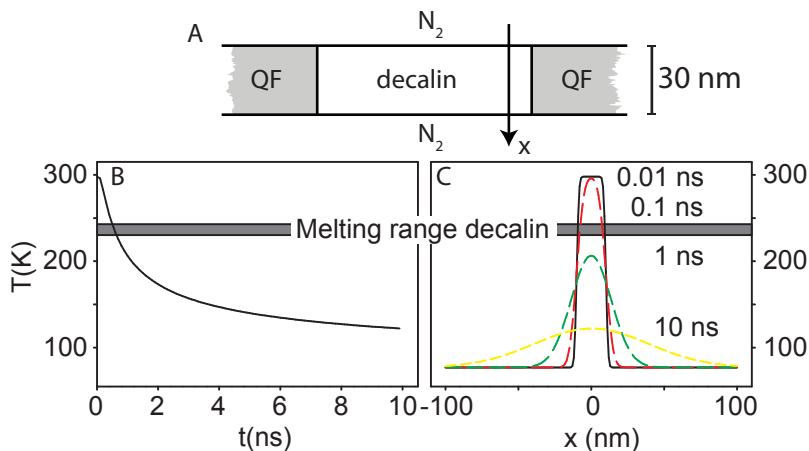


FIGURE 2.7. (A) Schematic representation of a hole in the Quantifoil (QF) TEM grid filled with a 30 nm thick film of decalin surrounded by liquid nitrogen. (B) Temperature at the centre of the film as function of time and (C) temperature profiles after different quenching times. The melting range of decalin is indicated as well.

### Appendix 2.B. Derivation of the Chemical Potential of Nanoparticle Clusters

Using statistical thermodynamics, an expression is derived for the chemical potential of the quantum dot clusters using a lattice model. The total free energy  $G_{tot}$  of this system is:

$$(2.15) \quad G_{tot} = N_S \mu_S + N_{QD} \mu_{QD}$$

where  $N$  and  $\mu$  are, respectively, the number of particles and the chemical potential of the solvent molecules  $S$  and the quantum dots  $QD$ . The chemical potential of the species can be calculated via:

$$(2.16) \quad \mu_S = \frac{\partial G_{tot}}{\partial N_S} \quad \mu_{QD} = \frac{\partial G_{tot}}{\partial N_{QD}}$$

The free energy can be split in a contribution of the pure systems and a contribution due to the mixing of these systems:

$$(2.17) \quad G_{tot} = N_S \mu_S^o + N_{QD} \mu_{QD}^o + \Delta_m G$$

$$(2.18) \quad \Delta_m G = \Delta_m H - T \Delta_m S$$

where  $\Delta_m H$  and  $\Delta_m S$  are the enthalpy and entropy of mixing, respectively. As the surface of our quantum dots is covered with apolar capping ligands and the particle is dispersed in an apolar medium, the interactions between solvent and capping are expected to be weak and the enthalpy of mixing is neglected.

**2.B.1. Entropy of Mixing.** The entropy of mixing is calculated using a lattice model where each lattice site has a size of 1 solvent molecule and each quantum dot takes  $A$  lattice sites. Using Boltzmann's formula for the entropy, the mixing entropy is calculated via:

$$(2.19) \quad \Delta_m S = S_{\text{mixed}} - S_{\text{demixed}}$$

$$(2.20) \quad = k_B \ln [W_{\text{mixed}}] - k_B \ln [W_{\text{demixed}}]$$

where  $W$  is the number of possible configurations in the mixed and demixed systems. The solvent molecules fill all space that is not taken by the quantum dots and therefore have  $W = 1$  in both pure solvent systems and mixed systems. The number of possibilities to place a quantum dot on a lattice containing  $N$  lattice sites is  $N$  for the first quantum dot,  $N - A$  for the second,  $N - 2A$  for the third and generally  $N - (n - 1)A$  for the  $n^{\text{th}}$  particle. The probability to place  $N_{QD}$  particles on a lattice with  $N$  positions becomes:

$$(2.21) \quad W = \frac{1}{N_{QD}!} \prod_{n=1}^{N_{QD}} (N - (n - 1)A)$$

where the factor  $1/N_{QD}!$  is used to take into account the indistinguishability of the particles. For the unmixed system, the total number of lattice sites is equal to  $AN_{QD}$ , such that the number of possible configurations becomes:

$$(2.22) \quad W_{\text{demixed}} = \frac{1}{N_{QD}!} \prod_{n=1}^{N_{QD}} (AN_{QD} - (n - 1)A)$$

$$(2.23) \quad = \frac{A^{N_{QD}} N_{QD}!}{N_{QD}!} = A^{N_{QD}}$$

Similarly for the mixed system containing  $N_{QD}$  quantum dots on a lattice with  $N$  sites we obtain:

$$(2.24) \quad W_{mixed} = \frac{1}{N_{QD}!} \prod_{n=1}^{N_{QD}} (N - (n-1)A)$$

which can be rewritten to:

$$(2.25) \quad W_{mixed} = \frac{A^{N_{QD}}}{N_{QD}!} \frac{\prod_{n=1}^{N/A} (N/A - (n-1))}{\prod_{n=N_{QD}+1}^{N/A} (N/A - (n-1))}$$

$$(2.26) \quad = \frac{A^{N_{QD}}(N/A)!}{N_{QD}!(N/A - N_{QD})!}$$

Using eqs. 2.20, 2.24 and 2.26 the mixing entropy becomes:

$$(2.27) \quad \Delta_m S = k_B \ln \left[ \frac{(N/A)!}{N_{QD}!(N/A - N_{QD})!} \right]$$

Using the Stirling approximation  $\ln(N!) = N \ln(N) - N$  this becomes:

$$(2.28) \quad \frac{-\Delta_m S}{k_B} = \frac{N_S}{A} \ln \left[ \frac{N_S}{N} \right] + N_{QD} \ln \left[ \frac{AN_{QD}}{N} \right]$$

**2.B.2. Chemical Potential of the Quantum Dots.** Combining this result with eq. 2.18 yields for the total free energy of the mixed system:

$$(2.29) \quad G_{tot} = N_S \mu_S^o + N_{QD} \mu_{QD}^o + k_B T \left( \frac{N_S}{A} \ln \left[ \frac{N_S}{N} \right] + N_{QD} \ln \left[ \frac{AN_{QD}}{N} \right] \right)$$

from which the chemical potential of the quantum dots can be calculated using eq. 2.16:

$$(2.30) \quad \mu_{QD} = \left( \frac{\partial G_{tot}}{\partial N_{QD}} \right)_{N_S} = \mu_{QD}^o + k_B T \ln \left[ \frac{AN_{QD}}{N} \right]$$

As no assumption with respect to the shape of the particle is made in this derivation, it must hold for any cluster of quantum dots. This equation can therefore be generalized for a cluster containing  $n$  particles to:

$$(2.31) \quad \mu_n = \mu_n^o + k_B T \ln \left[ \frac{nA_1 N_n}{N} \right]$$

where  $A_1$  is the number of lattice positions filled by a single quantum dot. In a three-dimensional system, the term inside the logarithm reduces to the volume fraction for a cluster of size  $n$ :

$$(2.32) \quad \phi_n = \frac{nA_1N_{QD}}{N}$$

or the two-dimensional equivalent, the surface fraction.

**2.B.3. Chain Length Distribution.** Using the chemical potentials derived above, the chain length distribution can be determined. For an equilibrium between a single particle and a cluster of particles, the change in free energy is defined as:

$$(2.33) \quad \Delta G = \mu_n - n\mu_1 \equiv 0$$

which, using eqs. 2.31 and 2.32 becomes:

$$(2.34) \quad (\mu_n^o - n\mu_1^o) + k_B T \ln \frac{\phi_n}{\phi_1^n} = 0$$

By introducing the coupling free energy defined as  $\Delta G_{cluster}^0 = \mu_n^o - n\mu_1^o$  and rewriting we obtain:

$$(2.35) \quad \ln \phi_n = n \ln \phi_1 - \frac{\Delta G_{cluster}^0}{k_B T}$$

For a linear chain, the cluster free energy can, as a first approximation, be written as a constant coupling free energy per particle-particle bond:

$$(2.36) \quad \Delta G_{cluster}^0 = \Delta G_2^0(n - 1)$$

which results in the chain length distribution:

$$(2.37) \quad \ln \phi_n = n \left( \ln \phi_1 - \frac{\Delta G_2^0}{k_B T} \right) + \frac{\Delta G_2^0}{k_B T}$$


---





# Adsorption of Nanoparticles at the Liquid/Air Interface Studied with Cryogenic Electron Tomography

## ABSTRACT

The three-dimensional distribution of nanoparticles at the liquid/air interface is imaged with cryogenic electron tomography. When the surface tension of the liquid is decreased, the interaction of the nanocrystals with the liquid/air interface shifts from adsorption to desorption. The concentration profiles are discussed in terms of the energies of the interfaces between nanoparticle, liquid, and air. The traditional method to investigate the adsorption of nanoparticles at liquid interfaces, a measurement of the macroscopic interfacial tension as function of concentration, does not reveal the adsorption-desorption transition but instead indicates an adsorption density much higher than a single monolayer of nanoparticles. This is due to the presence of free lead-oleate, a surface active species related to the capping ligands of the nanoparticles.

## 1. Introduction

Adsorption of colloidal particles at liquid interfaces is a versatile way to control the stability of emulsion droplets or microbubbles [1–4] or to guide the self-assembly of colloidal particles into superlattices or membranes [5–7]. For particles of only a few nanometers in size, adsorption to the liquid/gas or liquid/liquid interface can be of order  $k_B T$  and reversible [8], similar to molecular surfactants. To evaluate how strongly nanoparticles adsorb to liquid interfaces, the conventional method is to measure the interfacial tension as function of particle concentration [9–12]. However, in the presence of surface active molecular species, adsorption of the latter often dominates the changes in the macroscopic interfacial tension and obscures the effect of adsorbing colloidal nanoparticles. Here, we introduce Cryogenic Electron Tomography as a promising tool to investigate the adsorption energies of nanoparticles at the liquid/air interface. This technique resolves the spatial positions of individual nanoparticles, quantifying the complete concentration profile as a function of the distance of the nanoparticle center to the interface.

Previous in-situ characterizations did not provide a direct visualization of the distributions of individual nanoparticles at the liquid/air interface but instead relied on macroscopic measurements of the interfacial tension [12] or grazing incidence X-ray scattering [13]. Single-particle techniques do not detect the nanoparticles present below the interface, like AFM [14], or have insufficient resolution to resolve particles of a few nanometers, as in the case of SEM [15]. The technique that we adopt here, cryogenic electron microscopy (CEM), is well-known in biology [16] and gives snapshots even of structures that only exist in a narrow temperature window, such as the molecular liquid crystalline phases of a lipid membrane [17]. Also in the field of materials science, CEM is becoming an established way to visualize fragile structures at the nanoscale [18]. We have introduced CEM before to image nanoparticle structures in colloidal dispersions, be it only in two dimensions [19–22]. Here, the distribution of the nanoparticles is obtained in three dimensions using tomography [23].

## 2. Experimental

**2.1. Synthesis.** The so-called quantum dots (QDs) were synthesized according to a variation on the method of Kovalenko et al. [24] using standard airless techniques (Schlenk line and nitrogen glove box). Selenium (99.99%, Strem Chemicals, 1.2 g) was dissolved in 10 mL trioctylphosphine (90%, Sigma Aldrich). Lead

---

chloride (99.999%, Sigma-Aldrich, 0.95 g) and 17.5 mL oleylamine (90%, Aldrich) were combined and the mixture was heated to 160°C. At this temperature the Se-TOP solution and 2.5 mL  $\text{Sn}[\text{N}(\text{SiMe}_3)_2]_2$  (Sigma-Aldrich) was fast injected. The mixture was stirred for 2 minutes at 140°C and subsequently cooled down to room temperature. Oleic acid (90%, Sigma-Aldrich, 15 mL) was slowly added, followed by the addition of 40 mL methanol (99.8%, anhydrous, Sigma-Aldrich) to precipitate the particles. After centrifugation (2500 *g*, 5 minutes), the supernatant was removed and the quantum dots were dispersed in toluene (99.8%, anhydrous, Sigma-Aldrich).

For the cryo-electron-tomography experiments, a solvent is required that has a low vapor pressure at room temperature and vitrifies easily. Therefore the quantum dots were transferred to *cis/trans*-decalin (98%, Merck) and pentanol (98%, Baker) in different volume ratios by evaporation of the toluene and redispersion in the final solvent. Our experimental model system consists of PbSe nanocrystals with a diameter of 5.3 nm, dispersed in mixtures of decalin and pentanol. The surface of the particles is covered with oleic acid ligands, in order to disperse the particles in the solvent mixtures.

**2.2. Cryogenic Tomographic Transmission Electron Microscopy.** In a thermostatted Vitrobot, 3  $\mu\text{L}$  of 0.4  $\mu\text{mol/L}$  QD dispersion was placed on a QuantiFoil TEM grid with holes of 2  $\mu\text{m}$ , in an environment saturated with the solvent vapor. Excess fluid was removed using absorbent paper, resulting in a film with a thickness of a few particle diameters, after which the sample was vitrified using liquid nitrogen. For each sample, typically three tilt series of the vitrified samples were acquired on a Philips Tecnai 20 transmission electron microscope (200 keV) making use of a liquid-nitrogen-cooled Gatan 626 high-tilt cryo-holder. The tomograms were reconstructed using the weighted back projection implemented in IMOD [25] from tilt series containing approximately 100 images acquired at angles between  $-65^\circ$  to  $65^\circ$ .

Analysis of the tomograms was done using Matlab<sup>®</sup> 7. The particle positions were obtained from a cross-correlation of the tomograms with a spherical mask such that the maximums of this cross-correlation correspond to the positions of the particles. Contrast variations perpendicular to the electron beam cannot be resolved, which hinders the direct observation of the top and bottom surface of the liquid. However, in our system small density fluctuations occur in the liquid which give rise to a noise pattern with different amplitude than the background noise from acquisition and reconstruction. To measure the magnitude of the noise as

---

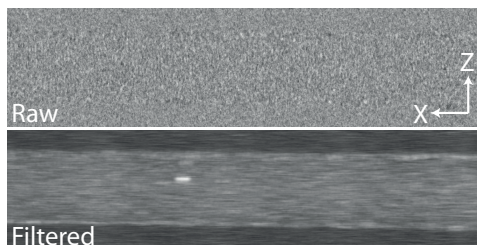


FIGURE 3.1. Raw X-Z slice of tomogram and the same slice after filtering. The liquid layer, which is hardly visible in the raw image is clearly visible in the filtered image. The layer is approximately 40 nm thick.

function of  $z$ , the tomogram was divided into columns of 40 by 40 pixels in the X-Y plane and all pixels in the Z-direction. For each of these stacks, the average pixel intensity was subtracted and all pixels with a negative deviation were discarded from the column. Only positive deviations of the average pixel intensity were taken into account because the nanoparticles are black objects (negative compared to the average value) which would strongly contribute to the average noise amplitude if also the negative deviations were taken into account. These positive fluctuations were averaged in the X-Y direction of each column to yield the noise amplitude as function of Z. These deviations are larger in the liquid compared to the fluctuations outside the liquid film due to the higher noise amplitude in the liquid as shown in fig. 3.1. The top and bottom of the liquid were defined as the Z-positions where the noise amplitude show the transition from small to large and vice versa.

**2.3. Surface Tension Measurements.** The macroscopic surface tensions of our liquid dispersions were measured with a Dataphysics OCA15 pendant drop tensiometer. The measurements were performed using drops of approximately 10  $\mu\text{L}$  in a saturated environment monitored for at least 5 hours to ensure that the system was in equilibrium and the interfacial tension was constant in time. Movies of the drop with 1 frame/minute were recorded and analyzed with Dataphysics SCA20 analysis software using the Young-Laplace expression [26]:

$$(3.1) \quad \Delta P = \Delta P(0) + \rho gh = \gamma \left( \frac{1}{R_1} + \frac{1}{R_2} \right)$$

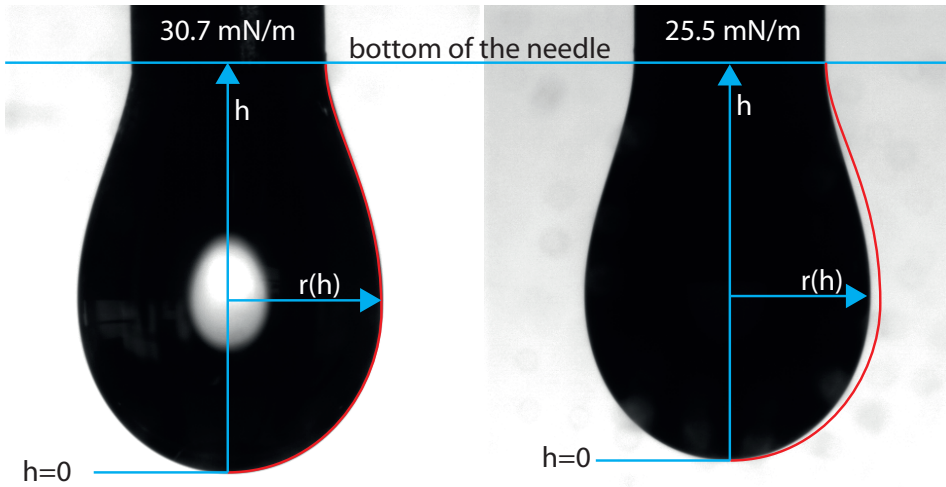


FIGURE 3.2. Image of two typical drops, with a surface tension of 31 mN/m and 26 mN/m, respectively. For comparison, the contour line of the left drop is copied to the right drop to visualize the difference of the drops.

This equation describes the pressure change  $\Delta P$  at the interface of the drop as function of the height  $h$ , where  $\rho$  is the droplet density,  $g$  the gravitational acceleration,  $\gamma$  is the surface tension of the droplet, and the radii of curvature of the interface are  $R_1$  and  $R_2$ . In the pendant drop geometry, the description of the interface profile gives a second order differential equation for which no analytical solution exists; the interfacial tension is determined by fitting the numerical solution of this equation to the drop profile.

### 3. Results

**3.1. Cryogenic Electron Tomography.** Our cryogenic electron tomography results are summarized in fig. 3.3. Representative X-Z views of samples with different volume fractions of pentanol are shown in fig. 3.3 (a-c), where the Z-axis is perpendicular to the film. From the tomograms, the particle positions, shown in fig. 3.3 (d-f), and the position of the surface are detected. Using this information, the distance of a particle center to the nearest interface (fig. 3.3 (g-i)) is calculated, which reveals the equilibrium distribution of particles between interface and bulk of the liquid. From fig. 3.3 it is clear that the equilibrium distribution shifts from

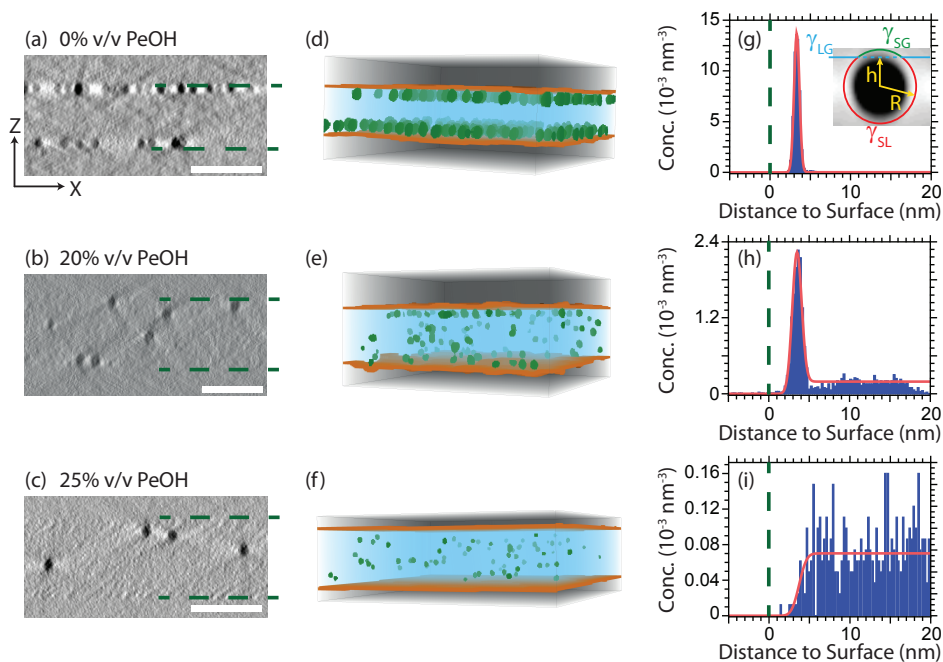


FIGURE 3.3. Cryogenic transmission electron tomography of free-standing thin liquid films of decalin/pentanol (PeOH) mixtures with added PbSe nanoparticles. (a-c) Representative cross sections perpendicular to the film with white scale bars of 25 nm, (d-f) 3D reconstructions of the sample volume in which the particles are green, the liquid is blue, and the interfaces are orange. (g-i) Concentrations in planes parallel to the film as a function of distance to the interface. The nanoparticles have a much stronger affinity to the surface of decalin than to decalin/pentanol mixtures, and surface coverage clearly remains less than a monolayer in all cases. The inset in (g) shows a close-up of a nanoparticle (average image of 100 nanoparticles) of radius  $R$  at a distance  $h$  from the decalin/air interface, with the interfacial tensions ( $\gamma$ ) between liquid (L), particle (S), and air (G).

strong adsorption, when the apolar liquid decalin is used (fig. 3.3 (g)), to weak adsorption, when the polar liquid pentanol is added (fig. 3.3 (i)).

The concentration profiles can be accounted for as follows. For an equilibrium system, the number density  $\rho$  of the particles at a distance  $h$  from particle center to liquid/air interface depends on the adsorption free energy  $F(h)$ , according to:

$$(3.2) \quad \rho(h) = \rho(\infty) \exp[-F(h)/(k_B T)]$$

where  $\rho(\infty)$  is the number density in the bulk liquid. The free energy profile is estimated via the Pieranski [27] approach, which has been successfully applied to many microparticle systems [1]. For a particle of radius  $R$  at a distance  $|h| < R$  from the liquid/air interface (see inset in fig. 3.3 (g)), the interfacial energy can be described by the sum of two contributions. First, the surface area of the liquid/air interface is decreased as the particle sticks out, resulting in a decrease in free energy of  $\Delta F = -\gamma_{LG}\pi(R^2 - h^2)$ , where  $\gamma_{LG}$  is the liquid/air interfacial tension. Second, part of the particle surface is now exposed to the gas, resulting in a change in free energy of  $\Delta F = (\gamma_{SG} - \gamma_{SL})2\pi R^2(1 - h/R)$ , where  $\gamma_{SG}$  and  $\gamma_{SL}$  are the interfacial tensions of the particle surface in, respectively, the gas and the liquid. Characterization of the binding strength of colloidal particles at a liquid/air interface is typically done by the contact angle  $\theta$ , defined as:  $\cos(\theta) = \Delta\gamma/\gamma_{LG} = (\gamma_{SG} - \gamma_{SL})/\gamma_{LG}$ . In fig. 3.3 (g-i), the solid red curve indicates the fitted distribution as obtained with this model using  $\Delta\gamma$  and  $\rho(\infty)$  as the fitting parameters and taking  $\gamma_{LG}$  from surface tension measurements on pure solvent mixtures: 30.7 mN/m for pure decalin, 28.7 mN/m for 20% v/v pentanol, and 28.3 mN/m for 25% v/v pentanol. To take into account the experimental resolution and fluctuations in the position of the interface, the distribution is broadened with a Gaussian having a standard deviation of 0.3-0.6 nm, corresponding to 1-2 pixels. The description using equation 3.2 and a potential energy in terms of  $\gamma_{LG}$ ,  $\gamma_{LS}$ , and  $\gamma_{SG}$  is clearly sufficient for a good fit of all the profiles.

**3.2. Colloidal Stability of Nanoparticles.** It is well known that the addition of a polar liquid like methanol can induce cluster formation and (size selective) precipitation of the studied type of nanoparticles [28], which would strongly influence the structures observed with cryo-electron-tomography. However, larger alcohols like butanol [28] and pentanol have this effect to a lesser extend. In pure decalin the clustering of the nanoparticles is reversible, with a coupling free energy of approximately  $-2k_B T$ , [22] indicating that only a small fraction of the particles is present in a cluster. These clusters are constantly forming and breaking up and therefore can adjust their shape to the energy potential set by the interface.

Although the aggregation strength increases with increasing pentanol concentration, the sample precipitates only at concentrations above 63% (fig. 3.4). Below 63% v/v pentanol the samples are stable for at least 1 week, indicating that the interactions are weak, even at much higher concentrations than the highest pentanol concentration used in our measurements (25% v/v). This indicates that the distributions observed with cryogenic electron tomography are mainly dictated by the adsorption of the particles to the interface and only to a lesser extent by the interactions between the nanoparticles.

**3.3. Macroscopic Surface Tension Measurements.** The conventional way to quantify reversible adsorption to the liquid/air interface is less direct than cryo-TEM, as it relies on measurement of the macroscopic surface tension as a function of the concentration of the surface active species.

From thermodynamics, the adsorption density  $\Gamma$  can be calculated using the Gibbs adsorption equation [29]. The common analysis assumes that besides pure solvent, the only other chemical component is the adsorbing species, so that

$$(3.3) \quad \Gamma = -\partial\gamma/\partial\mu = -(1/k_B T)\partial\gamma/\partial\ln(\phi)$$

where  $\gamma$  is the macroscopic interfacial tension and  $\mu$  the chemical potential of the adsorbing species, with  $k_B$  Boltzmann's constant,  $T$  the absolute temperature, and  $\phi$  the volume fraction of the particles. Here we assume that the chemical potential of the nanoparticles in the bulk behaves ideally and the finite volume of the nanoparticles can be neglected, such that the chemical potential can be expressed as:  $\mu = \mu^0 + k_B T \ln(\phi)$  where  $\mu^0$  is the chemical potential of the reference state, defined as a system where  $\phi$  equals one. The use of this relation is justified by the low volume fractions of particles ( $<1\%$  v/v) for the systems investigated in this chapter. A more general form of the Gibbs adsorption equation is  $d\gamma = \sum_i \Gamma_i d\mu_i$ , for a system with different components  $i$  [29]. In our case, the liquid consists of two components when decalin and pentanol are mixed, but their chemical potentials hardly change when the nanocrystals are added, since the particle volume fraction remains below 0.01; as such, eq. 3.3 remains a good first approximation.

As can be seen from the decreasing y-intercept in fig. 3.5, that is in absence of nanoparticles, addition of pentanol decreases the interfacial tension. With increasing nanoparticle concentration the interfacial tension gradually decreases further, indicating reversible adsorption. The slope of  $\gamma$  versus  $\ln\phi$  is more or less the same regardless of the pentanol concentration. Applying eq. 3.3 we find an adsorption

---



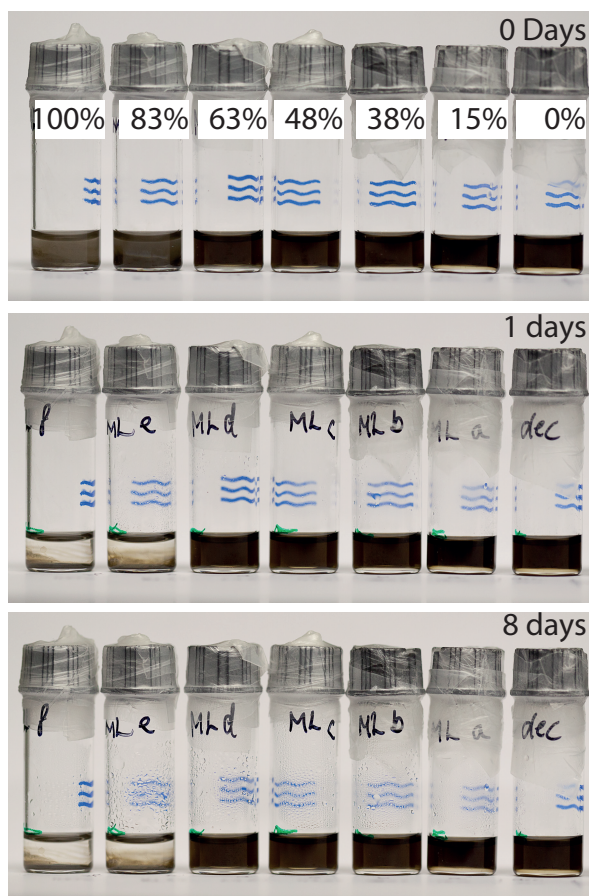


FIGURE 3.4. Stability of colloidal dispersions of PbSe nanoparticles in pentanol-decalin mixtures, with pentanol concentration from 0% v/v to 100% v/v (from right to left) followed in time. Above 63%, the dispersions aggregate and sediment within one day, while below 63% the system is stable for at least one week, which indicates that the interactions between the nanoparticles are weak.

density of  $4 \times 10^{17} \text{m}^{-2}$ , while electron microscopy shows that a close-packed monolayer can accommodate only  $0.12 \times 10^{17} \text{m}^{-2}$  particles (see inset of fig. 3.5).

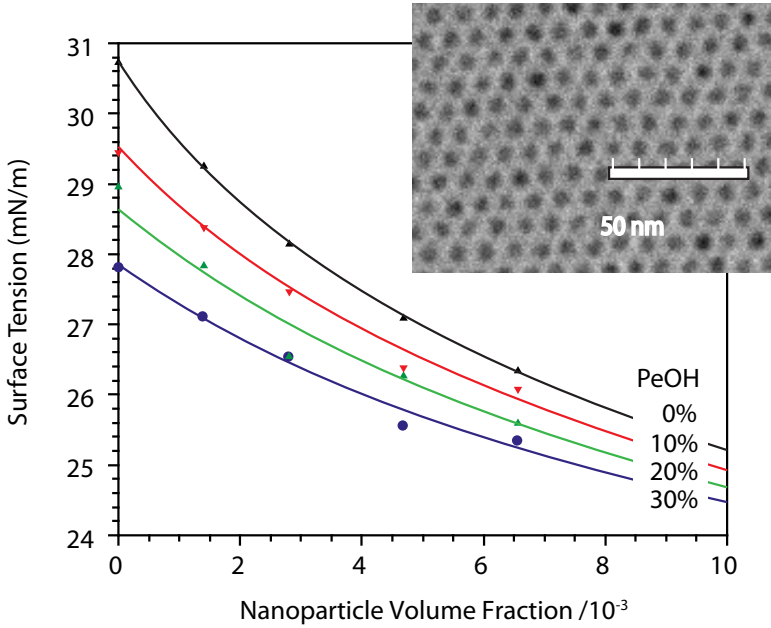


FIGURE 3.5. Interfacial tension of the liquid/air interface for mixtures of decalin and pentanol (PeOH) as a function of the concentration of PbSe nanoparticles. Inset: cryogenic transmission electron microscopy image of a full monolayer of particles, indicating the maximum possible packing density.

In fig. 3.6 the surface tension of a few samples is plotted as function of time. Initially when the droplet is created, the interface composition is predominantly that of the liquid and contains fewer nanoparticles than it would at equilibrium. Therefore, the surface tension decreases gradually in time, because nanoparticles diffuse from the bulk to the interface and adsorb to the interface, lowering the interfacial tension. Assuming that this process is diffusion limited, the decrease of the interfacial tension can be described in the limit of small times as [30]:

$$(3.4) \quad \gamma(t) = \gamma(0) - 2k_B T \rho \sqrt{\frac{Dt}{\pi}}$$

where the interfacial tension  $\gamma$  is described at a time  $t$  as function of the surface tension of the medium  $\gamma(0)$ , the nanoparticle number density  $\rho$ , and the diffusion coefficient  $D$ . The dashed line in fig. 3.6 shows the prediction of eq. 3.4 using a

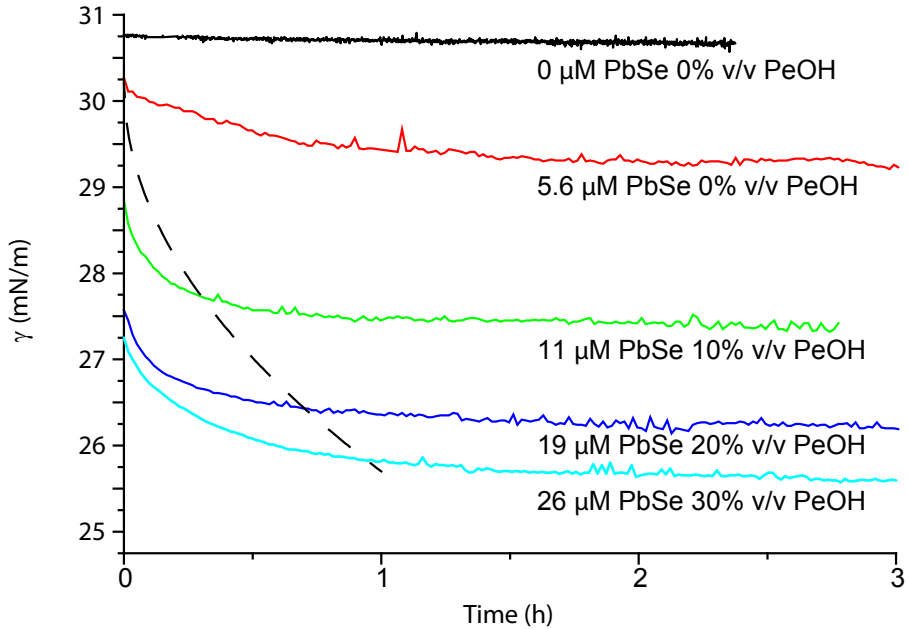


FIGURE 3.6. The surface tension of several samples plotted as function of time. The dotted line is calculated using eq. 3.4 and the diffusion coefficient of the nanoparticles.

concentration of  $5.6 \mu\text{mol/L}$  and calculating the diffusion coefficient via the Stokes-Einstein relation,  $D = k_B T / (6\pi\eta R_h)$ , which for particles with a hydrodynamic radius  $R_h$  of  $4.7 \text{ nm}$  dispersed in a medium with a viscosity  $\eta$  of  $1.9 \text{ mPa}\cdot\text{s}$ , gives  $D = 3.6 \times 10^{-11} \text{ m}^2/\text{s}$ . The predicted initial decrease in the surface tension is clearly much larger than is observed and the only two parameters that can be adjusted are the nanoparticle diameter or the number density of the particles. However, with this set of measurements these parameters are indistinguishable.

Both the time dependence and the concentration dependence of the interfacial tension point towards the presence of another surface active species besides pentanol or the nanoparticles. These other species determine the macroscopic interfacial tension and overshadow the contribution of the nanoparticles. The nature of these species is discussed at the end of the next section.

#### 4. Discussion

Rather than helping to explain the adsorption behavior observed by cryogenic electron tomography, the surface tension measurements are in conflict with it. The macroscopic surface tension suggests almost complete independence of the adsorption density on the decalin/pentanol ratio, whereas the tomographic measurements show a transition from strong adsorption to complete desorption. To resolve this discrepancy, we will first discuss the fitted interfacial tensions followed by an explanation of the apparently unrelated behavior of the macroscopic surface tension.

Fitting the data with eq. 3.2 yields quite high values of  $\Delta\gamma = \gamma_{SG} - \gamma_{SL}$ : in the case of pure decalin as the liquid,  $\Delta\gamma = 25.9$  mN/m, corresponding to a contact angle of  $32^\circ$ , and in the case of 20% v/v pentanol,  $\Delta\gamma = 25.7$  mN/m and  $\theta = 26^\circ$ . With 25% v/v pentanol, the particles do not adsorb at all, so the contact angle is not defined, and only a lower bound to  $\Delta\gamma$  can be given:  $\Delta\gamma > \gamma_{LG} = 28.3$  mN/m. The fact that  $\Delta\gamma$  has a high value can be understood on the basis of the surface coverage of the PbSe nanoparticles with oleic acid molecules, which consist of a carboxylic acid head group bound to the nanoparticle surface and an apolar octadecene tail pointing away from the nanoparticle. The surface of the nanoparticle is thus similar to octadecene (OD) and the particle/air interfacial tension is approximately that of octadecene/air,  $\gamma_{SG} \cong \gamma_{OD} = 28.16$  mN/m. For the particle/liquid interfacial tension an experimental value is not available, but an estimate can be obtained using the Girifalco and Good mixing rule [31]:

$$(3.5) \quad \gamma_{SL} = \gamma_{SG} + \gamma_{LG} - 2(\gamma_{SG}\gamma_{LG})^{1/2}$$

where we take the octadecene surface tension for the solid/gas interfacial tension  $\gamma_{SG}$  and the measured liquid/air interfacial tension is  $\gamma_{LG}$ . For all liquid compositions in this work, this estimate yields  $\gamma_{SL} < 0.1$  mN/m, so that  $\Delta\gamma \approx 28$  mN/m independent of solvent composition. This theoretical prediction has the correct order of magnitude but does not describe our observations precisely, as it would lead to an adsorption free energy of only  $-3 k_B T$  in the case of pure decalin, compared to  $-9 k_B T$  found by cryogenic tomography (see the minima in fig. 3.7 (a)). A more complete description of the interfacial energies would have to take into account more contributions than the terms of the Pieranski equation [32]. The effects of line tension and net charge on the nanocrystals will now be briefly discussed.

---

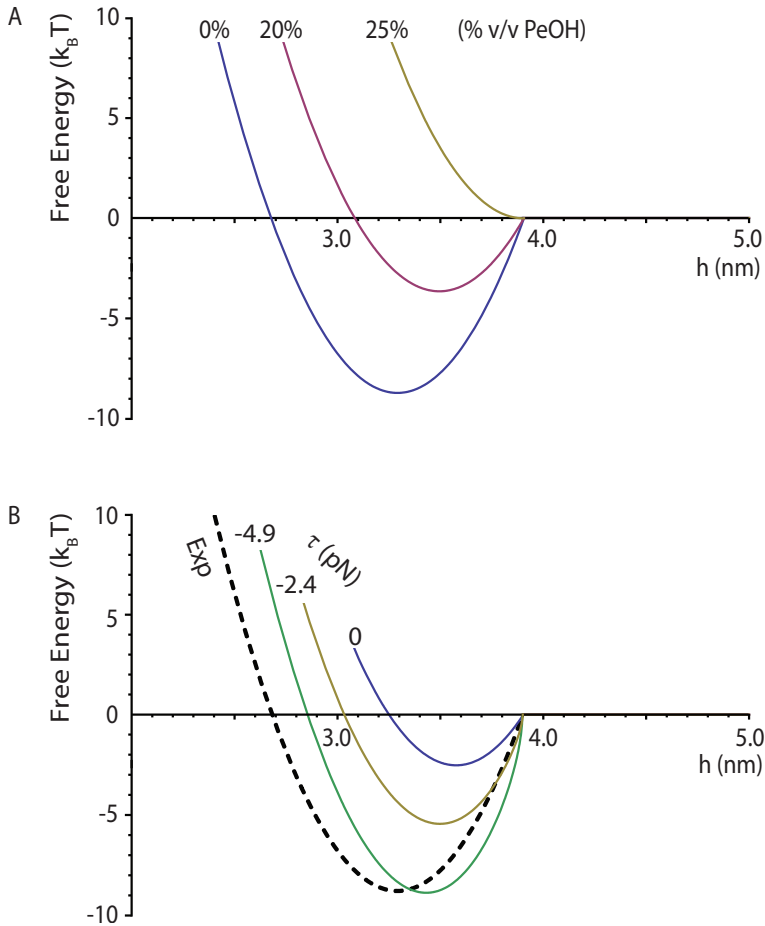


FIGURE 3.7. (a) Adsorption energy of nanoparticles as a function of distance to the interface at different pentanol concentrations, corresponding to the fitted profiles in fig. 3.3 (g-i). (b) The effect of line tension ( $\tau=0, -2.4,$  and  $-4.9$  pN) in the case of pure decalin, using  $\Delta\gamma = 28.1$  mN/m.

The surface tension is defined as that part of the total free energy of a phase-separated two-component system that cannot be ascribed to the bulk of the two phases, the so-called excess free energy. In a similar manner, for a three-component system, the free energy that cannot be ascribed to the bulk of the three phases nor the interface between them can be ascribed to the line where the three interfaces

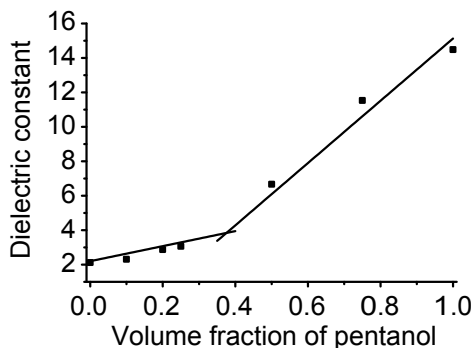


FIGURE 3.8. Dielectric constant of pentanol/decalin mixtures as function of the volume fraction of pentanol. The solid lines are Clausius-Mosotti relations for the low and high concentration regimes [33].

meet. In contrast to microparticles, nanoparticles are expected to exhibit much stronger line tension effects, which cause an additional contribution to the adsorption energy,  $\Delta F_\tau(h) = \tau (R^2 - h^2)^{1/2}$  [32]. As shown in fig. 3.7 (b), a line tension of  $-5 \times 10^{-12}$  N is already sufficient to change the adsorption free energy minimum from  $-3 k_B T$  to  $-9 k_B T$ . This value is close to that reported by Wi et al. [11] and well within the range of  $10^{-12}$  N to  $10^{-6}$  N reported experimentally [32]. Also, for models that include a line tension contribution, a non-continuous wetting transition is predicted [32], which can explain the sudden transition from adsorption to desorption of the nanoparticles when the solvent is changed from 20% to 25% pentanol. A more systematic study of the dependence of the adsorption energy on particle size would be necessary to determine the magnitude of the line tension.

Another option that could alter the surface adsorption behavior in our system is the presence of net charges on the nanoparticles. For a point charge approaching an interface between two mediums with a different dielectric constant, the interface becomes polarized, which can be described by the presence of an virtual image charge at a similar distance but on the opposite side of the interface [34]. The magnitude and sign of this image charge depend on the dielectric constants of the two mediums and in this case where the outside (vacuum) has a lower dielectric constant than the liquid, the sign of the image charge is equal to that of the real charge. This causes an effective repulsion between the charged object

and the interface, which lowers the adsorption energy and could eventually cause desorption of the particles if the repulsion becomes sufficiently strong.

An estimate of the fraction of charged particles can be obtained using the charging energy  $E_c$  calculated via [35]:

$$(3.6) \quad E_c = \sum_{l=0}^{\infty} \frac{e^2(\epsilon - 1)(l + 1)}{2\epsilon_2(\epsilon l + l + 1)R} \left(\frac{r}{R}\right)^{2l}$$

here,  $e$  is the electron charge,  $\epsilon = \epsilon_2/\epsilon_1$ ,  $\epsilon_2$  and  $\epsilon_1$  are the dielectric constants of the nanoparticle and the medium, respectively,  $R$  is the particle radius, and  $r$  is the distance of the charge to the center of the particle. Following the procedure of Shim and Guyot-Sionnest [36], the charging energy can be calculated assuming that the net charge is located at the surface of the nanoparticle. The radius of the dielectric sphere,  $R$ , is taken to be the core radius  $r_c$ , and the position  $r$  of the charge is taken to be  $r_c$  minus the  $\text{Se}^{2-}$  ionic radius of 0.198 nm. The dielectric constant of PbSe is  $\epsilon_2 = 250$  [37]. Using dielectric spectroscopy, the dielectric constants of the decalin-pentanol mixtures were measured as shown in fig. 3.8 [33]. For decalin, a value of 2.2 was found for the dielectric constant, corresponding to a charging energy of 5.1  $\text{k}_B\text{T}$  and a fraction of charged nanoparticles of less than one percent. The dielectric constant increases from 2.2 in pure decalin to 3.1 in 25% v/v pentanol (see fig. 3.8), but the charging energy is still 3.7  $\text{k}_B\text{T}$ , such that only 2.5% of the nanoparticles in our sample is charged. Considering the fact that even in the most polar sample investigated in this chapter only a small fraction of the nanoparticles is possibly charged, this phenomenon cannot explain the adsorption-desorption transition observed here.

Although the particle adsorption at the liquid/air interface can be accounted for on the basis of interfacial tensions and line tension, the question remains why the macroscopic measurements of the surface tensions show a qualitatively different behavior. The high adsorption density of  $4 \times 10^{17}$  particles/ $\text{m}^2$  calculated from fig. 3.5 corresponds to 1 particle per 3  $\text{nm}^2$ , much less than the cross section of the nanoparticle cores (22  $\text{nm}^2$ ). Although multilayer adsorption of nanoparticles has been found in simulations of liquid/liquid interfaces [38], our electron tomographic images show no evidence of multilayer adsorption. Therefore, the species that adsorb to the liquid/air interface and affect the measured interfacial tension are apparently not the nanoparticles themselves.

One candidate would be oleic acid molecules desorbed from the surface of nanoparticles, molecules that are about 2 nm in length. However, oleic acid molecules in aprotic solvents are present as linear apolar dimers [39], which do

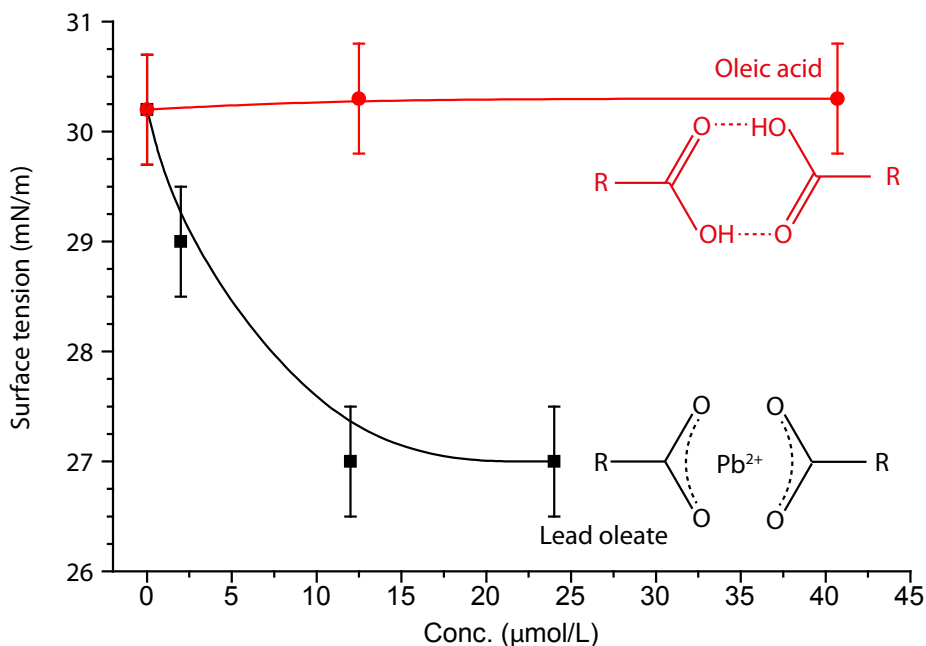


FIGURE 3.9. Surface tension of solutions of oleic acid and lead oleate in decalin as function of concentration (the lines are guides to the eye). The chemical structures represent the likely configuration of these molecules in solution, where R is the oleate chain.

not adsorb to the liquid/air interface; we verified that the surface tension of decalin remains unchanged (within 0.2 mN/m, see fig. 3.9) after dissolution of pure oleic acid, even up to a concentration of 0.040 mol/L, twice as much as present on the particles (assuming an adsorption density of  $\sim 3 \text{ nm}^{-1}$  [40]) in the sample with the highest nanoparticle concentration ( $\phi = 0.01$ ). A more plausible adsorbing species is lead oleate, consisting of a  $\text{Pb}^{2+}$  cation coordinated by two oleate ions in a v-shaped configuration [41]. We measured that 11  $\mu\text{mol/L}$  lead oleate suffices to decrease the interfacial tension of decalin by 3 mN/m (fig. 3.9), a concentration which can easily be present in the solution, even after repeated washing of the freshly synthesized nanoparticles.



## 5. Conclusion

In this chapter it is demonstrated with cryogenic electron tomography that colloidal nanocrystals coated with oleic acid molecules adsorb strongly at the surface of an apolar liquid and that they desorb when a liquid of lower interfacial tension is added. In contrast, no change in adsorption behavior was evidenced by measurements of the macroscopic surface tension as a function of the concentration of the nanocrystals. Those measurements were dominated by surface-active molecular species related to the ligands that stabilize the nanocrystals. Similar behavior is expected for many other types of nanocrystals, whose surface is generally coated with surface-active molecules so that they can be dispersed in apolar liquids [42].

## Bibliography

- [1] B. P. Binks. Particles as surfactants-similarities and differences. *Curr. Opin. Colloid Interface Sci.*, 7(1-2):21–41, 2002.
- [2] E. Vignati, R. Piazza, and T. P. Lockhart. Pickering emulsions: Interfacial tension, colloidal layer morphology, and trapped-particle motion. *Langmuir*, 19(17):6650–6656, 2003.
- [3] Y. Lin, H. Skaff, T. Emrick, A. D. Dinsmore, and T. P. Russell. Nanoparticle assembly and transport at liquid-liquid interfaces. *Science*, 299(5604):226–229, 2003.
- [4] T. N. Hunter, R. J. Pugh, G. V. Franks, and G. J. Jameson. The role of particles in stabilising foams and emulsions. *Adv. Colloid Interface Sci.*, 137(2):57–81, 2008.
- [5] A. Böker, J. He, T. Emrick, and T. P. Russell. Self-assembly of nanoparticles at interfaces. *Soft Matter*, 3(10):1231, 2007.
- [6] A. Dong, J. Chen, P. M. Vora, J. M. Kikkawa, and C. B. Murray. Binary nanocrystal superlattice membranes self-assembled at the liquid-air interface. *Nature*, 466(7305):474–7, 2010.
- [7] W. H. Evers, B. Goris, S. Bals, M. Casavola, J. de Graaf, R. van Roij, M. Dijkstra, and D. Vanmaekelbergh. Low-dimensional semiconductor superlattices formed by geometric control over nanocrystal attachment. *Nano Lett.*, 13(6):2317–2323, 2013.
- [8] Y. Lin, A. Böker, H. Skaff, D. Cookson, A. D. Dinsmore, T. Emrick, and T. P. Russell. Nanoparticle assembly at fluid interfaces: structure and dynamics. *Langmuir*, 21(1):191–4, 2005.

- [9] S. Ferdous, M. A. Ioannidis, and D. Henneke. Adsorption kinetics of alkanethiol-capped gold nanoparticles at the hexane/water interface. *J. Nanopart. Res.*, 13(12):6579–6589, 2011.
  - [10] S. Kutuzov, J. He, R. Tangirala, T. Emrick, T. P. Russell, and A. Böker. On the kinetics of nanoparticle self-assembly at liquid/liquid interfaces. *Phys. Chem. Chem. Phys.*, 9(48):6351–6358, Dec 2007.
  - [11] H. S. Wi, S. Cingarapu, K. J. Klabunde, and B. M. Law. Nanoparticle adsorption at liquid-vapor surfaces: influence of nanoparticle thermodynamics, wettability, and line tension. *Langmuir*, 27(16):9979–84, 2011.
  - [12] K. Du, E. Glogowski, T. Emrick, T. P. Russell, and A. D. Dinsmore. Adsorption energy of nano- and microparticles at liquid-liquid interfaces. *Langmuir*, 26(15):12518–22, 2010.
  - [13] M. Paulus, P. Degen, S. Schmacke, M. Maas, R. Kahner, B. Struth, M. Tolan, and H. Rehage. In situ observation of maghemite nanoparticle adsorption at the water/gas interface. *Eur. Phys. J.: Special Topics*, 167(1):133–136, 2009.
  - [14] L. N. Arnaudov, O. J. Cayre, M. A. Cohen Stuart, S. D. Stoyanov, and V. N. Paunov. Measuring the three-phase contact angle of nanoparticles at fluid interfaces. *Phys. Chem. Chem. Phys.*, 12(2):328–31, 2010.
  - [15] L. Isa, F. Lucas, R. Wepf, and E. Reimhult. Measuring single-nanoparticle wetting properties by freeze-fracture shadow-casting cryo-scanning electron microscopy. *Nat. Commun.*, 2:438, 2011.
  - [16] J. Dubochet, M. Adrian, J. J. Chang, J. C. Homo, J. Lepault, A. W. McDowell, and P. Schultz. Cryo-electron microscopy of vitrified specimens. *Quart. Rev. Biophys.*, 21(2):129–228, 1988.
  - [17] P. M. Frederik, K. N. Burger, M. C. Stuart, and A. J. Verkleij. Lipid polymorphism as observed by cryo-electron microscopy. *Biochim. Biophys. Acta*, 1062(2):133–41, 1991.
  - [18] H. Friedrich, P. M. Frederik, G. De With, and N. A. J. M. Sommerdijk. Imaging of self-assembled structures: Interpretation of TEM and cryo-TEM images. *Angew. Chem., Int. Ed.*, 49(43):7850–7858, 2010.
  - [19] K. Butter, P. H. H. Bomans, P. M. Frederik, G. J. Vroege, and A. P. Philipse. Direct observation of dipolar chains in iron ferrofluids by cryogenic electron microscopy. *Nat. Mater.*, 2(2):88–91, 2003.
  - [20] M. Klokkenburg, R. P. A. Dullens, W. K. Kegel, B. H. Ern e, and A. P. Philipse. Quantitative real-space analysis of self-assembled structures of magnetic dipolar colloids. *Phys. Rev. Lett.*, 96(3):37203, 2006.
-

- 
- [21] M. Klokkenburg, B. Ern , J. D. Meeldijk, A. Wiedenmann, A. Petukhov, R. Dullens, and A. P. Philipse. In situ imaging of field-induced hexagonal columns in magnetite ferrofluids. *Phys. Rev. Lett.*, 97(18):185702, 2006.
- [22] J. van Rijssel, B. H. Ern , J. D. Meeldijk, M. Casavola, D. Vanmaekelbergh, A. Meijerink, and A. P. Philipse. Enthalpy and entropy of nanoparticle association from temperature-dependent cryo-TEM. *Phys. Chem. Chem. Phys.*, 13(28):12770–12774, 2011.
- [23] P. A. Midgley, E. P. W. Ward, A. B. Hungria, and J. M. Thomas. Nanotomography in the chemical, biological and materials sciences. *Chem. Soc. Rev.*, 36(9):1477–94, 2007.
- [24] M. V. Kovalenko, D. V. Talapin, M. A. Loi, F. Cordella, G. Hesser, M. I. Bodnarchuk, and W. Heiss. Quasi-seeded growth of ligand-tailored PbSe nanocrystals through cation-exchange-mediated nucleation. *Angew. Chem., Int. Ed.*, 47(16):3029–33, 2008.
- [25] J. R. Kremer, D. N. Mastrorade, and J. R. McIntosh. Computer visualization of three-dimensional image data using IMOD. *J. Struct. Biol.*, 116(1):71–6, 1996.
- [26] J. Lyklema. *Fundamentals of Interface and Colloid Science. Volume I: Fundamentals*. Academic Press, Inc., 1991. ISBN 9780124605251.
- [27] P. Pieranski. Two-dimensional interfacial colloidal crystals. *Phys. Rev. Lett.*, 45(7):569–572, 1980.
- [28] C. B. Murray, D. J. Norris, and M. G. Bawendi. Synthesis and characterization of nearly monodisperse CdE (E= sulfur, selenium, tellurium) semiconductor nanocrystallites. *J. Am. Chem. Soc.*, 115(4):8706–8715, 1993.
- [29] R. J. Hunter. *Introduction to Modern Colloid Science*. Oxford University Press, 1st edition, 1993. ISBN 0198553862.
- [30] U. Teipel and N. Aksel. Adsorption behavior of nonionic surfactants studied by drop volume technique. *Chem. Eng. Techn.*, 24(4):393–400, 2001.
- [31] L. A. Girifalco and R. J. Good. A theory for the estimation of surface and interfacial energies. I. derivation and application to interfacial tension. *J. Phys. Chem.*, 61(13):904–909, 1957.
- [32] F. Bresme and M. Oettel. Nanoparticles at fluid interfaces. *J. Phys.: Condens. Matter*, 19(41):413101, 2007.
- [33] R. J. Kortschot. Dielectric constant of pentanol/decalin mixtures. Unpublished.
-

- [34] D. J. Griffiths and R. College. *Introduction to electrodynamics*. Prentice-Hall, Inc., 1999. ISBN 013805326.
  - [35] Louis E. Brus. A simple model for the ionization potential, electron affinity, and aqueous redox potentials of small semiconductor crystallites. *J. Chem. Phys.*, 79(11):5566, 1983.
  - [36] M. Shim and P. Guyot-Sionnest. Permanent dipole moment and charges in colloidal semiconductor quantum dots. *J. Chem. Phys.*, 111(15):6955, 1999.
  - [37] D. V. Talapin and C. B. Murray. PbSe nanocrystal solids for n- and p-channel thin film field-effect transistors. *Science*, 310(5745):86–9, 2005.
  - [38] R. J. K. U. Ranatunga, C. T. Nguyen, B. A. Wilson, W. Shinoda, and S. O. Nielsen. Molecular dynamics study of nanoparticles and non-ionic surfactant at an oil/water interface. *Soft Matter*, 7(15):6942–6952, 2011.
  - [39] D. H. Lee and R. A. Condrate. FTIR spectral characterization of thin film coatings of oleic acid on glasses: I. coatings on glasses from ethyl alcohol. *J. Mater. Sci.*, 34(1):139–146, 1999.
  - [40] M. Klokkenburg, J. Hilhorst, and B. H. Ern . Surface analysis of magnetite nanoparticles in cyclohexane solutions of oleic acid and oleylamine. *Vib. Spectr.*, 43(1):243–248, Jan 2007.
  - [41] T. Bala, B. L. V. Prasad, M. Sastry, M. U. Kahaly, and U. V. Waghmare. Interaction of different metal ions with carboxylic acid group: a quantitative study. *J. Phys. Chem. A*, 111(28):6183–90, 2007.
  - [42] C. B. Murray, C. R. Kagan, and M. G. Bawendi. Synthesis and characterization of monodisperse nanocrystals and close-packed nanocrystal assemblies. *Annu. Rev. Mater. Sci.*, 30:545–610, 2000.
-

## CHAPTER 4

# Second Virial Coefficient of Colloidal PbSe Nanoparticles

### ABSTRACT

The second virial coefficient ( $B_2$ ) is determined to quantify the interactions of PbSe nanoparticles dispersed in the apolar solvent decalin. Three independent techniques are used: cryogenic electron microscopy, small angle X-ray scattering, and analytical centrifugation. For particles smaller than 5.5 nm a positive  $B_2$  is found, showing that the repulsion between capping layers is the dominant interaction, while negative virial coefficients are measured for the larger particles, due to the increasing attractions of the nanoparticles. The dependence of the second virial coefficient on the nanoparticle size is accounted for by a dipolar hard sphere model and compared with the measured coupling enthalpies obtained from the analysis of the temperature dependence of the nanoparticle chain length distributions presented in chapter 2.

## 1. Introduction

An important parameter in theoretical physics, chemistry, and biology to quantify and to compare molecular and colloidal interactions is the osmotic second virial coefficient  $B_2$  [1]. It describes the first-order correction to the ideal gas equation of state, providing a link between the microscopic properties of a thermodynamic system, such as particle positions and interactions, and the macroscopic properties of this system, for example pressure. For instance, in biology the second virial coefficient ( $B_2$ ) is used to predict the crystallization of proteins [2], necessary for the determination of their atomic structure. In physical chemistry, the second virial coefficient for example plays a role in the steric repulsion of polymer brushes [3], utilized in the stabilization of colloids, or to quantify the interactions between these colloids [4–6]. The second virial coefficient can also be used to predict the critical temperature of a liquid-gas transition according to the Vliegenthart-Lekkerkerker criterion [7].

Several methods exist to measure  $B_2$  experimentally, based on different thermodynamic connections with microscopic or macroscopic properties of the system. In fig. 4.1 a schematic overview of three of these routes and corresponding measurements is shown. The best known approach to measure the  $B_2$  is from the angle-dependent scattering of light or X-rays, where the second virial coefficient can be obtained from the concentration dependence of the scattering intensity in the limit of forward scattering [1]. A second approach is to measure the osmotic pressure as function of concentration, for instance by integration of a sedimentation equilibrium obtained by analytical centrifugation [4, 8]. The third approach is quantitative microscopy, where the particle positions lead to the radial distribution function, from which the second virial coefficient is calculated by integration.

In this chapter, the use of cryo-TEM to obtain radial distribution functions and from that the second virial coefficient is examined for sterically stabilized PbSe nanoparticles in the apolar solvent decalin. For comparison,  $B_2$  is also determined by centrifugation and X-ray scattering. The dependence of the second virial coefficient on the particle size is discussed in terms of a dipolar hard sphere model.

## 2. Theory

For a system of non-interacting, uncharged solutes, Van 't Hoff's law dictates that the osmotic pressure  $\Pi$  is directly proportional to the particle number density

---

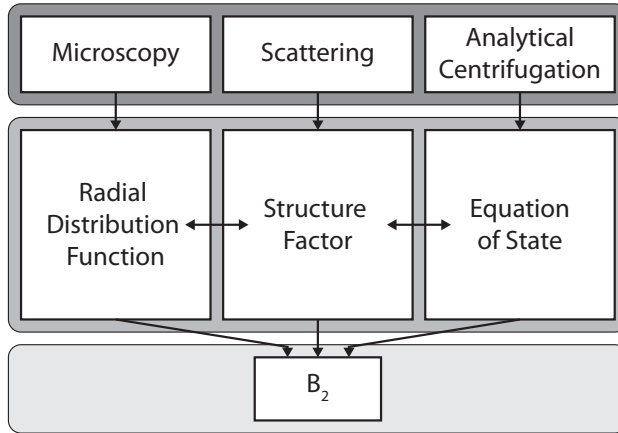


FIGURE 4.1. The three examined experimental techniques and their corresponding thermodynamic route to the second virial coefficient.

$\rho$ :

$$(4.1) \quad \Pi = k_B T \rho$$

where  $k_B T$  is the thermal energy. This equation of state completely neglects the size and interactions of the particles, but other equations of state exist which take these into account. A well known equation of state that describes the effect of the finite size of the particles via a hard sphere potential (see chapter 1) is the Carnahan-Starling (CS) equation of state [1]:

$$(4.2) \quad \Pi_{CS} = k_B T \rho \frac{1 + \eta + \eta^2 - \eta^3}{(1 - \eta)^3}$$

where the volume fraction  $\eta$  is defined as  $\rho v_0$  with  $v_0$  the volume of a particle. The general way to describe the influence of interaction is to use the virial expansion of the osmotic pressure:

$$(4.3) \quad \Pi = k_B T \rho (1 + B_2 \rho + B_3 \rho^2 + \dots)$$

where  $B_2$  and  $B_3$  are the second and third virial coefficient respectively. The second virial coefficient can be expressed as a function of the potential of mean force between the particles  $V(r)$  (see appendix 4.A).

$$(4.4) \quad B_2 = -\frac{1}{2} \int d\mathbf{r} (\exp[-V(r)/(k_B T)] - 1)$$

The relation between the macroscopic osmotic pressure and the microscopic properties can be determined via the radial distribution function  $g(r)$  or alternatively its Fourier transform, the structure factor  $S(q)$ . The radial distribution function is defined as:

$$(4.5) \quad g(r) \equiv \exp[-V(r)/(k_B T)]$$

where  $r$  is the center-to-center distance of the particles and  $V(r)$  the potential of mean force, which for low nanoparticle concentrations reduces to the orientationally averaged pair potential [5]. This opens the route from the (macroscopic) second virial coefficient to the microscopic radial distribution function calculated from the particle positions obtained from microscopy.

The second virial coefficient can also be related to the structure factor via the compressibility relation (see appendix 4.B):

$$(4.6) \quad k_B T \frac{\partial \rho}{\partial \Pi} = 1 + \rho \int d\mathbf{r} (g(r) - 1) = \lim_{q \rightarrow 0} S(q)$$

Combining this with eq. 4.3 we obtain:

$$(4.7) \quad \lim_{q \rightarrow 0} S(q) = \frac{1}{1 + 2B_2 \rho}$$

Here we neglect the third and higher order virial terms. This equation predicts a linear relation between the inverse structure factor and the nanoparticle number density, and the second virial coefficient is determined from the slope of a plot of  $S(0)$  as function of the number density.

**2.1. Relation between  $B_2$  and the Colloidal Pair Interaction.** The second virial coefficient can be calculated for a three dimensional system using the following equation:

$$(4.8) \quad B_2 = 2\pi \int r^2 (1 - \exp[-V(r)/k_B T]) dr$$

where  $r$  is the interparticle distance. The potential of mean force  $V$  is for sufficiently low number densities defined as [9]:

$$(4.9) \quad V(r) = -\log[\langle \exp[-\phi(r, \Omega)] \rangle_{\Omega}]$$

Here  $\phi$  is the pair potential between two particles, which is averaged over all orientations  $\Omega$  to obtain the potential of mean force.

To model the second virial coefficient for our system, we need an attractive and a repulsive term as demonstrated in chapter 2. The repulsive part of our interaction potential comes from the ligands at the surface of the nanoparticle. As



discussed in chapter 1, this repulsion can be modeled as a hard sphere repulsion with a sphere diameter of  $\sigma + 2r_c$  where  $\sigma$  is the diameter of the quantum dot core and  $r_c$  the thickness of the ligand shell:

$$(4.10) \quad \phi_{rep}(r) = \begin{cases} \infty & r < \sigma + 2r_c \\ 0 & r \geq \sigma + 2r_c \end{cases}$$

To model the attractive part of the interaction potential, a dipole-dipole interaction is used, although the origin of the anisotropic interaction studied by Klokkenburg et al. [10] and quantified again in chapter 2 is still not clear. Using analytical expressions for the weak coupling regime of hard sphere dipoles [5], we investigate the size dependence of the coupling constant  $\lambda$  using the dipole-dipole interaction:

$$(4.11) \quad \phi_{dd}(r, \Omega) = k_B T \lambda \left( \frac{\sigma_c + 2r_c}{r} \right)^3 f(\Omega)$$

$$(4.12) \quad \lambda = \frac{1}{4\pi\epsilon k_B T} \frac{p^2}{(\sigma_c + 2r_c)^3}; \quad p = p_0 \left( \frac{\sigma_c}{\sigma_0} \right)^n$$

Here,  $r$  is the distance between the two particles,  $f(\Omega)$  is a function that describes how the interaction depend on the relative orientation of the dipole moments,  $\sigma_c$  is the core diameter,  $r_c$  is the thickness of the capping layer, and  $\epsilon$  is the dielectric constant of the medium. As the origin of the dipole moment is unclear we model it as a power law of the nanoparticle core diameter. The constants  $p_0$  and  $\sigma_0$  are the dipole moment and particle diameter of a reference system of nanoparticles with similar shape and material. If the dipole of a particle is due to a bulk effect, the dipole moment scales with the volume of the quantum dots, that is,  $n = 3$ . Similarly, if the dipole moment is due to a positive and negative charge residing on opposite sides of the QDs the dipole moment depends linearly on the diameter, i.e.  $n = 1$ , and if the dipole moment is due to the surface atoms,  $n = 2$ .

Combining eqs. 4.8 to 4.12 yields an analytical expression that approximates the second virial coefficient of a dipolar hard sphere from the coupling parameter [5]:

$$(4.13) \quad \frac{B_2}{B_{2HS}} = 1 - \frac{1}{3}\lambda^2 - \frac{1}{75}\lambda^4 - \frac{29}{55125}\lambda^6 + O(\lambda^8)$$

where  $B_{2HS} = (2/3\pi)(\sigma_c + 2r_c)^3$  is the second virial coefficient for a system containing hard spheres of the same size. Equation 4.13 is valid if  $\lambda$  is between zero and approximately three [5].

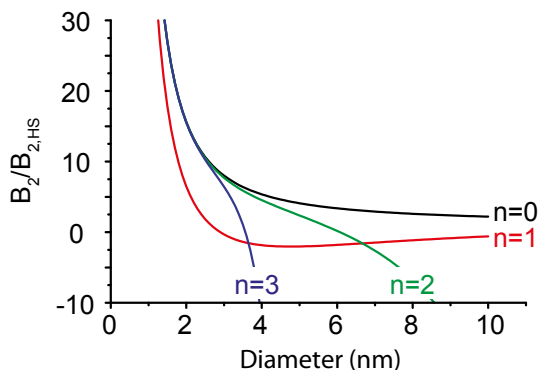


FIGURE 4.2. The second virial coefficient of a core-shell particle with an impenetrable shell and an attractive core normalized to the hard-sphere second virial coefficient of the core for different size dependencies of the dipole moment:  $p = p_0(\sigma_c/\sigma_0)^n$ . The curves are calculated using a reference size of  $\sigma_0 = 1$  nm and  $p_0$  is 0 Cm,  $2 \times 10^{-28}$  Cm,  $3 \times 10^{-29}$  Cm, and  $1.5 \times 10^{-29}$  Cm, for  $n$  is 0 to 3 respectively.

In fig. 4.2,  $B_2/B_{2HS}$  is plotted as function of particle size for different values of  $n$ . A clear difference is observed for  $n \leq 1$  and  $n > 1$ . In cases where  $n > 1$  and the particles are small, the curves overlap because the attractive part of the interaction potential becomes negligible and only the repulsive part remains. The curves are normalized to the hard sphere second virial coefficient of the core, neglecting the repulsive contribution of the capping ligands; therefore the relative value of  $B_2/B_{2HS}$  goes to infinity for small particle diameters. Upon increasing the particle diameter, the interactions become more and more dominant and deviations of a pure hard sphere second virial coefficient (black line in fig. 4.2) occur. In cases where  $n \leq 1$ , the opposite behavior is seen, as the deviations are clear for the small particle diameters and the curve approaches the pure hard sphere case when the particle grow larger.

### 3. Methods

**3.1. Experimental System.** All measurements were performed on colloidal PbSe nanocrystals capped with oleic acid and dispersed in the apolar medium

decalin. The nanoparticles were obtained from the Condensed Matter and Interfaces group, Utrecht University and synthesized using the procedures described in chapters 2 and 3. Solvent exchange was performed by evaporating the original medium, typically toluene, under a gentle flow in a nitrogen environment, and the particles were redispersed into decalin.

**3.2. Cryogenic Transmission Electron Microscopy.** Cryo-TEM samples were prepared according to the procedure described in section 2.2 of chapter 2 by placing 3  $\mu\text{L}$  of an approximately 0.4  $\mu\text{M}$  QD dispersion on a QuantiFoil TEM grid with 2  $\mu\text{m}$  holes. Excess fluid was removed using absorbent paper, resulting in a film with a thickness of a few particle diameters, after which the sample was vitrified using liquid nitrogen. The TEM-grids were mounted into a liquid nitrogen cooled Gatan 626 cryo-holder and cryo-TEM images were acquired using a Tecnai 12 electron microscope, operated at 120 keV.

From the images, the particle positions ( $\mathbf{r}$ ) were determined using Mathematica and the radial distribution functions ( $g(r)$ ) were obtained for each image using:

$$(4.14) \quad g(\mathbf{r}) = \frac{1}{\rho} \left\langle \sum_{i \neq j} \delta(\mathbf{r}_i - \mathbf{r}_j - \mathbf{r}) \right\rangle_i$$

where  $\rho$  is the average number density of the system. To take into account the finite size of the images, the  $g(r)$  was calculated from a histogram of all particle-particle distances normalized using a simulated ideal gas radial distribution function with the same boundary conditions of the sample.

The second virial coefficient was obtained by integrating the radial distribution function in the low density limit according to eqs. 4.4 and 4.5:

$$(4.15) \quad B_2 = 2\pi \int_0^\infty r^2 (1 - g(r)) dr$$

Direct numerical integration of the measured  $g(r)$  is not possible due to the noise that becomes important at large distances. Fitting the data with a suitable function that describes the main features of the radial distribution function reduces this problem. Different functions are used that are approximately zero for small  $r$ , have a peak at a particular distance  $r$ , and finally approach unity at large distances, such that the integral converges. The final value of  $B_2$  depends only little on the choice of the exact mathematical form of these equations.

**3.3. Analytical Centrifugation.** Analytical centrifugation measurements were performed using a LUMiSizer with a custom-made upgrade to allow 100 days continuous operation (LUM, Berlin) following the LUMiFuge procedure developed by Luigjes et al. [8]. For a typical measurement, a capillary of 50  $\mu\text{m}$  internal thickness and a length of 20 mm was filled for 10-15 mm with the sample containing about 2 – 15 % v/v of the nanoparticles. These capillaries were then closed by applying two-component epoxy glue on both ends and glueing this into the metal holder. This complete assembly was loaded into a standard 2 mm path length LUMiSizer cell.

A typical centrifugation measurement consists of 3 steps. In the first step, 256 scans were recorded at 2 second intervals to acquire a low noise initial profile. Next, scans were recorded at half an hour intervals typically for 3-4 weeks, to reach sedimentation-diffusion equilibrium. Finally the equilibrium profile was obtained, again by averaging 256 scans at 2 second intervals.

The 0% and 100% transmission levels were determined internally from the transmission through the metal (0% transmission) and the liquid depleted from the nanoparticles at the end of the centrifugation procedure (100% transmission). The concentration profile was then calculated from the absorption at each height in the sample, and it was subsequently integrated to obtain the osmotic pressure as function of position:

$$(4.16) \quad \Pi(r) = \Delta m \omega^2 \int_0^r \rho(r') r' dr'$$

where  $r$  is the distance to the rotor,  $\Delta m$  the buoyant mass of the particles,  $\omega$  the angular velocity, and  $\rho(r)$  the number density. For the lowest values of  $r$ , the number density cannot be obtained or not very accurately due to the noise and therefore the osmotic pressure profile is assumed to follow the Van 't Hoff law. The buoyant mass is derived from this part of the curve from the slope of the logarithm of the absorbance versus the square of the position. As both the number density and the osmotic pressure are known at all heights in the sample, it is straightforward to construct the equation of state. The value for  $B_2$  is extracted by fitting the equation of state with eq. 4.3, including the third virial term to account for deviation at high concentrations. Equation 4.3 can be rewritten to:

$$(4.17) \quad \left( \frac{\Pi}{\rho k_B T} - 1 \right) \frac{1}{\rho} = B_2 + B_3 \rho$$

---

If the equation of state is plotted this way, the second virial coefficient is given by the y-intercept and the third virial coefficient can be obtained from the slope. This way the contributions of the virial coefficients can be distinguished visually.

**3.4. Small Angle X-ray Scattering.** The second virial coefficient is also determined from small angle X-ray scattering (SAXS). The data were collected at the ESRF Facility in Grenoble at the BM26 DUBBLE beamline operated at 11 keV. The detector, a Dectris Pilatus3 1M, is mounted at 6.5 m from the sample aligned such that the beam is located in the bottom right corner of the detector opening a wide range of  $q$  values. The images are calibrated using wet rat-tail collagen.

Radial scattering profiles are obtained by azimuthal averaging of the 2D patterns with Fit2D software [11]. These scattering profiles are subsequently corrected for beam intensity and absorption by dividing the intensities by the intensity of the transmitted beam measured using ion chambers mounted directly after the sample. The background scattering due to the capillary and liquid is obtained using the same procedure and subtracted from the data.

As the scattered intensity is the product of the form factor and the structure factor, the structure factor is determined from the concentration dependence of the scattering pattern via:

$$(4.18) \quad S_C(q) = \frac{I_C(q)/C}{I_0(q)/C_0}$$

where  $S_C$  is the structure factor for the sample with concentration  $C$  and  $I_C$  is the radial scattering profile. The reference profile  $I_0$  is that measured at the lowest concentration  $C_0$  and contains only the form factor of the particles.

The limit of the structure factor in the case of  $q \rightarrow 0$  is calculated utilizing the fact that  $S(q)$  is proportional to  $q^2$  for small  $q$ , so that the y-intercept of a linear fit of  $S$  as function of  $q^2$  for  $10^{-2} < q < 10^{-1}$  is used to obtain this limit. Subsequently the second virial coefficient is obtained from a least squares fit of eq. 4.7 to the measured compressibilities.

## 4. Results

**4.1. Cryo-TEM.** In fig. 4.3 typical cryo-TEM images are shown for 5-11 nm PbSe QDs. For each size, typically 100 images are acquired (>10000 particles in total) and the  $g(r)$  is calculated for each image and averaged, weighted by the number of particles. Care is taken that no higher order peaks are present in each of the individual radial distribution functions. In fig. 4.4 measured radial dis-

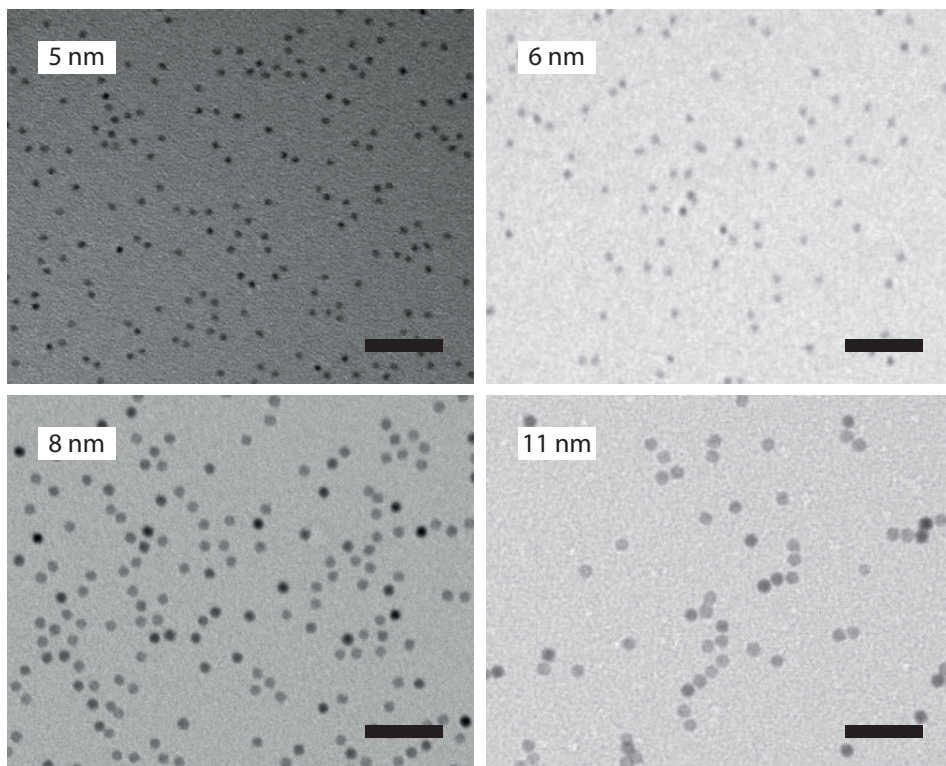


FIGURE 4.3. Typical Cryo-TEM images for PbSe QDs in decalin with a diameter of 5 nm, 6 nm, 8 nm, and 11 nm. The scale bars in the images represent 50 nm.

tribution functions and the corresponding fits are shown for three systems with different diameters of the quantum dots. The absence of higher order peaks indicates that the sample can be considered to be in the low number-density limit. The peak in the radial distribution function shifts to larger values with increasing nanoparticle diameter, indicating the increase of the center-to-center distance of two nanoparticles at contact. This distance is due to the size of the nanoparticle core and the repulsive capping ligands adsorbed at the surface, which keep the nanoparticles separated by about 3 nm, corresponding to slightly interdigitating ligands (the ligand length is approximately 2 nm). The increased height of the peak with increasing particle size indicates an increasing contact free energy (eq. 4.5), corresponding qualitatively to the observed trend in the coupling free

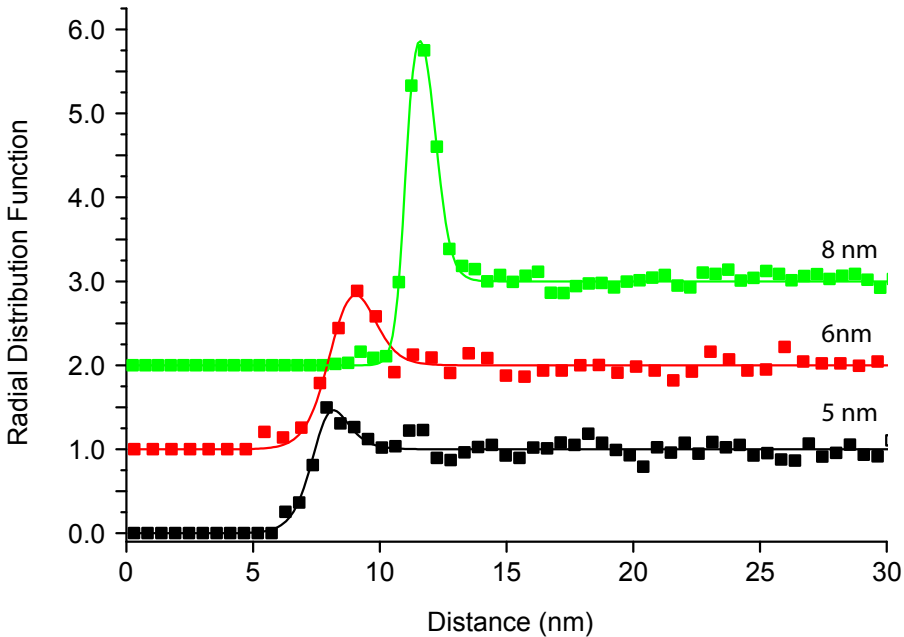


FIGURE 4.4. Experimental  $g(r)$  from cryo-TEM and the corresponding fits for PbSe nanoparticles with a core diameter of 5 nm, 6 nm, and 8 nm. The curves are shifted vertically for clarity.

energy (see chapter 2). Determination of the  $g(r)$  of larger particles becomes more and more problematic due to this increasing interaction. The theory used for the analysis of the radial distribution is valid in the low number-density limit and for larger particles the interaction becomes so strong that even in the lowest experimental accessible concentration limit, this requirement is not met and the radial distribution function shows higher order correlations.

Integration of the fits of the radial distribution functions with eq. 4.15 yields values of the second virial coefficient ranging from  $1.8 \pm 2 \times 10^2 \text{ nm}^3$  for 5 nm QDs to  $-22 \pm 2 \times 10^2 \text{ nm}^3$  in the case of 8 nm QDs, clearly changing from positive to negative with increasing size. A discussion of these results is given in section 5.

**4.2. Analytical Centrifugation.** In fig. 4.5 the final transmission profile is shown as function of the position in the capillary after 3 weeks of centrifugation at 2000 rpm ( $\approx 500 g$ ) for QDs with a diameter of 4.4 nm, 5.6 nm, and 6.3 nm. The distance in the capillary is defined with respect to the center of the rotor.

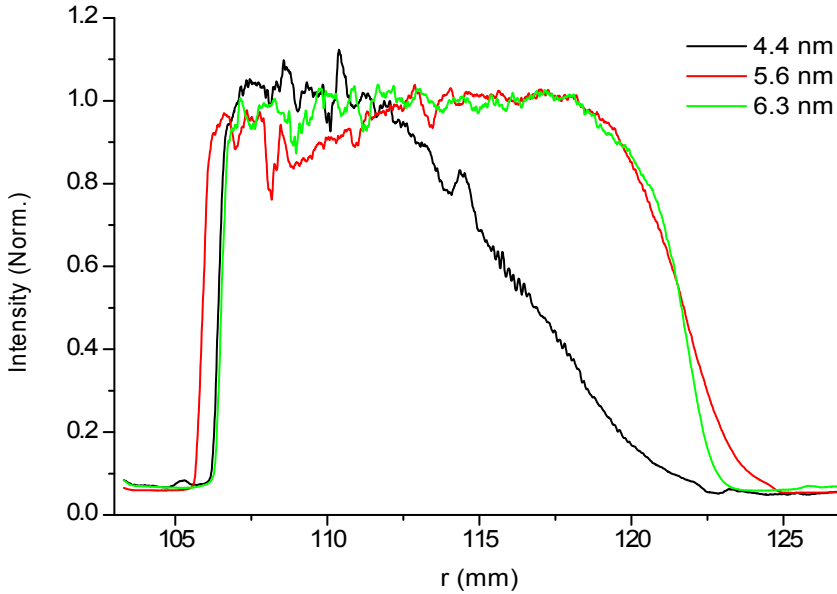


FIGURE 4.5. Transmission curves (raw data) for 4.4 nm, 5.6 nm, and 6.3 nm PbSe QDs after 3 weeks of centrifugation at 2000 rpm.

Experiments were also carried out for a sample of 5.3 nm QDs but the data is not shown in the plots because it is very similar to the data of the 5.6 nm QDs. The transmission profiles in fig. 4.5 are more compressed for the larger particles than for the smaller particles, in agreement with the decreased gravitational length  $l_g$ .

$$(4.19) \quad l_g = \frac{k_B T}{\Delta m \omega^2 r}$$

where  $\Delta m$  is the buoyant mass of the particles,  $\omega$  the rotation speed,  $r$  the distance to the rotation axis, and  $k_B T$  the thermal energy. This gravitational length is defined for an ideal gas and describes only the general trend in fig. 4.5.

From the logarithm of these transmission profiles, the concentration profiles are calculated, and subsequently integrated using eq. 4.16 to calculate the osmotic pressure as function of height. From the concentration profile and the osmotic pressure profile, the equation of state is obtained. In fig. 4.6 the equation of state is shown for the three particle sizes in normal representation (A) and in a representation highlighting the second virial term (B). The Van 't Hoff and the Carnahan-Starling (CS) equations of state (eq. 4.2) are plotted in fig. 4.6 (A) as well. The equation of state of the smallest particles stays between the Van 't Hoff



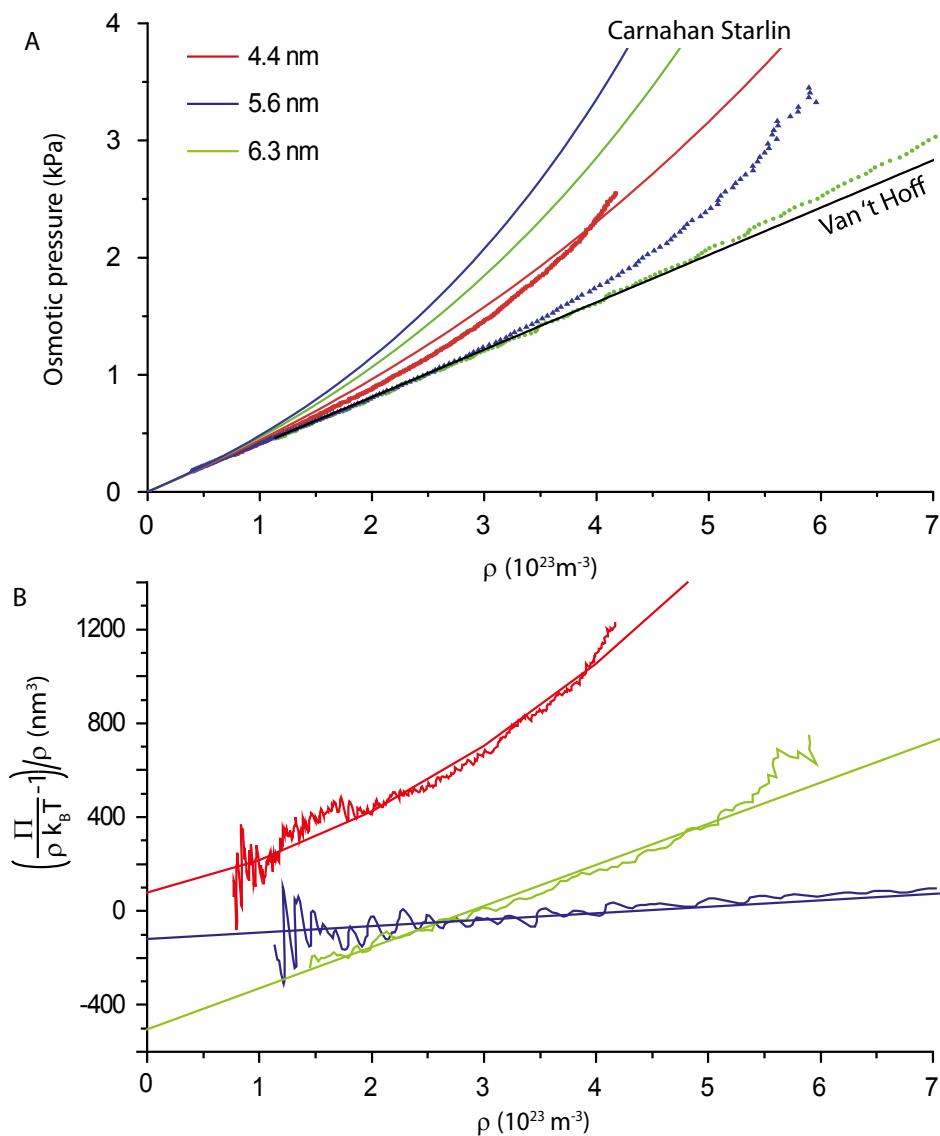


FIGURE 4.6. (A) The equation of state for 4.4 nm, 5.6 nm, and 6.3 nm QDs from analytical centrifugation. The solid lines are the Van 't Hoff (black) and the Carnahan-Starling (colored) equation of states. (B) Representation of the equation of state which highlights the contribution of the higher order virial terms, see text for details.

and CS equations of state, indicating that attractive interactions are present but the hard core repulsion of the particles is still the dominant factor. However, for the larger particles, the equation of state drops even below the ideal gas relation, indicating that attractions become the dominant factor. This is highlighted in fig. 4.6 (B) which is a representation of the equation of state (eq. 4.17) of which the y-intercept is the second and the slope is the third virial coefficient. From the y-intercept, the values of  $B_2$  are determined to be from  $0.8 \pm 0.5 \times 10^2 \text{ nm}^3$  for the 4.4 nm to  $-5.1 \pm 1.4 \times 10^2 \text{ nm}^3$  for the 6.3 nm nanoparticles.

**4.3. Small Angle X-ray Scattering.** In fig. 4.7 the measured scattering curves are plotted for different nanoparticle concentrations normalized to 1 at  $q$  is  $1.3 \text{ nm}^{-1}$ . The scattering curve of the lowest concentration sample can be fitted accurately by the form factor of spheres (black dots in fig. 4.7) indicating that in that case the system exhibits only single particle scattering and there is negligible interaction between the particles. For higher concentrations the scattering intensity is decreased at small  $q$  and increased at intermediate  $q$ , showing the appearance of correlations between the particles.

The structure factor (fig. 4.8) is calculated by dividing these normalized patterns by the form factor fitted to the lowest concentration data, see eq. 4.18. The structure factor shows a peak which shifts to large  $q$  when the concentration increases. This peak corresponds to the average distance between two scatterers in the system and therefore the average distance between the nanoparticles decreases with increasing concentration. For the highest concentrations, the center of this peak is at  $q = 0.78 \text{ nm}^{-1}$ , corresponding to a real space distance of 8.1 nm, slightly larger than the particle-particle distances obtained from the radial distribution function from cryo-TEM (7.5 nm).

The second virial coefficient can be obtained from the limit of the scattering vector going to zero, so the structure factor has to be extrapolated using the  $q^2$  dependence at small  $q$  as shown in fig. 4.9. Using this extrapolation, the structure factor at zero angle is obtained and shown in fig. 4.9(B) for two different particle sizes. According to eq. 4.7, the inverse structure factor should be a linear function of the concentration, with a proportionality constant of 2 times  $B_2$  and a y-intercept of 1. Fitting our data with this relation yields values of  $6 \pm 1 \times 10^2 \text{ nm}^3$  and  $1.1 \pm 0.4 \times 10^2 \text{ nm}^3$  for the second virial coefficient of the QDs with a diameter of 4.4 nm and 5.7 nm, respectively.

---

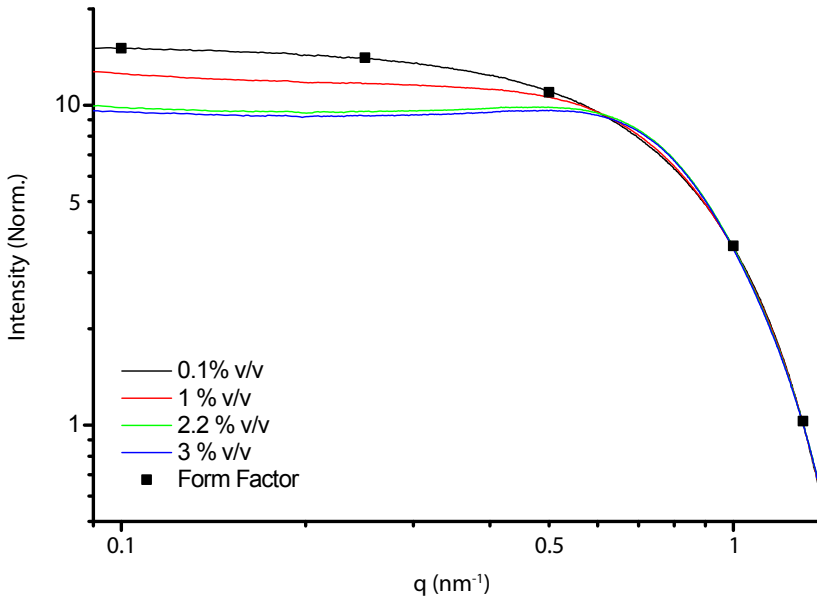


FIGURE 4.7. Radial X-ray scattering profiles for different concentrations of 4.4 nm PbSe quantum dots in decalin. The black dots are the calculated form factor, indicating that the lowest concentration shows only single particle scattering.

TABLE 4.1. Experimental values of the  $B_2$  obtained from cryo-TEM, Analytical Centrifugation (AC), and SAXS.

Diameter (nm)	Second Virial Coefficient ( $\text{nm}^3$ )		
	cryo-TEM	AC	SAXS
4.4		$80 \pm 50$	$592 \pm 104$
5.0	$185 \pm 209$		
5.3	$-251 \pm 120$	$-117$	
5.6	$-380 \pm 200$	$-120 \pm 108$	
5.7			$110 \pm 37$
6.0	$-183 \pm 303$		
6.3	$-826 \pm 520$	$-506 \pm 140$	
8.0	$-2237 \pm 200$		

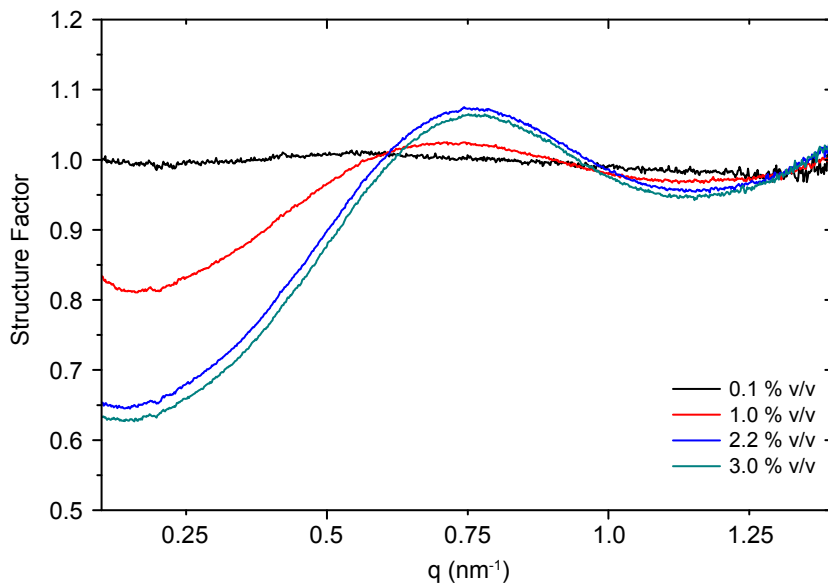


FIGURE 4.8. Structure factors of PbSe nanoparticles in decalin at increasing concentration obtained from X-ray scattering.

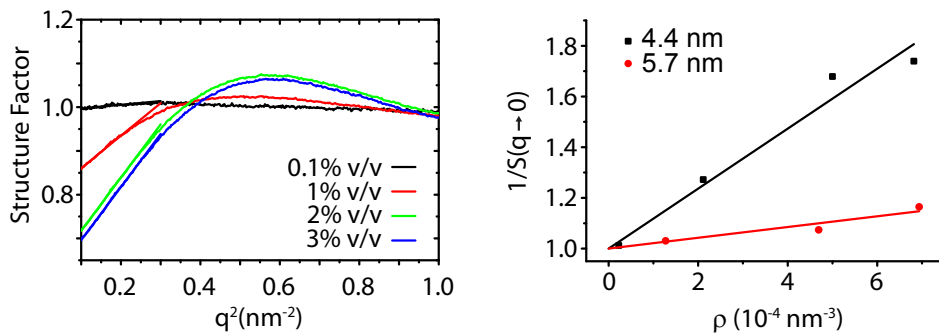


FIGURE 4.9. (A) The structure factor plotted as function of  $q^2$  for different concentrations. (B) The inverse of the structure factor at  $q \rightarrow 0$  as function of concentration.

## 5. Discussion

In fig. 4.10, the second virial coefficient is plotted as function of the particle diameter for the three methods used (see table 4.1), all showing a clear decrease of the  $B_2$  with increasing particle size. It is remarkable that, although

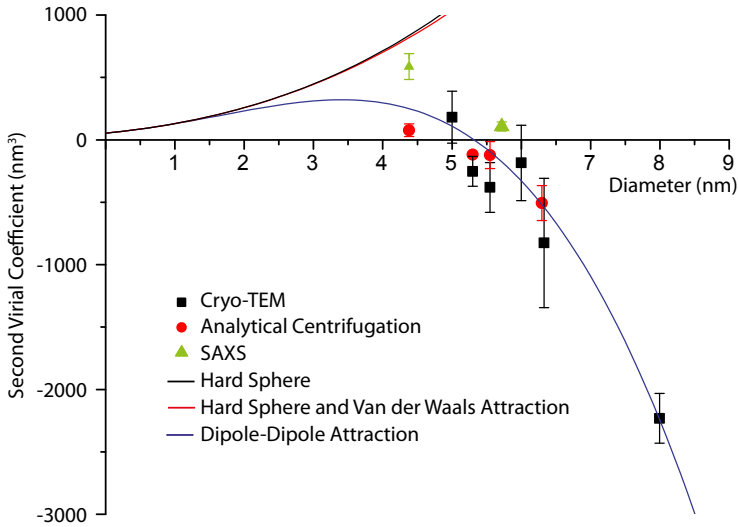


FIGURE 4.10. The second virial coefficient of PbSe nanoparticles dispersed in decalin plotted as function of size for the three techniques used. The solid lines are calculations based on purely hard spheres (black), hard spheres with the Van der Waals interaction, and a dipolar hard sphere interaction. For details of these calculations see text.

the  $B_2$  determined using cryo-TEM is derived from images of two-dimensional systems, whereas analytical centrifugation and SAXS are bulk measurements, all three methods yield similar values for the 3-dimensional  $B_2$ . This is because the calculation of the second virial coefficient from microscopy images is based on the assumption that the radial distribution function is the logarithm of the average interaction potential averaged over all nanoparticle orientations. Although the positions of nanoparticles are trapped in a two-dimensional liquid film, this does not restrict the rotational degrees of freedom of the particles and therefore the orientational average of the pair potential is the same as that of the bulk particles, such that a three-dimensional second virial coefficient can be calculated from these two-dimensional measurements.

The lines in fig. 4.10 are calculations based on different possible interactions between the nanoparticles. The hard sphere interaction predicts a continuously increasing second virial coefficient, which does not match with our results. If the

attractive Van der Waals interaction is taken into account, calculated via eqs. 1.4, 4.8 and 4.9 with a Hamaker constant of  $6 k_B T$ , its influence on the predicted second virial coefficients is negligible. The curve passing through the data-points in fig. 4.10 is a fit based on eqs. 4.11 and 4.13 using only  $n$  and  $p_0$  as fit parameters and take the reference diameter to be 1 nm. This gives a good description of the observed trend with an  $n$  of  $1.3 \pm 0.1$  and  $p_0$  equal to  $1.0 \pm 0.2 \times 10^{-28}$  Cm. For this fit it was assumed that the thickness of the capping layer is the difference between the core diameter and the average center-to-center distance determined from the radial distribution function,  $r_c \approx 1.5$  nm, although the results depend only slightly on the choice of  $r_c$ . The values for lambda in the studied size vary from 1.3 to 2.1, which is well within the range of 0 to 3 in which eq. 4.13 is valid. The value of  $n$  is close to unity, indicating that the dipole moment of the particles is almost proportional to the nanoparticle diameter (see eq. 4.12). This is in agreement with the result of Shim and Guyot-Sionnest [12] where they measured the electric dipole moment of CdSe and ZnSe quantum dots with a diameter between 2.5 nm and 6 nm using dielectric spectroscopy. For both materials the dipole moment was found to depend linearly on the nanoparticle size.

The origin of this dipole moment can be accounted for using the same reasoning as presented before by Shim and Guyot-Sionnest [12]. The PbSe quantum dots studied here consist of positive lead ions and negative selenium ions placed on a cubic rock-salt lattice. Each of the unit cells of this lattice is charge neutral and does not have an intrinsic dipole moment; therefore the core of the quantum dot can be considered as a neutral quasi-sphere. However, the atoms at the surface of this particle are not fully coordinated and contribute to the presence of localized surface charges. Most of these surface charges are compensated by the ligands adsorbed to the nanoparticle surface or are removed by reorganization of the interface. However, not all charges might be compensated and they might remain randomly distributed on the surface, giving rise to a net dipole moment of the particle. The magnitude of this dipole moment can be described as a random walk, giving an average dipole moment of  $p \propto \sqrt{N} \sigma_c$ , where  $N$  is the number of charges on the sphere. In this description, no restrictions are placed on the sign of the charges, indicating that these surface charges can be all positive, both positive and negative, or all negative. However, as the quantum dot as a whole is charge neutral both positive and negative surface charges are present. Comparing this prediction for the dipole moment with the size dependence of the dipole moment found in our experiments, only a weak dependence of the number of charges on

---

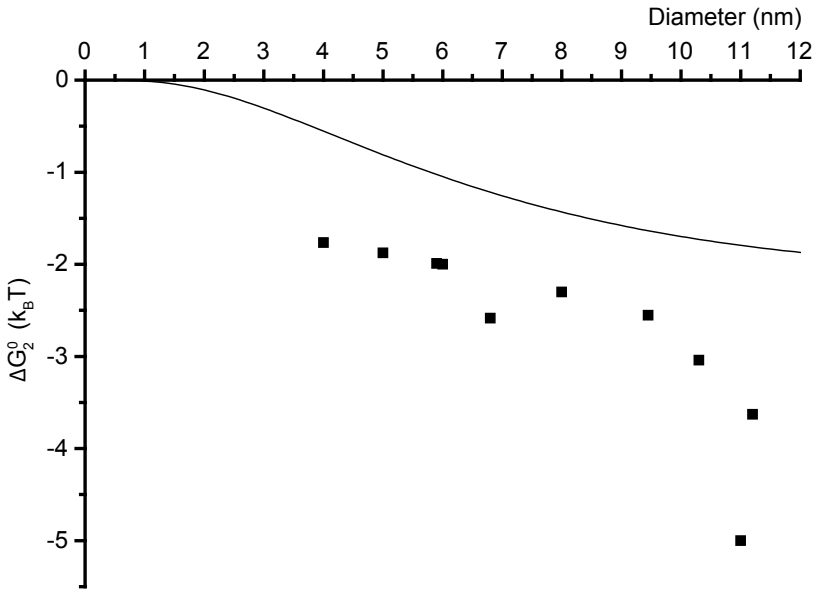


FIGURE 4.11. Coupling free energy as measured from cryo-TEM images plotted as function of size (dots) and the coupling free energy as predicted from the fluctuating dipole model used to describe the second virial coefficient.

the nanoparticle diameter is found. Shim and Guyot-Sionnest [12] attributed this effect to the faceted nature of the nanocrystal. These facets are nanometer sized and therefore the Coulomb energy would be extremely high between charges residing on the same facet, and thereby limiting the number of charges per facet. As long as the number of facets is independent of the nanocrystal size, it follows that the number of charges has to be constant as well.

From the coupling parameter  $\lambda$  used in this model (eq. 4.12), the contact free energy can be calculated via [5]:

$$(4.20) \quad V(r = \sigma) = -\frac{1}{3}k_B T \lambda^2$$

These values can be compared to the coupling free energy ( $\Delta G_2^0$ ) measured using cryo-TEM as described in chapter 2, shown in fig. 4.11. The calculated coupling free energies are comparable to the data from chapter 2, indicating that the interaction can be described by a dipole-dipole interaction.

## 6. Conclusions/Outlook

The second virial coefficient of PbSe quantum dots in decalin is obtained using three independent experimental techniques which yield similar results. A clear decrease in  $B_2$  is observed with increasing particle size due to the increasing contribution of the attractive interactions. The size dependence of the second virial coefficient can be explained by the dipolar hard sphere model using a dipole originating from a constant number of charges randomly distributed over the surface of a sphere. The agreement between the data from this experiment and from the experiments in chapter 2 gives further evidence that the dipole-dipole interaction is the dominant interaction between PbSe nanoparticles.

## Bibliography

- [1] A. Vrij and R. Tuinier. *Structure of Concentrated Colloidal Dispersions*, chapter 5. Elsevier, 2005.
  - [2] B. L. Neal, D. Asthagiri, O. D. Velev, A. M. Lenhoff, and E. W. Kaler. Why is the osmotic second virial coefficient related to protein crystallization? *J. Cryst. Growth*, 196(2-4):377–387, 1999.
  - [3] E. W. Fischer. Elektronenmikroskopische Untersuchungen zur Stabilität von Suspensionen in makromolekularen Lösungen. *Koll.-Zeit.*, 160(2):120–141, 1958.
  - [4] B. Luigjes, D. M. E. Thies-Weesie, B. H. Ern e, and A. P. Philipse. Sedimentation equilibria of ferrofluids: II. Experimental osmotic equations of state of magnetite colloids. *J. Phys. Condens. Matter*, 24(24):245104, 2012.
  - [5] A. P. Philipse and B. W. M. Kuipers. Second virial coefficients of dipolar hard spheres. *J. Phys. Condens. Matter*, 22(32):325104, 2010.
  - [6] F. Cousin, E. Dubois, and V. Cabuil. Tuning the interactions of a magnetic colloidal suspension. *Phys. Rev. E*, 68(2):021405, 2003.
  - [7] G. A. Vliegthart and H. N. W. Lekkerkerker. Predicting the gas-liquid critical point from the second virial coefficient. *J. Chem. Phys.*, 112(12):5364, 2000.
  - [8] B. Luigjes, D. M. E. Thies-Weesie, A. P. Philipse, and B. H. Ern e. Sedimentation equilibria of ferrofluids: I. Analytical centrifugation in ultrathin glass capillaries. *J. Phys. Condens. Matter*, 24(24):245103, 2012.
  - [9] W. G. McMillan and J. E. Mayer. The statistical thermodynamics of multi-component systems. *J. Chem. Phys.*, 13(7):276, 1945.
-



- [10] M. Klokkenburg, A. J. Houtepen, R. Koole, J. W. J. de Folter, B. H. Erné, E. van Faassen, and D. Vanmaekelbergh. Dipolar structures in colloidal dispersions of PbSe and CdSe quantum dots. *Nano Lett.*, 7(9):2931–2936, 2007.
  - [11] A. P. Hammersley. Fit2d: An introduction and overview, 1997. ESRF97HA02T.
  - [12] M. Shim and P. Guyot-Sionnest. Permanent dipole moment and charges in colloidal semiconductor quantum dots. *J. Chem. Phys.*, 111(15):6955, 1999.
-

### Appendix 4.A. Connection between $B_2$ and the Pair Potential

An expression for the virial coefficients can be obtained from statistical thermodynamics starting from the partition function:

$$(4.21) \quad Z = \frac{1}{N! \Lambda^{3N}} \int d\mathbf{r}^N \exp[\beta \Phi(\mathbf{r}^N)]$$

for a system with volume  $V$  and  $N$  particles with positions  $\mathbf{r}$  and inverse temperature  $\beta = 1/(k_B T)$ . The potential energy  $\Phi$  is given by:

$$(4.22) \quad \Phi(\mathbf{r}) = \sum_{i < j}^N \phi(|\mathbf{r}_i - \mathbf{r}_j|)$$

The partition function can be written as the product of an ideal part  $Z_0 = V^N/(N! \Lambda^{3N})$  and a correction  $Q$ :

$$(4.23) \quad Q = \frac{1}{V^N} \int d\mathbf{r}^N \exp[\beta \Phi(\mathbf{r}^N)]$$

Combining eqs. 4.22 and 4.23 and rewriting in terms of the Mayer functions  $f(r)$  yields:

$$(4.24) \quad Q = \frac{1}{V^N} \int d\mathbf{r}^N \prod_{i < j}^N (f(r_{ij}) + 1); \quad f(r) = \exp[\beta \phi(r)] - 1$$

This can be expanded into a sum of 0 and higher orders of  $f$ :

$$(4.25) \quad Q = \frac{1}{V^N} \int d\mathbf{r}^N \left( 1 + \frac{N(N-1)}{2} f(r_{12}) + \dots \right)$$

The pressure can be calculated via:

$$(4.26) \quad \begin{aligned} P &= -\frac{\partial F}{\partial V} = k_B T \frac{\partial \ln[Z]}{\partial V} = k_B T \frac{1}{Z} \frac{\partial Z}{\partial V} \\ &= k_B T \frac{Q}{Z} \frac{\partial Z_0}{\partial V} + k_B T \frac{\partial \ln[Q]}{\partial V} \end{aligned}$$

Combination of eq. 4.26 with  $Z_0$  and eq. 4.25 yields the virial expansion for the osmotic pressure:

$$(4.27) \quad P = k_B T \rho \left( 1 - \frac{1}{2} \rho \int d\mathbf{r} f(r) - \dots \right)$$

Comparison with eq. 4.3 yields the following expression for the second virial coefficient:

$$(4.28) \quad B_2 = -\frac{1}{2} \int d\mathbf{r} f(r) = -\frac{1}{2} \int d\mathbf{r} (\exp[-\phi(r)/(k_B T)] - 1)$$

Although the above relation is derived for a one component system it was shown by McMillan and Mayer [9] that for a multicomponent system the expressions are similar. The only difference is that instead of the pair potential, the potential of mean force  $V$  is used, which describes the average interaction free energy between two particles. For our specific case, this means that the interaction potential between two nanoparticles at a fixed distance is calculated while the other nanoparticles and solvent molecules are allowed to move freely. This way, the influence of these components is averaged out and an average interaction potential between the colloids is obtained.

### Appendix 4.B. Compressibility and Structure Factor

It is well known that fluctuations in the number of particles  $N$  in a volume  $V$  are related to the compressibility  $\kappa$  as:

$$(4.29) \quad k_B T \rho \kappa = \frac{\langle N^2 \rangle - \langle N \rangle^2}{\langle N \rangle}; \quad \kappa \equiv -\frac{1}{V} \frac{\partial V}{\partial P}$$

We can define the one- and two-body distribution functions in a homogeneous fluid:

$$(4.30) \quad \rho^{(1)}(\mathbf{r}) = \sum_i^N \delta(\mathbf{r}_i - \mathbf{r})$$

$$(4.31) \quad \langle \rho^{(1)}(\mathbf{r}) \rangle = \rho$$

$$(4.32) \quad \int_V d\mathbf{r} \langle \rho^{(1)}(\mathbf{r}) \rangle = \langle N \rangle$$

$$(4.33) \quad \rho^{(2)}(\mathbf{r}, \mathbf{r}') = \sum_{i,j}^N \delta(\mathbf{r}_i - \mathbf{r}) \delta(\mathbf{r}_j - \mathbf{r}')$$

$$(4.34) \quad \langle \rho^{(2)}(\mathbf{r}, \mathbf{r}') \rangle = \rho^2 g(|\mathbf{r} - \mathbf{r}'|)$$

$$(4.35) \quad \int_V d\mathbf{r} \int_V d\mathbf{r}' \langle \rho^{(2)}(\mathbf{r}, \mathbf{r}') \rangle = \langle N^2 \rangle - \langle N \rangle^2$$

Combining these with eq. 4.29 yields:

$$(4.36) \quad k_B T \rho \kappa = 1 + \rho \int d\mathbf{r} (g(r) - 1)$$

The structure factor is the fourier transform of the radial distribution factor via:

$$(4.37) \quad S(q) = 1 + \rho \int d\mathbf{r} \exp[i\mathbf{q}\mathbf{r}] (g(r) - 1)$$

Comparing these equations shows that the compressibility is related to the structure factor at  $q = 0$  as:

$$(4.38) \quad k_B T \rho \kappa = S(0)$$

Inserting the definition of  $\kappa$  we obtain:

$$(4.39) \quad k_B T \frac{\partial \rho}{\partial \Pi} = S(0)$$

# **Non-Regularized Inversion Method from Light Scattering Applied to Ferrofluid Magnetization Curves for Nanoparticle Size Distribution Analysis**

## **ABSTRACT**

A model-independent, non-regularized inversion method is applied to the analysis of magnetization curves of ferrofluids. This numerical method, originally used for the analysis of light scattering measurements, does not assume prior knowledge of the distribution shape of the particle sizes or magnetic dipole moments nor the presence of a single population of particles. Positive number densities are enforced via a non-negative least squares procedure. This inversion procedure is implemented in MINORIM available on the web. The method is successfully tested on real measurement data of ferrofluid samples with a known, multimodal size distribution. The robustness of the method is further demonstrated by numerical simulations with a test magnetic dipole moment distribution and Gaussian noise added to the generated superparamagnetic magnetization curves.

## 1. Introduction

Magnetic nanoparticles have many applications that are the subject of current research. For example, in cancer therapy, local hyperthermia is generated by heating the magnetic nanoparticles linked to cancer cells, through the use of an alternating magnetic field [1, 2]. Another promising biomedical technique is magnetic particle imaging (MPI) [3], which requires well-controlled frequency-dependent magnetic properties of the nanoparticles. Both of these biomedical applications ideally require magnetic particles that have exactly the same (size-dependent) magnetic resonance frequency [4, 5], to obtain a maximum response at that frequency. For these and other applications, it is important to know the magnetic properties of the nanoparticles and how they are distributed across the entire population of the nanoparticles. A widely adopted approach is to obtain the distribution of dipole moments from the magnetization of the sample as function of external magnetic field strength.

Often magnetization data are fitted using an a priori assumed particle size distribution shape which can be derived from the size distribution that is usually obtained from Transmission Electron Microscopy (TEM) analysis. Chantrell et al. [6] used a log-normal distribution, but other distributions such as a gamma function are used as well [7, 8]. The parameters of the log-normal distribution can either be derived from the low- and high-field limits of the magnetization curves [6, 7] or from fitting the complete magnetization curve [9, 10]. More advanced models can be proposed, like a core-shell model [11], to explain the discrepancy between the diameter acquired from magnetization measurements and the physical diameter as obtained from TEM-images. Although in principle it is possible to use multiple peaks to model multimodal systems, the increasing number of fit parameters makes the results less reliable and physically less meaningful.

For dynamic light scattering (DLS), there is a long tradition to obtain the particle size distribution from a system of colloidal particles in a liquid dispersion without a priori assumption of the distribution shape using discrete inversion methods [12]. Deriving particle size or magnetic dipole moment distribution information by applying inversion techniques also enters in the domain of analysis of magnetization measurements [13–17]. Using an analysis technique that does not assume any shape of the distribution, the generated magnetization curve belonging to the calculated distribution generally agrees better with the experimental one.

Nowadays, many different inversion methods are available, such as genetic algorithms [13], maximum entropy [18], singular value decomposition (SVD) [19],

---

simulated annealing [13], moment expansion [20], and non-negative least squares methods. The latter can be subdivided into a class of regularized methods, such as the CONTIN method [12, 21, 22], often used in dynamic light scattering [12], and non-regularized methods [23]. The reconstruction of the magnetic size distribution using these techniques is not trivial and not necessarily robust, as for example, the SVD method is highly sensitive to noise [6]. Moreover for a good reconstruction based on the moment expansion a minimal number of moments ( $\sim 10$ ) is necessary, but the higher the moment order, the harder it is to obtain reliable results. Although genetic algorithms can provide reliable distributions, these methods typically have a relatively high computational cost.

In this chapter, we demonstrate the application of a model-independent, non-regularized inversion method for the analysis of magnetization curves, adapted from a method designed by Strawbridge and Hallett [23] for the analysis of static light scattering (SLS) measurements. This method does not assume prior knowledge of the shape of the magnetic dipole moment distribution, or equivalently the magnetic size distribution, nor the presence of a single population of particles of similar average size (monomodal system). Using non-negative least squares procedures (NNLS), our method enforces positive number densities, unlike other methods that can give negative, unphysical results [15]. In this thesis, our procedure is applied to measurement data from Alternating Gradient Magnetometry (AGM) and from as Vibrating Sample Magnetometry (VSM) but it is applicable to any method that yield the sample magnetization as function of the external field strength.

In principle, our program is based on discrete sampling methods, originally developed by Pike et al. [24] as an exponential sampling technique and later improved by Morrison et al. [25]. With the NNLS procedure based on Lawson and Hanson [26], a short execution time is obtained on the order of seconds or less using a state-of-the-art personal computer.

In the next section, the mathematical foundation of our model-independent method is presented, followed by demonstration of the method on real measurement data of ferrofluid samples with a known, multimodal size distribution. The robustness of the method is investigated using simulations with a test magnetic dipole moment distribution and Gaussian noise added to the generated superparamagnetic magnetization curves.

---

## 2. Numerical Methods

For a dilute dispersion of monodisperse spherical magnetic nanoparticles, the magnetization  $M$  of the sample as function of the applied magnetic field  $H$  is described by the Langevin function  $L$ , with

$$(5.1) \quad M(H) = M_{\text{sat}} L(H, \mu) = M_{\text{sat}} \left( \coth(\alpha) - \frac{1}{\alpha} \right)$$

$$\alpha = \left( \frac{\mu \mu_0 H}{k_B T} \right)$$

where  $M_{\text{sat}}$  is the saturation magnetization,  $\mu$  is the magnetic dipole moment of a magnetic nanoparticle,  $\mu_0$  is the permittivity of vacuum,  $k_B$  is the Boltzmann constant, and  $T$  is the absolute temperature. In case of a monodisperse ferrofluid with number density  $n$ ,  $M_{\text{sat}}$  corresponds to the magnetization  $M_{\text{sat}} = n\mu$  when all magnetic dipoles are aligned in the limit of infinite applied field  $H$ . For a polydisperse or a multimodal dispersion, the magnetization is the sum of all contributing dipole moments, which for a continuous distribution of the number density  $P(\mu)$ , defined as the number of particles with a dipole moment between  $\mu$  and  $\mu + d\mu$ , can be written as a distribution integral:

$$(5.2) \quad M(H) = \int_0^{\infty} \mu L(H, \mu) P(\mu) d\mu$$

In order to obtain the magnetic dipole moment distribution  $P(\mu)$ , eq. 5.2 must be solved given the experimental magnetization curve  $M_{\text{exp}}(H)$  and using the Langevin factor  $L(H, \mu)$  from eq. 5.1. This is in general an ill-conditioned problem, as small experimental uncertainties such as noise can give rise to large, unphysical peaks in the distribution curve [12].

To address this problem, one can use discrete methods for which eq. 5.2 is rewritten in a discrete form. For this purpose, the magnetic dipole moment domain is subdivided into a histogram of  $N$  intervals of which each bin spacing  $\Delta_i$  has a center dipole moment  $\mu_i$  and a bin content equal to the number of the dipole moments  $n_i$  (see fig. 5.1). The experimental magnetization curve consists of  $J$  points  $M_j$  measured at a field strength  $H_j$  respectively. The discrete form of eq. 5.2 becomes:

$$(5.3) \quad M_{\text{exp}}(H_j) = \sum_{i=1}^N \mu_i L(H_j, \mu_i) n_i$$



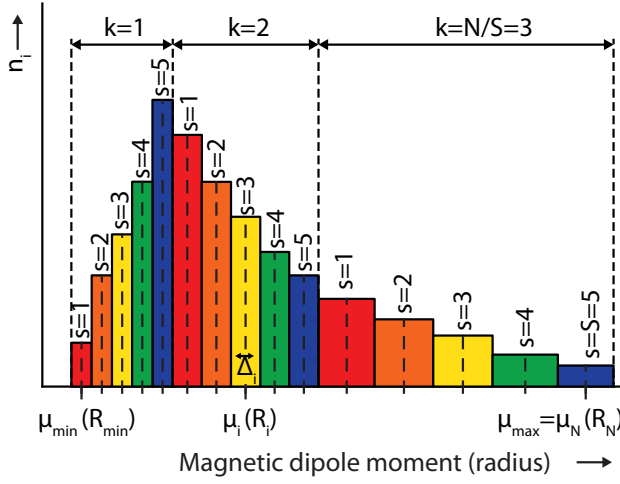


FIGURE 5.1. Histogram showing an example of a dipole moment distribution with the dipole moments  $\mu$  (or alternatively the particle radius  $R$ ) binned in  $N = 15$  geometrically spaced bins, subdivided into  $S = 3$  subdomains. The meaning of the y-axis values depends on the definition of the probability factor  $P(\mu)$  in the magnetization function (eq. 5.2).

The basis vector  $H_j$  contains the experimental values for the magnetic field strength, and the measurement output can be written as a column vector  $\mathbf{M}_{\text{exp}}$  with length  $J$ . We describe the Magnetic dipole moment Distribution (MD) by a column vector  $\mathbf{n}_{\text{MD}}$  with length  $N$  and elements  $n_i$  in a basis  $\mu_i$ . Utilizing a  $J \times N$  data transfer matrix  $\overleftrightarrow{\mathbf{T}}$  with matrix elements  $T_{ji}$  formed by the product  $\mu_i L(H_j, \mu_i)$  calculated using the Langevin theory (see eq. 5.1), eq. 5.3 can be summarized in terms of linear algebra with:

$$(5.4) \quad \mathbf{M}_{\text{exp}} = \overleftrightarrow{\mathbf{T}} \cdot \mathbf{n}_{\text{MD}}$$

Without experimental uncertainties, the number distribution  $\mathbf{n}_{\text{MD}}$  can be solved from eq. 5.4. Due to noise and other measurement uncertainties, statistical methods are needed to obtain the best magnetic dipole moment distribution  $n_i$  in terms of minimizing the mean squares deviation  $\xi^2$ :

$$(5.5) \quad \xi^2 = \|\mathbf{M}_{\text{exp}} - \overleftrightarrow{\mathbf{T}} \cdot \mathbf{n}_{\text{MD}}\|^2$$

Note that this result is obtained without a priori knowledge of the shape (e.g., *log-normal* or *Gaussian*) of the dipole moment distribution. Alternatively, the problem can be defined in the particle size domain rather than the dipole moment domain via  $\mu = (4/3)\pi r^3 m_s$  where  $r$  is the particle radius and  $m_s$  the bulk saturation magnetization of the studied material.

Often, regularization methods are used in order to make the problem less ill-conditioned. In Dynamic Light Scattering, the CONTIN method [12, 21, 22] based on the algorithm of Tikhonov [27, 28] is a well-known example. A mathematical regularizing term is added to eq. 5.5 to force a smooth outcome of the probability distribution  $n_i$ . The regularizer is the square norm of the first or higher order derivative of the distribution function  $n_i$  itself, multiplied by a regularization strength parameter  $\lambda$  which determines the influence of this regularization term. The result is a mean squared deviation  $\xi^2$  that is low when a smooth distribution is obtained because then the derivatives of this function are small.

Another class of inversion methods are the non-regularization methods, which Strawbridge and Hallett [23] applied to the analysis of Static Light Scattering measurements. We adopt this method here to treat data of magnetization measurements. A minimum  $\mu_{min}$  and maximum  $\mu_{max}$  magnetic dipole moment determine the range allowed. The range can be divided into  $N$  discrete parts represented by a center value  $\mu_i$ , where the index  $i$  runs from 1 to  $N$ . Although a linear spacing is possible, in this work the bins are spaced according to a geometrical series:

$$(5.6) \quad \mu_i = \mu_{min} \left[ \left( \frac{\mu_{max}}{\mu_{min}} \right)^{1/(N-1)} \right]^{i-1}$$

This distribution favors the smaller dipole moments, as for smaller dipole moments the number of bins in an interval  $\Delta\mu$  is larger than for a similar interval at higher dipole moments. As each bin has an equal weight in the inversion algorithms, this gives an higher weight to the smaller dipole moments. This is recommended because the particles contribute with a weight factor proportional to their dipole moment to the total signal and therefore the magnetization curve is dominated by the larger particles.

The essence of the non-regularization method used here is to split the range of  $N$  intervals into  $S$  subdomains, each with index  $s$  and elements  $n_s$ :

$$(5.7) \quad \mathbf{n}_s = (\mu_s, \mu_{S+s}, \mu_{2S+s} \dots \mu_{(k-1)S+s}, \dots)^T$$

$$k = 1, \dots, \frac{N}{S}; \quad s = 1, \dots, S; \quad \frac{N}{S} \in \text{Integer}$$

For each subdomain  $\mathbf{n}_s$  eq. 5.4 is solved by minimizing the mean squared deviation  $\xi^2$  (eq. 5.5). The vector representing the magnetization measurement  $\mathbf{M}_{exp}$  is unaltered, but an adapted version of the data transfer matrix  $\overleftrightarrow{\mathbf{T}}_s$  with dimension  $J \times N/S$  is used based on subdomain  $\mathbf{n}_s$ . Finally the subdomain distributions are merged into the total probability distribution  $\mathbf{n}_{psd}$ .

To ensure that a solution is obtained which has physical meaning, the constraint is imposed that each  $n_i$  in eq. 5.5 must be positive. For this purpose a non-negative least mean squares method is applied, developed by Lawson and Hanson [26] implemented in Mathematica [29]. An additional benefit of the non-negative constraint is that eq. 5.4 is less ill-conditioned.

The choice of the total number of bins depends on the desired resolution of the reconstructed dipole moment distribution. A large number  $N$  of different discrete magnetic dipole moments gives a high resolution in the magnetic dipole moment (or size) range but can give rise to noisy peaks in the probability distribution. With this solution one can reconstruct a precise magnetization curve. This is the optimal choice for a system with low polydispersity or for a system where different populations are present that have almost similar dipole moments. With a small number  $N$  of intervals, a smooth probability distribution is obtained with the disadvantage of a peak broadening or indistinguishable peaks in case of a multimodal system. The latter is comparable to a high regularization parameter  $\lambda$  in regularization methods. The mean squared deviation  $\xi^2$  is increased in case of a small number of intervals, meaning a lower quality of the fit of the magnetization curve. For a polydisperse system, i.e., a broad distribution, a small number of intervals can be acceptable. The number of subdomains  $S$  has an optimum related to the number of intervals  $N$  because a small number of subdomains does not eliminate the ill-condition of the inversion problem, while a large number of subdomains will result in broadening of the distributions.

Often, the first bins of the histogram, representing small magnetic dipole moments (or particle sizes), contain noise. To arrive at an objective cutoff value that discriminates between the noise and the ‘real’ part of the signal, we utilize the fact that smaller magnetic moments require a higher magnetic field  $H$  to reach the saturation magnetization. Experimental factors impose a limit to the maximum magnetic field that can be reached, and therefore one can calculate the minimum magnetic moment that can be measured with that particular system (for details see appendix 5.C). Values below this threshold should be interpreted carefully.

Our procedure is implemented in the computer program MINORIM, available for several platforms [30].

### 3. Experimental Methods

**3.1. Ferrofluid Synthesis.** The magnetic particles used to demonstrate the inversion method are nearly monodisperse magnetite nanoparticles synthesized by single-step thermal decomposition of iron oleate synthesized according to a chemical recipe from the Hyeon group [31] and described as the “sphere synthesis” by Luigjes et al. [10]. Two batches of particles were prepared containing magnetite particles with a diameter of 6.4 nm and 10.5 nm, respectively, with the surfaces coated with oleic acid and dispersed in the solvent *cis/trans*-decalin (Merck, for synthesis).

**3.2. Electron Microscopy.** Transmission electron microscopy on these samples is performed using a Philips Tecnai 12 electron microscope operated at 120 keV. For each sample the size distribution is obtained by measuring the diameter of 200-300 particles with iTEM software (Olympus, Münster, Germany)

**3.3. Alternating Gradient Magnetometry.** For the preparation of the magnetic samples used in this work, the saturation magnetization of the two nanoparticle dispersions was measured, and two stock dispersions were prepared with approximately equal saturation magnetization. From these stock solutions, mixtures were prepared with well defined amounts of large and small particles.

The magnetization curves were measured with Alternating Gradient Magnetometry (AGM) using a Princeton Micromag Model 2900. The absence of magnetic interactions in the samples was ensured by comparing the shapes of the normalized magnetization curve with a normalized magnetization curve after dilution by a factor of 10, which in absence of dipole-dipole interactions should be equal.

**3.4. Data Correction and Analysis.** The first step in the analysis of the magnetization curves was the correction for any non-superparamagnetic behavior, such as diamagnetic contributions, based on the fact that the high field part of the magnetization curve is independent of the distribution of the dipole moments and only depends on the average dipole moment in the system. By fitting the data with a hyperbolic function, the diamagnetic contribution was determined and subtracted from the raw data. This corrected magnetization curve is used as input for the inversion routine, which returns the experimental particle size

---

distribution  $\mathbf{n}_{\text{exp}}$ . An overview of the complete analysis algorithm is shown in appendix 5.A. For the conversion from magnetic dipole moment to magnetic radius, we assume spherical particles with a volume magnetization equal to the magnetite bulk magnetization of 480 kA/m [10].

**3.5. Numerical Simulations.** The limits of this inversion method were tested with numerical simulations of magnetization curves. The basis vector for the simulated distributions is chosen geometrically with approximately 10 times more points per decade than used in the inversion method, to mimic a continuous distribution. The number distribution vector  $\mathbf{n}$  is filled with a mono- or bi-modal distribution for which the bin content is log-normally distributed with known average dipole moment and standard deviation. This distribution was inserted in eq. 5.4, which then yields the simulated magnetization curve,  $\mathbf{M}_{\text{sim}}$ , with a base vector  $\mathbf{H}$  containing the same values for the magnetic field strength as the experimental data. Finally, Gaussian noise was added to the magnetization curve with standard deviations from 0.001% to 1% of the saturation magnetization, which are typical values for experimental systems. This simulated magnetization curve was used as input for the inversion routine to obtain the simulated size distribution  $\mathbf{n}_{\text{sim}}$ .

## 4. Results and Discussion

The applicability of our inversion method is tested both with experimental data and numerical simulations. In the first part of this section we show the results of the analysis of a mixture of small (6.4 nm) and large (10.5 nm) nanoparticles mixed in different ratios. In the second part we will explore the limits of the inversion method using simulations of different magnetic size distributions.

**4.1. Experiments.** Figure 5.2 compares the number distribution of magnetic sizes obtained with the inversion method and the particles sizes from TEM image analysis. Both distributions contain two distinct peaks, corresponding to the large and small particles mixed to obtain the magnetic sample. The magnetic radius ( $R_M$ ) is smaller for both peaks than the physical particle size ( $R_P$ ). This is a well-known effect [11] due to the weaker paramagnetism of the surface layer of the nanoparticles. In our case, the difference between the magnetic radius and TEM radius is about 1 nm for both the small and large particles, consistent with a surface effect.

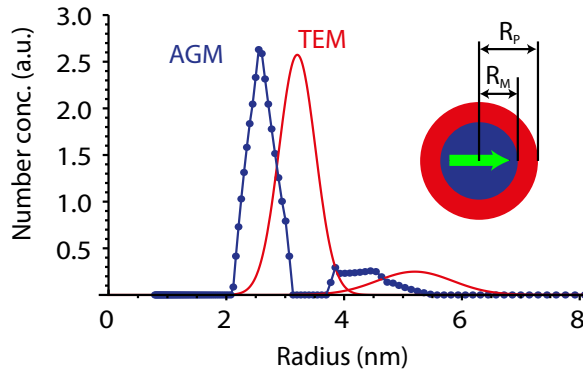


FIGURE 5.2. The particle size distribution from magnetic measurements, (AGM, blue dots) and TEM (red line). The inset shows a schematic picture of a magnetic nanoparticle with a magnetic core and a shell with weaker magnetic properties, indicating the origin of the discrepancy between the magnetic ( $R_M$ ) and TEM ( $R_P$ ) radii.

The most common method to analyze the magnetization curves of ferrofluids is a fit assuming a log-normal distribution. Figure 5.3 compares both fit methods on the same sample. The inversion method shows a residual that is centered around zero, evidenced by the histogram of the deviations in fig. 5.3 D. The autocorrelation of these residuals (data not shown) shows the absence of any correlation, indicating that the residuals are randomly distributed around zero, which confirms the goodness of the fit. The log-normal distribution is not able to describe the system properly as is clearly visible by the systematic deviations from zero in the residual (fig. 5.3 B). As the noise level on this magnetization curve is typical for experimental data, the histogram in fig. 5.3 D indicates that the noise on the experimental measurements is Gaussian, with a standard deviation on the order of 0.1% of the saturation magnetization.

To obtain statistics on the reliability of the results, 10 measurements were performed on 3 different samples containing small and large particles, of which two are duplicates and a third one is diluted by a factor of 10. In fig. 5.4 the averaged magnetic particle size distributions are shown of the sample, with the error bars indicating the standard deviation for each bin. As expected, all curves show two separate peaks, even the low concentration sample, for which the standard deviation of the noise is 10% of the saturation magnetization. The two samples

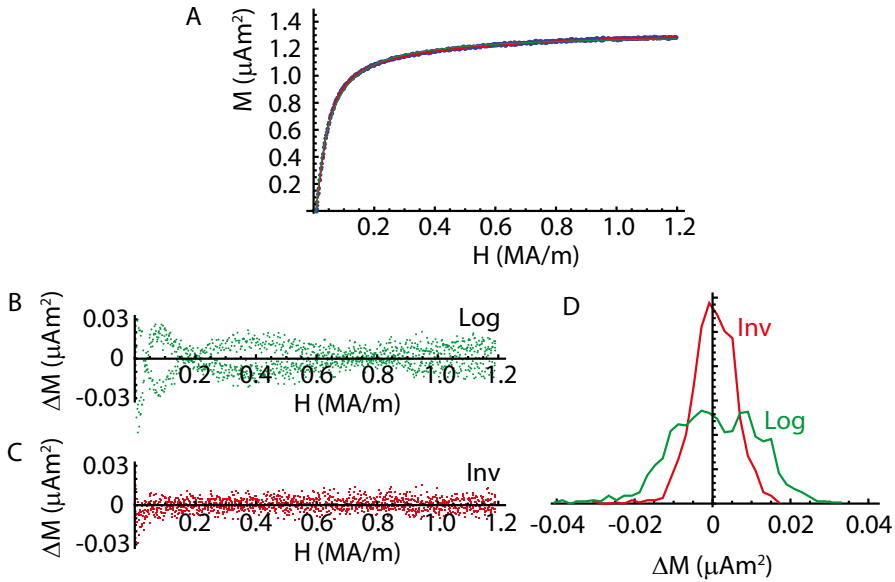


FIGURE 5.3. (A) Comparison between a fit with a log-normal model (Log, green) and the inversion method described in this work (Inv, red) and residuals of the log-normal fit (B) and the inversion method (C). (D) Shows the histogram of the residuals.

with the same high concentrations yield practically indistinguishable results, which confirms the reproducibility of the inversion method.

An important criterion to judge the applicability of the inversion method is whether the intensity of the peaks in the resulting dipole moment distribution is related to the amount of the corresponding fraction of the particles. We tested this requirement by creating mixtures with different amounts of the two monodisperse stock dispersions and measured the magnetization curve. From the results of the analysis of the magnetization curves with the inversion method, the volumetric fraction of the small particles is calculated, shown in appendix 5.B as function of the experimental volume fraction of the small particles in the mixture. The solid line has a slope of unity and corresponds well with our data, indicating that the peak area is proportional to the contribution of the particles to the total magnetization.

**4.2. Simulations.** The main variables that influence the quality of the final fit are noise (see fig. 5.4), the range of sampling points of the magnetization curve,

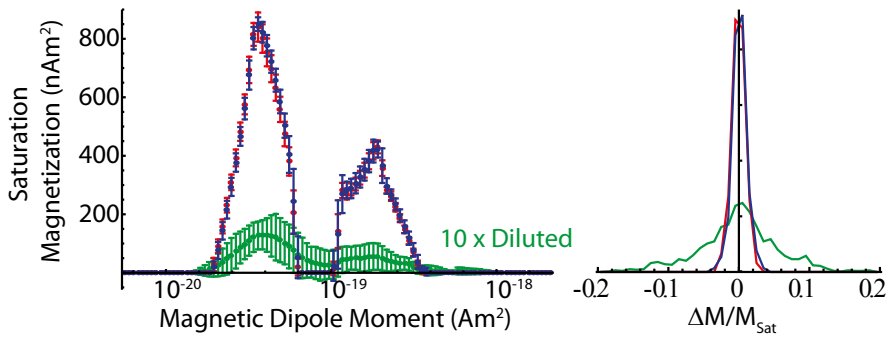


FIGURE 5.4. Dipole moment distributions averaged over 10 different measurements on two duplicate samples containing small and large particles mixed in a magnetization ratio of 1.97. Both samples yield indistinguishable distributions with a ratio of the peak areas of 1.96. The third sample is diluted by a factor of 10 and has a poor signal-to-noise ratio ( $\Delta M/M_{Sat}$ , see histogram on the right) but still yields a similar distribution.

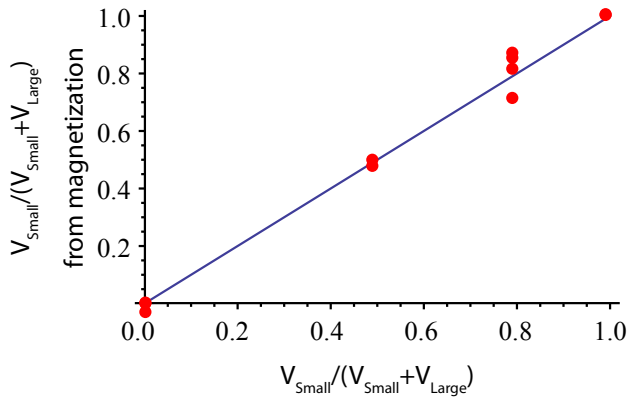


FIGURE 5.5. Volume ratio of small particles dispersion ( $V_{Small}$ ) to the total sample volume ( $V_{Small} + V_{Large}$ ) obtained from the analysis of magnetic measurements with the inversion method plotted as function of the volume ratio of the two components in the sample. The solid line has a slope of unity.



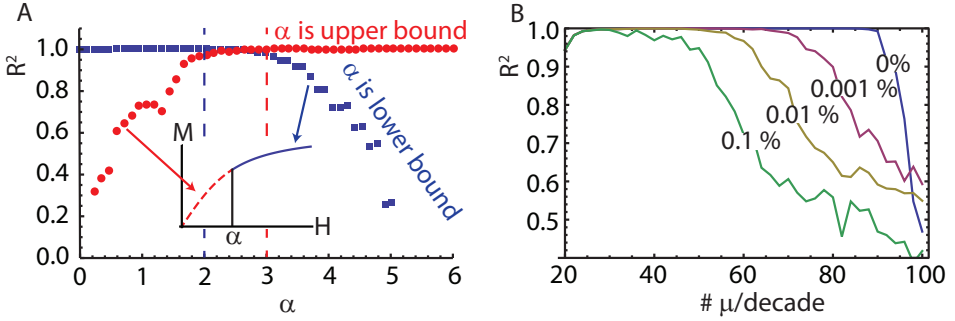


FIGURE 5.6. (A) Fit quality expressed in an  $R^2$  parameter (see eq. 5.8) for dimensionless magnetic field strengths from 0 to  $\alpha$  (circles) and from  $\alpha$  to  $\alpha = 10$  (squares), indicated in the inset by the corresponding colors. The region where both ranges yield a reasonable fit contains most information about the distribution shape. (B) The correlation coefficient plotted as function of the number of dipole moment values per decade used for the calculated distribution. With increasing noise the agreement at high number of dipole moments per decade decreases. The same happens at a low number of dipole moments per decade, due to insufficient resolution to resolve the sharp peaks.

and the number  $N$  of sampling dipole moments. In this section the influence of these parameters on the final result using simulated magnetization curves is investigated. To quantify the agreement between the simulated dipole moment distribution and that obtained from the inversion method we use the  $R^2$  value, defined as:

$$(5.8) \quad R^2 = 1 - \frac{\sum_{\mu} (\mathbf{n}_{\text{exp}}(\mu) - \mathbf{n}_{\text{sim}}(\mu))^2}{\sum_{\mu} (\mathbf{n}_{\text{exp}}(\mu) - \langle \mathbf{n}_{\text{exp}}(\mu) \rangle)^2}$$

where  $\mathbf{n}$  is the dipole moment distribution function from the simulated (Sim, sampled at  $\mu_{\text{Exp}}$ ) and analyzed (Exp) dataset. The summation runs over all values of  $\mu$  present in the fitted distribution above the threshold calculated from the maximum magnetic field strength, see appendix 5.C.

The Langevin curve at small field strength and high field strength only depends on the average dipole moment (see Supporting Information) and does not contain any information on the shape of the distribution. The boundaries of the useful

region containing the information about the magnetic distribution can be found by analyzing the minimal and maximal field strengths for which a good fit is acquired with the inversion method. In fig. 5.6 A, the fit quality of the theoretical dipole distribution is calculated from magnetization curves at field strengths from 0 to  $\alpha$  (disks) and from  $\alpha$  to 6 (squares), where  $\alpha$  is the dimensionless magnetic field strength (see eq. 5.1). To obtain a dipole moment from the inversion method similar to the simulated distribution, all information about the distribution must be present in the analyzed part of the magnetization curve. The upper bound of this range is found by analyzing magnetization curve with increasing maximum field strength till the  $R^2$  value comes close to 1, which is for  $\alpha > 3$ . The lower limit is obtained similarly by varying the lowest magnetic field value till the goodness of the fit deviates from 1, which happens for  $\alpha > 2$ . From these two boundaries it becomes clear that all information about the size distribution is located between  $\alpha \approx 2$  and  $\alpha \approx 3$  and a good quality of the measurement in this region is required. Figure 5.6 B shows the fit quality, expressed as  $R^2$ , as function of the number of bins per decade of the histogram used to reconstruct the distribution. At low resolution, the peaks are broadened and therefore the fit quality is lowered. If the number of dipole moments per decade becomes too high, i.e., insufficient “regularization”, the fit quality is also decreasing. The onset of this decrease depends on the noise but for typical experimental systems this is always above 40 dipole moment values per decade.

In fig. 5.7, the average dipole moment and the standard deviation of the distribution are compared by plotting the average dipole moment or standard deviation of the reconstructed dipole moment distribution as function of the simulated standard deviation or average dipole moment. In both graphs the solid line has a slope of unity and represents agreement between simulation and calculation. In fig. 5.7 B, the average dipole moment of a sample with 1% Gaussian noise is shown, which is worse than the noise in most experiments, but the agreement between simulated and fitted average dipole moment is still good. The same holds for the standard deviation. Although the scatter is much stronger if the sample has a high noise level, in both cases the results follow the ‘best fit’ line well. This good agreement shows that, although the noise might be too high to obtain a reliable distribution, the integrated results are still physically meaningful. The final test for this analysis method is its capability to separate two distinct distributions. In fig. 5.8, an example is shown with different dipole moment ratios, with a noise standard deviation of 0.1%. In this example, the calculated dipole

---

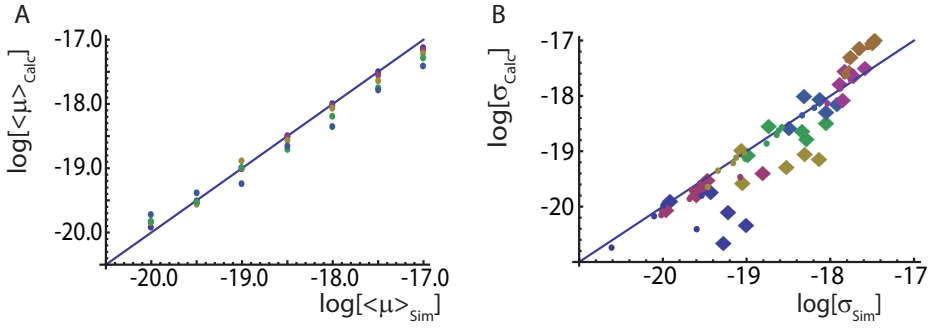


FIGURE 5.7. (A) The calculated average dipole moment plotted against the simulated average dipole moment and (B) the simulated and calculated standard deviations of a simulation with 0.01% noise (circles) and 1% noise (diamonds). In both cases the agreement is good.

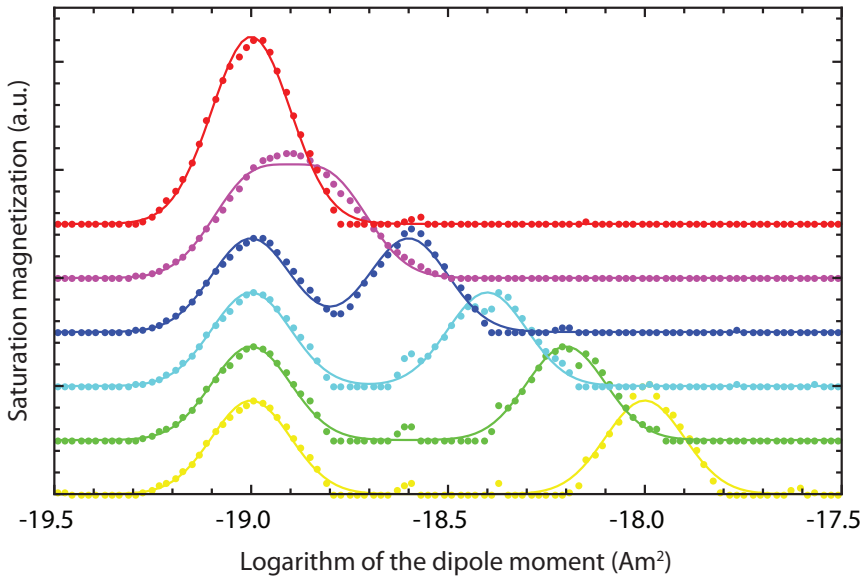


FIGURE 5.8. Comparison of the simulated (solid line) and calculated (dots) distribution for a bimodal system with different dipole moment distributions. The curves are shifted vertically for clarity.

moment distributions are in good agreement with the theoretical distribution, but this agreement strongly depends on both the noise and number of dipole moment values per decade.

## 5. Conclusion

In this chapter, we have demonstrated an inversion method previously used to analyze light scattering data and now applied to the analysis of magnetization curves. With this method the magnetic size distribution of single-domain nanoparticles in ferrofluids can be resolved independently of an a priori assumed size distribution shape. Both with experimental data and numerical simulations, the resulting size distribution is in good agreement with the initial size distribution of the particles or the dipole moment distribution used as input for the numerical simulations. Using this method it is possible to obtain the shape of the particle size or dipole moment distribution from AGM, VSM, or other measurement techniques that yield the magnetization curves of magnetic fluids.

---

---

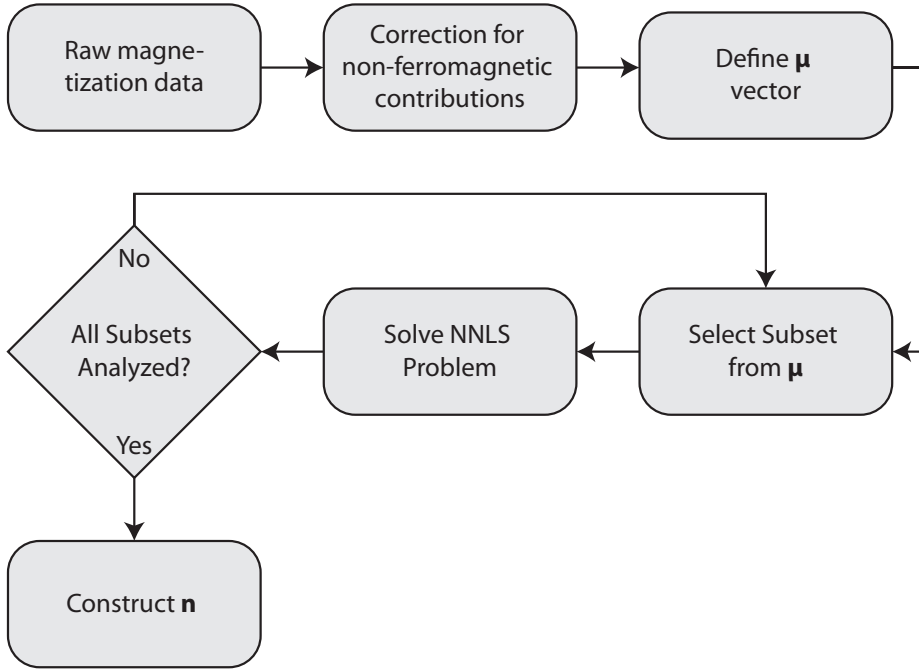
## Bibliography

- [1] Q. A. Pankhurst, J. Connolly, S. K. Jones, and J. Dobson. Applications of magnetic nanoparticles in biomedicine. *J. Phys. D: Appl. Phys.*, 36(13):R167–R181, 2003.
  - [2] K.M. Krishnan. Biomedical nanomagnetism: A spin through possibilities in imaging, diagnostics, and therapy. *IEEE Trans. Magn.*, 46(7):2523–2558, 2010.
  - [3] B. Gleich and J. Weizenecker. Tomographic imaging using the nonlinear response of magnetic particles. *Nature*, 435:1214, 2005.
  - [4] M. Klokkenburg, C. Vonk, E. M. Claesson, J. D. Meeldijk, B. H. Ern e, and A. P. Philipse. Direct imaging of zero-field dipolar structures in colloidal dispersions of synthetic magnetite. *J. Am. Chem. Soc.*, 126:16706, 2004.
  - [5] R.E. Rosensweig. Heating magnetic fluid with alternating magnetic field. *J. Magn. Magn. Mater.*, 252:370, 2002.
  - [6] R. W. Chantrell, J. Popplewell, and S. W. Charles. Measurements of particle size distribution parameters in ferrofluids. *IEEE Trans. Magn.*, 14(5):975–977, 1978.
  - [7] M. Ra a. Magnetic properties and magneto-birefringence of magnetic fluids. *Eur. Phys. J. E*, 2(3):265–275, 2000.
  - [8] A. Ivanov, S. Kantorovich, E. Reznikov, C. Holm, A. Pshenichnikov, A. Lebedev, A. Chremos, and P. J. Camp. Magnetic properties of polydisperse ferrofluids: A critical comparison between experiment, theory, and computer simulation. *Phys. Rev. E*, 75(6):1–12, 2007.
  - [9] J.C. Bacri, R. Perzynski, D. Salin, V. Cabuil, and R. Massart. Magnetic colloidal properties of ionic ferrofluids. *J. Magn. Magn. Mater.*, 62(1):36–46, 1986.
  - [10] B. Luigjes, S. M. C. Woudenberg, R. De Groot, J. D. Meeldijk, H. M. Torres Galvis, K. P. De Jong, A.P. Philipse, and B. H. Ern e. Diverging geometric and magnetic size distributions of iron oxide nanocrystals. *J. Phys. Chem. C*, 115(30):14598–14605, 2011.
  - [11] D. X. Chen, A. Sanchez, E. Taboada, A. Roig, N. Sun, and H.C. Gu. Size determination of superparamagnetic nanoparticles from magnetization curve. *J. Appl. Phys.*, 105(8):083924, 2009.
  - [12] W. Brown. *Dynamic light scattering: the method and some applications*. Clarendon Press, Oxford, 1993.
-

- [13] A. Kákay, M. W. Gutowski, L. Takacs, V. Franco, and L. K. Varga. Langevin granulometry of the particle size distribution. *J. Phys. A: Math. Gen.*, 37(23):6027–6041, 2004.
  - [14] G. Lei, K. R. Shao, Y. B. Li, G. Y. Yang, Y. Guo, J. Zhu, and J. D. Lavers. Bayesian inversion method and its information determination for the estimation of particle size distribution in ferrofluids. *IEEE Transactions on Magnetics*, 45(10):3981–3984, 2009.
  - [15] T. Weser and K. Stierstadt. Discrete particle-size distribution in ferrofluids. *Zeit. Phys. B-Cond. Mat.*, 59(3):253–256, 1985.
  - [16] D. V. Berkov, P. Görnert, N. Buske, C. Gansau, J. Mueller, M. Giersig, W. Neumann, and D. Su. New method for the determination of the particle magnetic moment distribution in a ferrofluid. *J. Phys. D: Appl. Phys.*, 33:331, 2000.
  - [17] J. A. Potton, G. J. Daniell, A. D. Eastop, M. Kitching, D. Melville, S. Poslad, B. D. Rainford, and H. Stanley. Ferrofluid particle-size distributions from magnetization and small-angle neutron-scattering data. *J. Magn. Magn. Mat.*, 39(1-2):95–98, 1983.
  - [18] J. Skilling and S. Sibisi. *Maximum entropy and Bayesian methods : proceedings of the Fourteenth International Workshop on Maximum Entropy and Bayesian Methods : Cambridge, England, 1994*. Kluwer Academic Publishers, Dordrecht; Boston, 1996. ISBN 0792334523 9780792334521. ID: 34990181.
  - [19] W. H. Press. *Numerical recipes : the art of scientific computing*. Cambridge University Press, 2007.
  - [20] V. John, I. Angelov, A. A. Öncül, and D. Thévenin. Techniques for the reconstruction of a distribution from a finite number of its moments. *Chem. Eng. Sci.*, 62(11):2890–2904, 2007.
  - [21] S. W. Provencher. A constrained regularization method for inverting data represented by linear algebraic or integral-equations. *Comput. Phys. Commun.*, 27(3):213–227, 1982.
  - [22] S. W. Provencher. Contin - a general-purpose constrained regularization program for inverting noisy linear algebraic and integral-equations. *Comput. Phys. Commun.*, 27(3):229–242, 1982.
  - [23] K. B. Strawbridge and F. R. Hallett. Size distributions obtained from the inversion of  $I(Q)$  using integrated light-scattering spectroscopy. *Macromolecules*, 27(8):2283–2290, 1994.
-

- [24] E. R. Pike, D. Watson, and F. M. Watson. *Measurement of Suspended Particles by Quasi-Elastic Light Scattering*. John Wiley and Sons, 1983.
  - [25] I. D. Morrison, E. F. Grabowski, and C. A. Herb. Improved techniques for particle-size determination by quasi-elastic light-scattering. *Langmuir*, 1(4): 496–501, 1985.
  - [26] C. L. Lawson and R. J. Hanson. *Solving least squares problems*. Prentice-Hall, Englewood Cliffs, 1974.
  - [27] A. N. Tikhonov. Solution of incorrectly formulated problems and regularization method. *Soviet Mathematics (translation)*, 4:1035–1038, 1963 1963.
  - [28] A. N. Tikhonov. *Numerical methods for the solution of ill posed problems*. Kluwer, Dordrecht, 1995.
  - [29] M. D. Woodhams and M. D. Hendy. Reconstructing phylogeny by quadratically approximated maximum likelihood. *Bioinformatics*, 20:348–354, 2004.
  - [30] J. van Rijssel and B. W. M. Kuipers. Minorim inversion method. <http://hdl.handle.net/10411/10164>, 2013.
  - [31] J. Park, K. An, Y. Hwang, J.-G. Park, H.-J. Noh, J.-Y. Kim, J.-H. Park, N.-M. Hwang, and T. Hyeon. Ultra-large-scale syntheses of monodisperse nanocrystals. *Nat. Mater.*, 3:891, 2004.
-

### Appendix 5.A. Outline of the Algorithm



A flowchart of the implementation of the analysis method presented in this chapter is shown above. Starting with the raw M-H data obtained from the measurements, the first step is correction for non-ferromagnetic linear contributions like diamagnetic signals. The mathematical foundation of this procedure is described in appendix 5.C.

In the next step the base vector of the dipole moment distribution is constructed using a geometric distribution of dipole moments within a specified minimum and maximum dipole moment. The number of points is defined as the number of subsets times the number of dipole moments per subset.

For each subset the reconstruction is performed by minimizing  $\chi^2$  using a NNLS algorithm developed by Lawson and Hanson [26]. If the reconstruction is complete for all subsets, the final distribution histogram is constructed from the subset histograms, and this final distribution is saved to disk.



## Appendix 5.B. High and Low Field Approximations

The magnetization of a ferrofluid of (magnetically) polydisperse spherical nanoparticles can be described as:

$$(5.9) \quad M(H) = N \int \mu P(\mu) L(\mu, H) d\mu + \chi_{dia} H$$

Here we will determine the shape of  $M(H)$  in the low-field limit (i.e.,  $\alpha \rightarrow 0$ ) and the high-field limit (i.e.,  $\alpha \rightarrow \infty$ ).

**5.B.1. Low-Field Limit.** The Langevin equation in the low-field limit simplifies to:

$$(5.10) \quad L(\alpha) = \frac{\alpha}{3} = \frac{\mu_0 \mu H}{3k_B T}$$

Inserting this into eq. 5.9 we obtain:

$$(5.11) \quad M(H) = N \int \mu P(\mu) \alpha / 3 d\mu + \chi_{dia} H$$

which simplifies to:

$$(5.12) \quad M(H) = N \frac{\mu_0 H}{3k_B T} \int \mu^2 P(\mu) d\mu + \chi_{dia} H$$

$$(5.13) \quad = N \frac{\mu_0 H}{3k_B T} \langle \mu^2 \rangle + \chi_{dia} H$$

**5.B.2. High-Field Limit.** For  $\alpha \rightarrow \infty$ , the term  $\coth(\alpha) = 1$  and by plugging in the definition of  $\alpha$  we obtain:

$$(5.14) \quad M(H) = N \int \mu P(\mu) \underbrace{\coth(\alpha)}_{=1} d\mu - N \int \mu P(\mu) \frac{1}{\alpha} d\mu + \chi_{dia} H$$

$$(5.15) \quad = N \int \mu P(\mu) d\mu - N \frac{k_B T}{\mu_0 H} \int P(\mu) d\mu + \chi_{dia} H$$

$$(5.16) \quad = N \langle \mu \rangle - N \frac{k_B T}{\mu_0 H} + \chi_{dia} H$$

$$(5.17) \quad = N \langle \mu \rangle \left( 1 - \frac{k_B T}{\mu_0 \langle \mu \rangle H} \right) + \chi_{dia} H$$

$$(5.18) \quad = M_s \left( 1 - \frac{k_B T}{\mu_0 \langle \mu \rangle H} \right) + \chi_{dia} H$$

where  $M_s = N \langle \mu \rangle$

In conclusion, it is shown that in the limits of high and low field, the magnetization curve is independent of the shape of the distribution, i.e., the integral

can be solved analytically, and these limits can therefore be used to correct the distribution from non-Langevin contributions.

### Appendix 5.C. Diamagnetic Correction

Before the analysis of the experimental magnetization curves obtained with AGM, in most cases, a correction for the diamagnetic contribution has to be applied. This correction is especially important for the outcome of the analysis in the small dipole regime. In this section the method for this correction is described and its influence on the detection of small dipoles is discussed.

The full experimental magnetization curve,  $M(H)$ , can be described as:

$$(5.19) \quad M(H) = N \int \mu P(\mu) L(\mu, H) d\mu + \chi_{dia} H$$

where  $N$  is the total number of particles in the sample,  $P(\mu)$  the number fraction of particles with a dipole moment  $\mu$ ,  $L(\mu, H)$  the Langevin function,  $\chi_{dia}$  the total diamagnetic contribution and  $H$  the magnetic field strength. In appendix 5.B we derived for the high-field part of the magnetization curve:

$$(5.20) \quad M(H) = M_s \left( 1 - \frac{k_B T}{\mu_0 \langle \mu \rangle H} \right) + \chi_{dia} H$$

where  $\langle \mu \rangle$  is the average dipole moment of the sample. By fitting this to the high field region of the magnetization curve, the saturation magnetization, the diamagnetic contribution, and the average dipole moment can be obtained. The magnetic field region where this method can be applied depends on the smallest dipole moment present. Or the other way around, the choice of the high field boundary determines the lowest possible value for  $\mu$  that can be obtained. The approximation of the Langevin function is valid if  $\alpha$  is larger than 3 (see fig. 5.9). By combining this condition with equation 15 we obtain at room temperature:

$$(5.21) \quad \mu H > 0.98 \times 10^{-14} \text{ A}^2 \text{ m}$$

This means that for a typical high field range of  $H > 10^6 \text{ A/m}$ , the minimal dipole moment which can be measured is:  $\sim 1 \times 10^{-20} \text{ Am}^2$ . However, the choice of this boundary does not influence the minimal dipole moment too much. Even if this boundary is  $5 \times 10^5 \text{ A/m}$  (half our experimental field range) the minimal dipole moment increases with a factor of 2. This implies also that most of the information is present in a small portion of the data (see discussion of fig. 5.6).

---

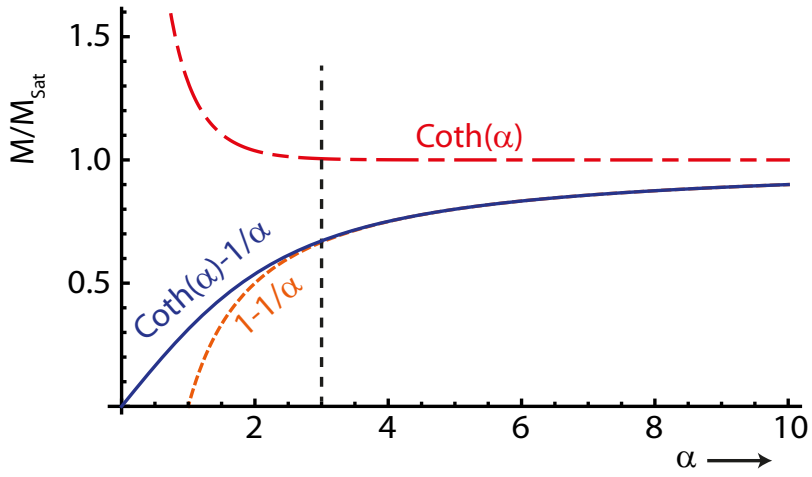


FIGURE 5.9. The Langevin equation (solid line) and approximations. Above  $\alpha = 3$ , the hyperbolic cotangent part (long dash) is approximately 1 and the Langevin equation can be described by the hyperbolic part (short dash) only.



## CHAPTER 6

# Synthesis of Monodisperse Cobalt Nanoparticles for their Self-Assembly into Binary Superlattices

### ABSTRACT

Nanoparticles of different materials can be organized in self-assembled structures, while retaining their unique size-dependent properties. In this chapter the self-assembly of magnetic cobalt nanoparticles and semiconductor PbSe quantum dots, with a diameter of respectively 13 and 6.7 nm, is examined. It is shown that in the presence of a horizontal magnetic field, magnetically aligned superstructures with an  $\text{AlB}_2$  crystal lattice are obtained.

The formation of large scale single-crystalline superlattices requires monodisperse nanoparticles. Our method to synthesize high-quality magnetic cobalt nanoparticles utilizes glass test tubes as reaction vessels. The high surface-to-volume ratio allows for efficient and uniform heating of the system, yielding favorable reaction conditions for homogeneous nucleation. The rapidity and robustness of this method is used to investigate the role of the surfactants and solvent in the synthesis of the magnetic nanoparticles.

## 1. Introduction

Nanoparticle solids of core/shell nanoparticles with a magnetic core and a semiconductor shell are known to exhibit semiconductor-type transport properties with magneto-resistance typical for magnetic tunnel junctions [1]. For further control over the collective properties of such materials, it is necessary to tune the properties of the magnetic and semiconductor nanoparticle components independently of each other. A further level of control can be obtained from the structure of the nanoparticle solid via the formation of so-called binary nanoparticle superlattices [2]. This self-assembly of different types and sizes of nanoparticles into an ordered superlattice is achieved via evaporation of the solvent from a droplet of a nanoparticle dispersion on a tilted substrate [3] or on a liquid sub-phase [4]. With these methods, a large variety of crystal structures is obtained [2] depending on the relative sizes [5] and interactions of the nanoparticles [6].

For long-range order in the superlattice, nanoparticles with a low polydispersity of at most 5% are necessary. To achieve such a low polydispersity various different synthesis methods have been developed, such as hot injection [7, 8] or heating up [9] methods.

Cobalt is a well studied strongly magnetic material, which has promising properties for magnetic [10, 11] as well as catalytic [12, 13] applications. It is known that cobalt nanoparticles with a low polydispersity and good magnetic properties can be obtained using a heating up method [9]. The magnetic properties of a superstructure formed with these nanoparticles not only depend on the magnetic properties of the individual nanoparticles but also on the mesoscopic structure of the assembly. For example, close-packed lattices [8], linear chains [14, 15], or two-dimensional monolayers with mesoscopic voids [16] each show unique magnetic properties [17]. Further processing of carefully designed superstructures, for example by attachment of the individual nanoparticles via oxidation [18, 19], provides well defined materials that can be used in for example lithium-ion batteries [20] or gas sensors [21].

The mid- to near-IR band gap of lead selenide nanocrystals makes them promising candidates for optoelectronic applications in for example solar cells [22], transistors [23] or photodiodes [24]. The structure of superlattices with PbSe and other semiconductor or metallic nanoparticles has been shown to depend on the size ratio between the components [25], the composition of the sub-phase [26], and the reaction temperature [6].

---

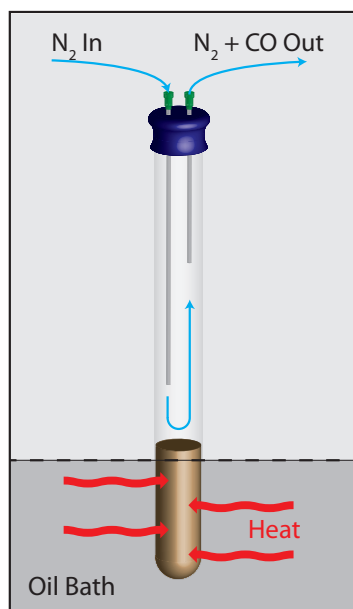


FIGURE 6.1. Schematic image of the test tube containing the reactants used in the synthesis of the cobalt nanoparticles immersed in the oil bath.

In this chapter, first a minimalistic method for the synthesis of cobalt nanoparticles is presented. As already shown by Timonen et al. [9], fast injection of the precursors into hot solvent is not necessary to split nucleation and growth; instead, using a heating up method yields similar results. In the method investigated here, the heating up stage was shortened by putting the reaction mixture directly into a preheated oil bath, thereby creating an as constant as possible temperature during the whole synthesis. Second, the self-assembly of these cobalt nanoparticles with the PbSe nanoparticles into binary superlattices is investigated. As one of the components is strongly magnetic, the influence of magnetic fields on the formed assemblies is studied as well.

## 2. Experimental

**2.1. Synthesis of Cobalt Nanoparticles.** For a typical experiment, a stock surfactant solution was prepared by dissolving 24 mg oleic acid (Sigma Aldrich

>99%) and 13.3 mg trioctylphosphine oxide (Sigma Aldrich 99%) in 2 mL *o*-dichlorobenzene (Sigma-Aldrich >99%). In a borosilicate glass test tube with a length of 129 mm and a diameter of 13 mm, 72 mg dicobalt octacarbonyl (STREM 95% stabilized with hexane) was mixed with 2 mL of the surfactant solution. The temperature- and oxygen-sensitive dicobalt octacarbonyl was stored in a freezer and only transferred into a nitrogen flushed glovebox (< 10 ppm O<sub>2</sub>) just before use. The test tube was sealed with a rubber septum and taken out of the glovebox and connected to a nitrogen flow as shown in fig. 6.1. The gas input was connected to the long needle (130 mm gauge 21), which was initially placed below the liquid interface. The outlet needle (38 mm gauge 21) was connected to a Brooks Instrument Sho-Rate model 1355 flow meter and a bubbler. The reaction mixture was bubbled with nitrogen for 2 minutes at a purging rate of 0.8 mL/s after which the input needle was lifted to just below the septum and the nitrogen flow was reduced to 0.2 mL/s. The test tube was then put in a preheated oil-bath for 30 minutes while stirring with two magnetic stirbars, one in the oilbath and one in the test tube. Subsequently, the test tube was transferred to a room temperature water bath to quench the reaction. During this process, the temperature inside the test tube was monitored using a Measurement Computing USB-501-TC-LCD logging thermometer. Finally, the input needle was lowered to just below the liquid interface and the reaction mixture is flushed for 2 minutes with nitrogen at a rate of 0.8 mL/s to remove dissolved carbon monoxide. The needles were then removed and the test tube was transferred to the glovebox for washing and storage.

**2.2. Solvent Exchange of the Cobalt Nanoparticles.** Typically, the synthesized cobalt nanoparticles tend to aggregate when transferred to other solvents than dichlorobenzene. However, via a route comprising ligand exchange and partial oxidization of the nanoparticle interface, the particles can be transferred to different solvents. To this end, a drop of 20  $\mu$ L trioctylphosphine (TOP, Sigma Aldrich 90%) was added to approximately 1 mL of crude sample which was then exposed to air for 30 min. The particles were subsequently precipitated by centrifugation with a Beckman Coulter Microfuge for 1 hour at 12400 rpm, and the precipitate was then redispersed in toluene.

**2.3. Synthesis of PbSe Nanoparticles.** In the synthesis of PbSe NCs, standard airless techniques (Schlenk line and nitrogen glove box) were used. The synthesis is based on the method of Kovalenko et al. [7]: 0.95 g lead chloride (99.999%, Sigma-Aldrich) and 17.5 mL oleylamine (90%, Aldrich) were combined

---



and the mixture was heated to 160°C. At this temperature a mixture of 1.2 g selenium (99.99%, Strem Chemicals) dissolved in 10 mL trioctylphosphine (90%, Sigma Aldrich) and 2.5 mL Sn[N(SiMe<sub>3</sub>)<sub>2</sub>]<sub>2</sub> (Sigma-Aldrich) was fast injected. The mixture was reheated to 140°C and afterwards it was allowed to cool to room temperature in 30 minutes. Oleic acid (90%, Sigma-Aldrich, 15 mL) was slowly added, followed by the addition of 40 mL methanol (Sigma-Aldrich, anhydrous, 99.8%) to precipitate the particles. After centrifugation (2500 *g*, 5 minutes), the supernatant was removed and the quantum dots (with a diameter of 6.7 ± 0.5 nm) were dispersed in toluene.

**2.4. Superlattice Formation.** In a typical experiment, a glass well with a diameter of 2.5 cm and a depth of 0.5 cm was covered with a minimal amount of ethylene glycol (EG), just sufficient to cover the bottom of the well. The ethylene glycol was subsequently preheated to the desired temperature. On top of the EG, 100 µL of a nanoparticle dispersion containing a mixture of cobalt nanoparticles and PbSe nanoparticles in hexane or toluene with a concentration of 1 to 10 mg/mL was gently put. When all hexane was evaporated, TEM-samples of the self-assembled structures were obtained by pressing a TEM-grid carefully on these freshly formed structures and lifting them from the EG interface. The remaining EG on the grid was removed under vacuum (<1 mbar) for approximately two hours at room temperature.

### 3. Results

**3.1. Synthesis of Cobalt Nanoparticles.** At a reaction temperature of 160°C, spherical cobalt nanoparticles with an average size of 9.6 nm and a polydispersity of 4.6% are typically obtained. Repeating this synthesis 8 times yielded slightly varying results, with average diameters from 8.3 nm to 10.1 nm and polydispersities from 4% to 6%. In some cases, instead of the desired narrow one-peak distribution (fig. 6.2 A, B), two peaks, both broader than the single desired peak were obtained (fig. 6.2 C, D). Of these, the larger particles represented the desired main product of the synthesis, while the smaller ones that sometimes appeared were in the minority. The average particle size is only weakly dependent on the reaction temperature, as it shifts from 11 nm at 145°C to 8 nm when the synthesis is performed at 165°C (fig. 6.2 E).

In fig. 6.3 A, the temperature evolution is shown for a typical synthesis at a reaction temperature of 156°C. The immersion of the test tube in the oil bath results in a fast increase of the temperature of the reaction mixture and rapid

---

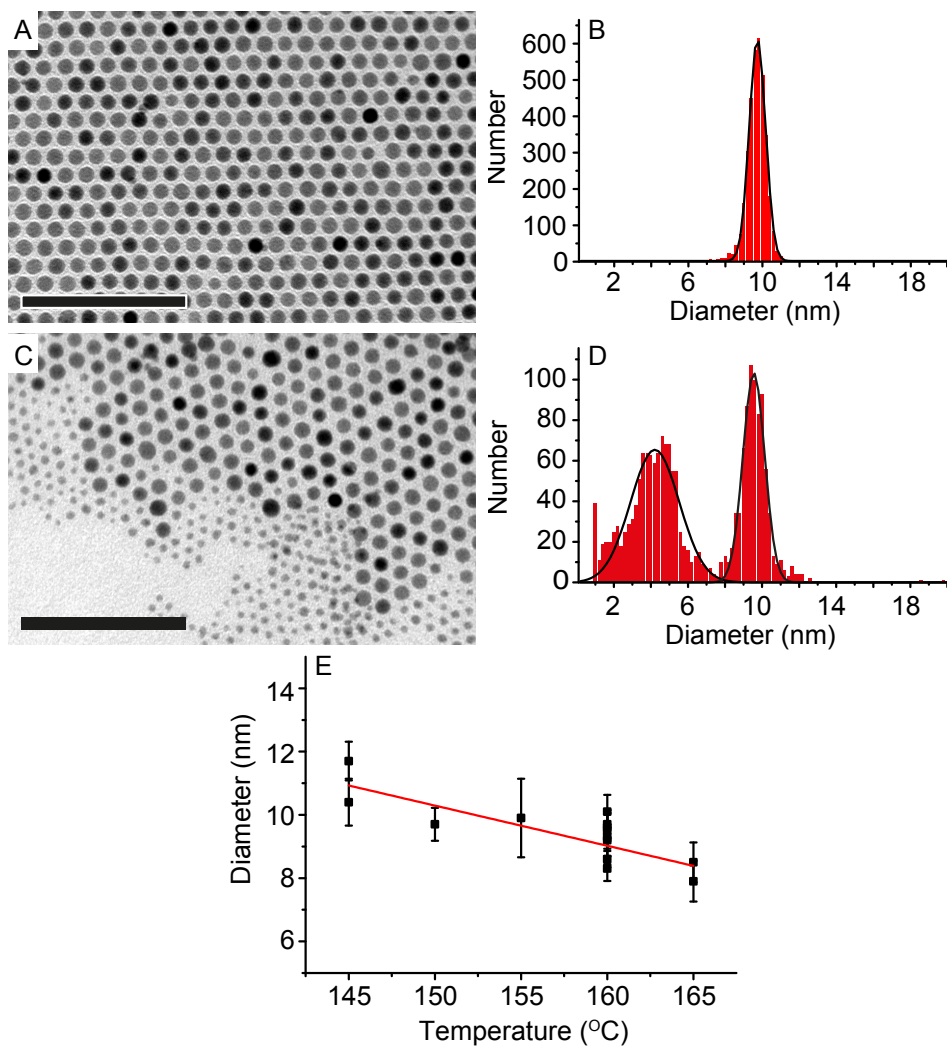


FIGURE 6.2. (A) TEM image and (B) particle size distribution of a typical monodisperse synthesis result with a particle diameter of  $9.7 \pm 0.4$  nm. The scale bars represent 100 nm. (C, D) Similar as A and B but now for a bidisperse synthesis result with particle diameters of  $4.1 \pm 1.3$  nm and  $9.6 \pm 0.6$  nm for the two fractions. (E) Average particle size as function of the reaction temperature.

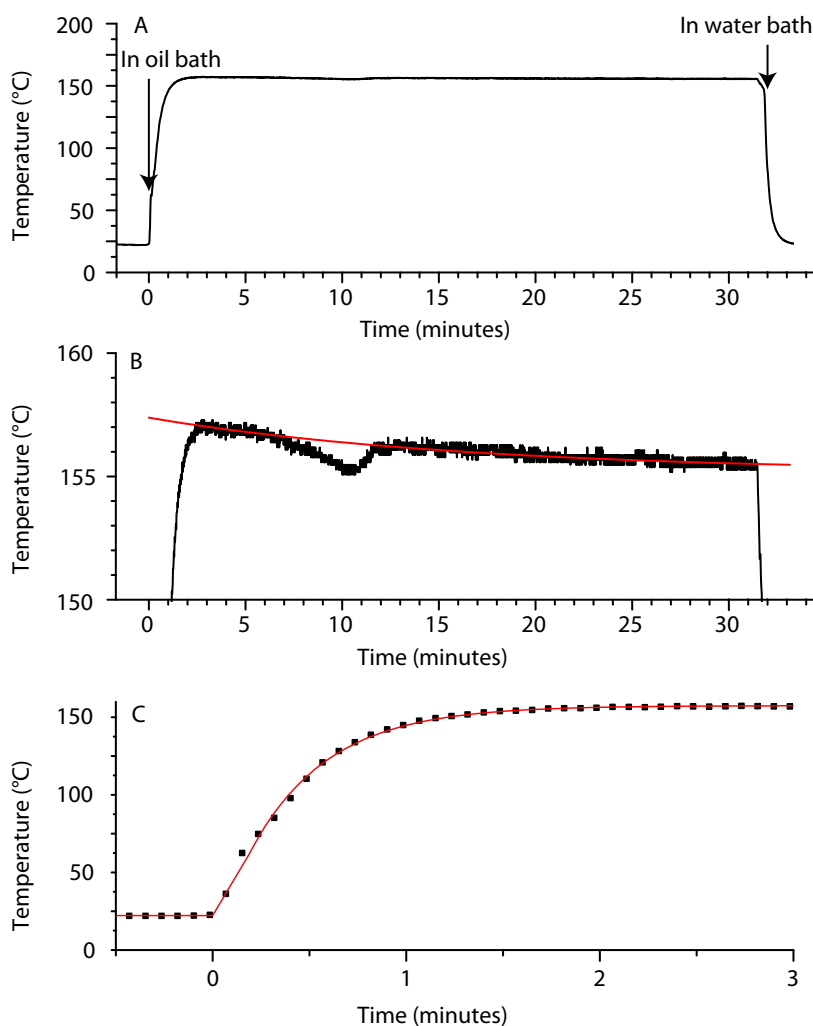


FIGURE 6.3. (A) Temperature-time profile for a typical cobalt nanoparticle synthesis; the arrows show the points where the test tube is immersed in the oil or water bath. (B) Close-up of the temperature drop due to the endothermic reaction; the red line gives the approximate oil bath temperature. (C) Fit of the initial part of the temperature evolution with eq. 6.1.

equilibration to the oil bath temperature, yielding nearly isothermal reaction conditions (fig. 6.3 B). The initial heating up and equilibration is described by the exponential law:

$$(6.1) \quad T(t) = T_{\text{RT}} + (T_{\text{Oil}} - T_{\text{RT}}) (1 - \exp[-t/\tau])$$

where  $T_{\text{RT}}$  is room temperature,  $T_{\text{Oil}}$  is the temperature of the oil bath, and  $\tau$  is characteristic time constant for the temperature equilibration. This time constant is system-specific; it depends on the thermal conductivities, the geometry of the test tube, the heat capacity and volume of the reaction mixture, and the stirring rate of both the oil and the reaction mixture. For our setup the time constant was measured to be 25 seconds, corresponding to an initial heating rate on the order of  $300^\circ\text{C}/\text{min}$  (fig. 6.3 C). After equilibration, the reaction temperature remained nearly constant throughout the reaction, and this was limited only by the stability of the oil bath (see the red line in fig. 6.3 B). However, despite the efficient coupling between the reaction mixture and the oil bath, a distinct spontaneous temperature drop of ca.  $1^\circ\text{C}$  due to the thermally decomposing carbonyl is observed after 6-11 minutes in a reaction run at  $156^\circ\text{C}$  (fig. 6.3). In comparison, a temperature drop of approximately  $10^\circ\text{C}$  is observed in heating up experiments wherein polydispersities of 7-8% are achieved using the same reaction. [9] This temperature drop was explained to quench the nucleation, thereby separating nucleation and growth, causing the reported low polydispersities. However, this explanation is not supported here, as nanoparticles with even smaller polydispersities are obtained despite the mild temperature drop in the test tube method.

The nucleation and growth of the cobalt nanoparticles can be rationalized by the LaMer scheme [27]. The accumulation of cobalt atoms from the isothermally decomposing  $\text{Co}_2(\text{CO})_8$  leads to the nucleation of the nanoparticles when the critical supersaturation is reached. Subsequently, the nuclei grow into mature nanoparticles by consuming the remaining and still forming molecular species [28, 29]. Beyond this qualitative description, it is challenging to explain how certain chemistries and synthesis methods lead to formation of nearly monodisperse particles while others result in considerably more polydisperse particles. In this case, clearly it is not necessary to inject the cobalt precursor at an elevated temperature, in an attempt to achieve a separation between nucleation and growth [29], and neither does the  $10^\circ\text{C}$  spontaneous temperature drop play a role. It is interesting to observe that the precursor injection at an elevated temperature was shown to be unimportant also in the synthesis of monodisperse CdSe and CdTe quantum

---

dots [30]. It remains an open question whether cobalt, CdSe and CdTe are individual cases or if other hot-injection methods could be converted into non-injective methods as well.

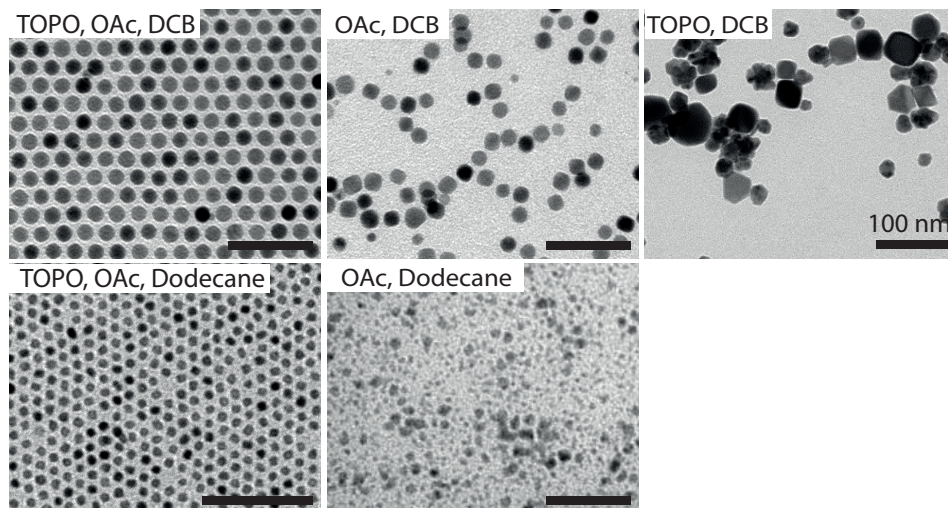


FIGURE 6.4. TEM images of synthesis results with varying solvents, dichlorobenzene (DCB) or dodecane, and ligands oleic acid (OAc) or trioctylphosphine oxide (TOPO). The scale bar represents 100 nm for all images.

The reaction mixture consists of three components that can coordinate with cobalt and therefore play a role in the reaction mechanism of the formation of the cobalt nanoparticles; namely, the solvent dichlorobenzene and the ligands oleic acid and trioctylphosphine oxide. To study the effect of each of these components, several syntheses are performed with varying compositions of the reaction mixture. In fig. 6.4, TEM images of typical synthesis outcomes of these reactions are shown. The reference synthesis, containing oleic acid, TOPO, and DCB, gives an average size of  $9.7 \pm 0.4$  nm. When DCB is replaced with the non-coordinating solvent dodecane, the average particle size becomes much smaller ( $4.2 \pm 0.5$  nm) and the shape of the particles is more erratic. On the other hand, when TOPO is excluded from the reaction mixture, the particle size does not change significantly, but the particle shape becomes more cubic. When the synthesis is performed with only oleic acid without TOPO or dichlorobenzene, the result is a sample containing small (3 nm) and very polydisperse ( $> 25\%$ ) nanoparticles. On the

other hand, when oleic acid is excluded from the reaction mixture, the synthesis yields relatively large particles of 40 nm. From these results, it is clear that all three components are required to obtain monodisperse, quasi-spherical nanoparticles.

**3.2. Solvent Exchange.** In order to use these cobalt dispersions for the formation of binary superlattices, the high boiling-point solvent DCB has to be replaced by a more volatile solvent. Washing the cobalt nanoparticles via precipitation with antisolvent and subsequent redispersion in an apolar liquid like toluene or hexane typically results in unstable dispersions. However, via a capping exchange with trioctylphosphine, combined with mild oxidation of the cobalt surface, the particles can be made stable in other apolar solvents. In fig. 6.5, the magnetic properties of cobalt nanoparticles with an diameter of about 8.5 nm are analysed using MINORIM (see chapter 5) before and after the oxidative washing step. The cobalt bulk magnetization of 1432 kA/m is used to convert the magnetic dipole moment into the magnetic diameter. The magnetic size distribution before solvent exchange (squares) consists of two peaks that are attributed to the bimodal size distribution as can be seen from the corresponding TEM image. From the magnetic measurements the particles have a magnetic diameter of  $8.9 \pm 1.5$  nm which corresponds well to the average size of  $9.6 \pm 0.4$  nm of the nanoparticles determined from TEM images. After solvent exchange, the size distribution changed in two ways: first, the fraction of small particles is removed, because they are too small to precipitate during the centrifugation step. The second change is a decrease of the magnetic diameter of the large particles to 8.2 nm, which can be interpreted as the formation of a weak-magnetic oxide shell around the particles.

One of the consequences of this washing method is that the formation of the oxide shell slows down further oxidation of the nanoparticles. This reduces one of the greatest disadvantages of cobalt magnetic nanoparticles, namely the difficult handling in air.

**3.3. Binary Self-Assembly of Co and PbSe Nanoparticles.** The formation of binary superlattices of magnetic and semiconductor nanoparticles is explored using the self-assembly method of Dong et al. [4]

In fig. 6.6 representative TEM images are shown for a system containing 13 nm cobalt nanoparticles and 6.7 nm PbSe nanoparticles, self-assembled at different temperatures of the ethylene glycol sub-phase. Taking into account the ligand-shell surrounding the particles ( $\sim 2$  nm) these have a size ratio of 0.63 for which, in the case of hard spheres, an AlB<sub>2</sub>-like structure is predicted [25]. This is exactly what

---

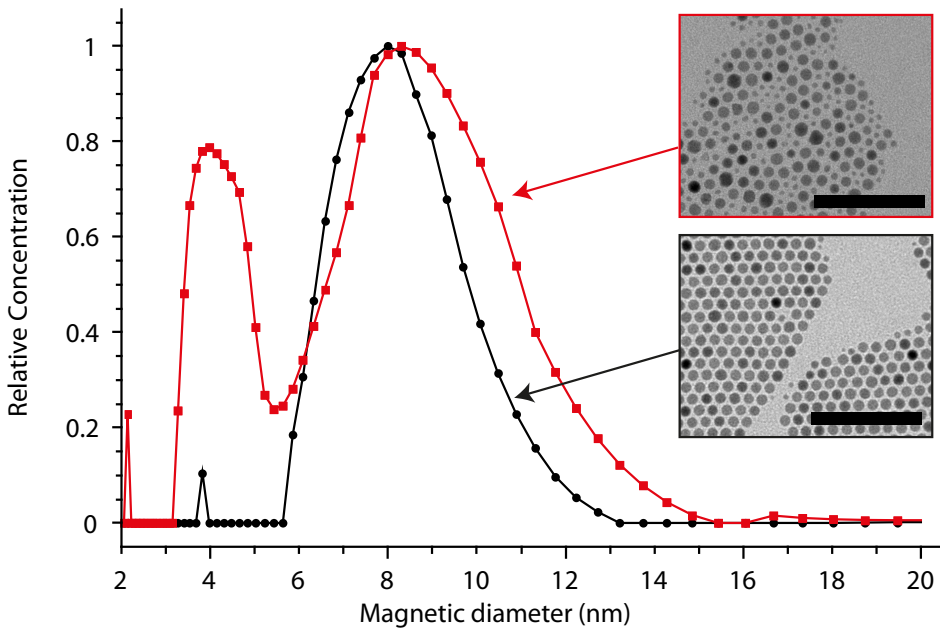


FIGURE 6.5. Magnetic size distributions reconstructed using MINORIM, from a cobalt sample before and after oxidation and washing. In the inset the TEM images of the samples are shown. The scale bar represents 100 nm.

is observed in the assemblies prepared at 45°C. However, at lower temperatures (20°C) the interactions between the nanoparticles become more important [25], which favors phase-separation; locally, where both types of particles are present, still have same  $\text{AlB}_2$ -like structure is found. Upon increasing the temperature to 70°C, the interparticle spacing is decreased due to dissolution of the ligand molecules into the ethylene glycol subphase [26]. Since for smaller particle-particle separations the Van der Waals interactions become more dominant, the system phase separates into more or less ordered hexagonal layers. A similar effect is observed when instead of ethylene glycol diethylene glycol (DEG) is used as the sub-phase. DEG is a better solvent for the capping ligands than EG, so even at lower temperatures the ligands desorb from the nanoparticle interface, therefore reducing the colloidal stability of these particles. As a consequence, when DEG is used as the sub-phase, only locally ordered structures are observed in which the particles are often sintered together.

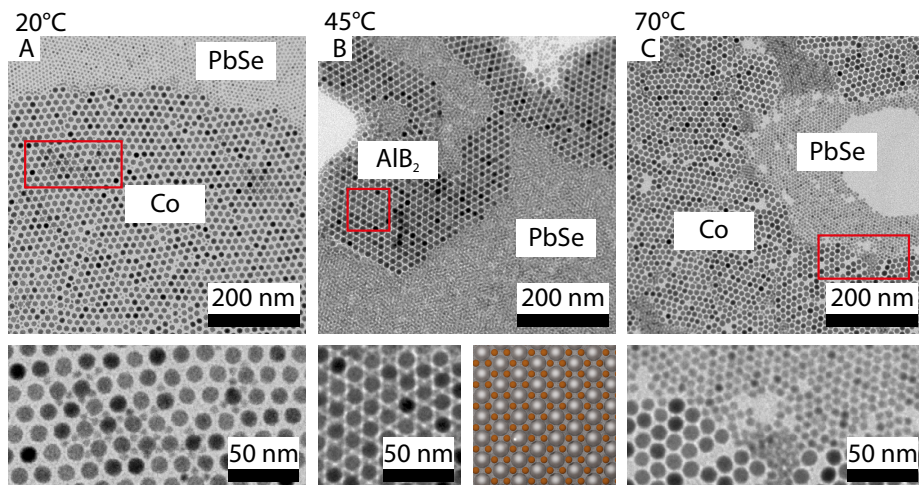


FIGURE 6.6. TEM images of self-assembled binary nanoparticle films formed by evaporating a mixture of 13 nm cobalt nanoparticles and 6.7 nm PbSe nanoparticles in toluene on an ethylene glycol/air interface at different temperatures. (A) At 20°C, the two types of nanoparticles phase separate nearly completely to form distinct close-packed PbSe and Co regions. Only locally the smaller PbSe nanoparticles penetrate to the interstitial spaces in the close-packed cobalt lattice (lower inset). (B) At 45°C, nearly all cobalt nanoparticles are located in a binary  $A1B_2$  type superlattice with the PbSe nanoparticles. Excess PbSe nanoparticles form close-packed assemblies around the binary structures. (C) At 70°C, the stabilizing ligand shells of both types of nanoparticles dissolve partly in the ethylene-glycol so that the core-core separations decrease. This leads to an increase in the particle-particle interactions and hence phase separation of the two types of nanoparticles into PbSe and Co rich regions similar to what is observed at 20°C.

It is well known that colloidal magnetic particles form two-dimensional sheets when aligned in a magnetic field [31] due to the dipole-dipole interactions between the nanoparticles. Here, we performed the self-assembly process in the presence of a 100 mT magnetic field to create magnetically aligned binary superlattices.



In fig. 6.7 the structure of these assemblies is shown for different magnifications, revealing the ordering on different length scales. In the image with the lowest magnification (fig. 6.7 A), the structures indicated by the arrows are the sheets containing the cobalt nanoparticles, which could easily be micrometers long. The width of these sheets (fig. 6.7 B, C) ranged from 100 nm to 500 nm although preferential multiples of 140 nm are found. An indication for this behavior is found in fig. 6.7 C, where three sheets that each have a width of 140 nm are aligned parallel and two of them merge in the top-left corner. It is likely that the system initially forms equally sized bands, which later merge into the broader sheets, which was previously found both experimentally [31] and theoretically [32, 33].

#### 4. Conclusions

A minimalistic synthesis method for cobalt nanoparticles was developed with which cobalt nanoparticles can be synthesized in a fast way, with polydispersities of 6% or lower. The high quality of these particles clearly requires the combination of a coordinating solvent, dichlorobenzene, and the ligands oleic acid and trioctylphosphine oxide, because omission of one of those reduces the quality of the synthesized nanoparticles. The ease of this method allows for rapid screening of the reaction conditions, which opens a route toward the determination of the essential requirements for the synthesis of monodisperse nanoparticles.

These cobalt nanoparticles were combined with PbSe quantum dots and superlattices were formed at the ethylene glycol/air interface. Depending on the reaction temperature, the obtained superlattices have an  $\text{AlB}_2$  like crystal lattice. For both low and high reaction temperatures, phase separated layers are obtained due to the strong interactions between the nanoparticles, while the largest the binary superlattices are found at intermediate reaction temperatures. When a magnetic field is applied during self-assembly, the structures have a preferential orientation, visible as micrometers long and 140 nm wide sheets of binary superlattices.

#### Bibliography

- [1] J. S. Lee, M. I. Bodnarchuk, E. V. Shevchenko, and D. V. Talapin. “Magnet-in-the-semiconductor” FePt-PbS and FePt-PbSe nanostructures: Magnetic properties, charge transport, and magnetoresistance. *J. Am. Chem. Soc.*, 132 (18):6382–6391, 2010.
-

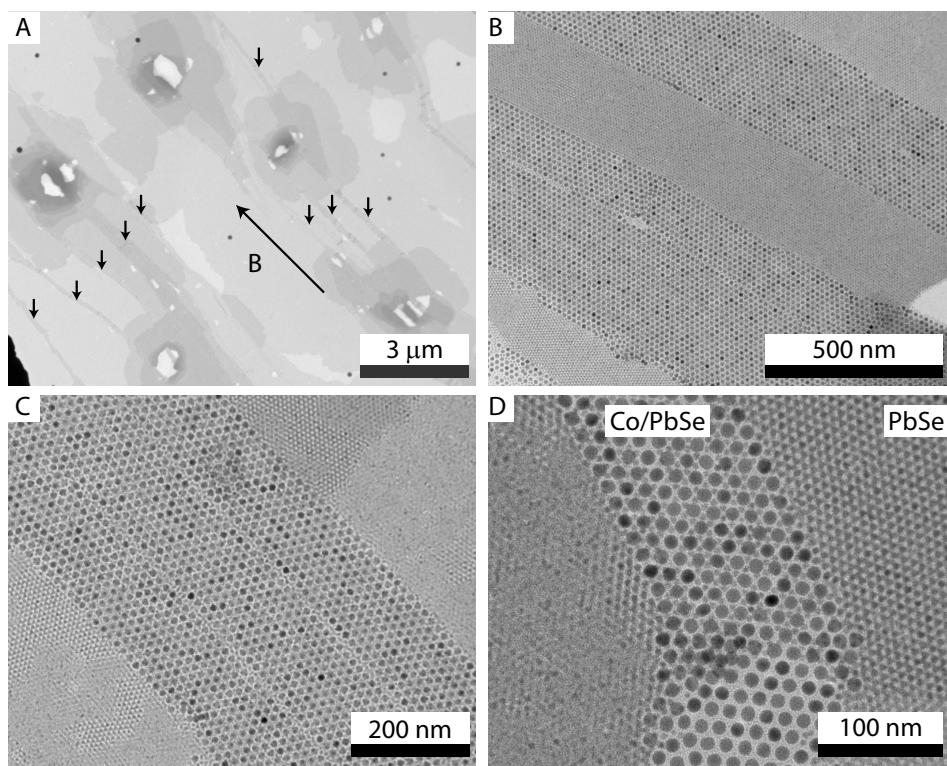


FIGURE 6.7. TEM images of a binary superlattice of PbSe (8.3 nm) and cobalt (17 nm) nanoparticles with a size ratio of 0.63 at different magnifications. In the low magnification image (A) the aligned sheets of the cobalt containing structures are marked with the short vertical arrows and the direction of the magnetic field is represented by the longer arrow. The inner structure of these sheets is  $\text{AlB}_2$  as is clear at the highest magnification (D).

- [2] E. V. Shevchenko, D. V. Talapin, N. A. Kotov, S. O'Brien, and C. B. Murray. Structural diversity in binary nanoparticle superlattices. *Nature*, 439(7072): 55–9, 2006.
- [3] E. V. Shevchenko, D. V. Talapin, C. B. Murray, and S. O'Brien. Structural characterization of self-assembled multifunctional binary nanoparticle superlattices. *J. Am. Chem. Soc.*, 128(11):3620–37, 2006.
- [4] A. Dong, J. Chen, P. M. Vora, J. M. Kikkawa, and C. B. Murray. Binary nanocrystal superlattice membranes self-assembled at the liquid-air interface.

- 
- Nature*, 466:474–477, 2010.
- [5] D. V. Talapin, E. V. Shevchenko, C. B. Murray, A. V. Titov, and P. Kral. Dipole-dipole interactions in nanoparticle superlattices. *Nano Lett.*, 7(5): 1213–9, 2007.
- [6] M. I. Bodnarchuk, M. V. Kovalenko, W. Heiss, and D. V. Talapin. Energetic and entropic contributions to self-assembly of binary nanocrystal superlattices: temperature as the structure-directing factor. *J. Am. Chem. Soc.*, 132(34):11967–77, 2010.
- [7] M. V. Kovalenko, D. V. Talapin, M. A. Loi, F. Cordella, G. Hesser, M. I. Bodnarchuk, and W. Heiss. Quasi-seeded growth of ligand-tailored PbSe nanocrystals through cation-exchange-mediated nucleation. *Angew. Chem. Int. ed.*, 47(16):3029–33, 2008.
- [8] V. F. Puentes, K. M. Krishnan, and A. P. Alivisatos. Colloidal nanocrystal shape and size control: The case of cobalt. *Science*, 2115(2001), 2001.
- [9] J. V. I. Timonen, E. T. Seppälä, O. Ikkala, and R. H. A. Ras. From hot-injection synthesis to heating-up synthesis of cobalt nanoparticles: observation of kinetically controllable nucleation. *Angew. Chem. Int. ed.*, 50(9): 2080–4, 2011.
- [10] Q. A. Pankhurst, J. Connolly, S. K. Jones, and J. Dobson. Applications of magnetic nanoparticles in biomedicine. *J. Phys. D: Appl. Phys.*, 36(13): R167–R181, 2003.
- [11] B. Gleich and J. Weizenecker. Tomographic imaging using the nonlinear response of magnetic particles. *Nature*, 435:1214, 2005.
- [12] M. E. Dry. The Fischer-Tropsch process: 1950-2000. *Catal. Today*, 71(3-4): 227–241, 2002.
- [13] V. Iablokov, S. K. Beaumont, S. Alayoglu, V. V. Pushkarev, C. Specht, J. Gao, A. P. Alivisatos, N. Kruse, and G. A. Somorjai. Size-controlled model Co nanoparticle catalysts for CO<sub>2</sub> hydrogenation: synthesis, characterization, and catalytic reactions. *Nano Lett.*, 12(6):3091–3096, 2012.
- [14] G. Cheng, D. Romero, G. T. Fraser, and A. R. Hight Walker. Magnetic-field-induced assemblies of cobalt nanoparticles. *Langmuir*, 21(26):12055–9, 2005.
- [15] J. Ku, D. M. Aruguete, A. P. Alivisatos, and P. L. Geissler. Self-assembly of magnetic nanoparticles in evaporating solution. *J. Am. Chem. Soc.*, 133(4): 838–48, 2011.
-

- [16] C. Salzemann, J. Richardi, I. Lisiecki, J. J. Weis, and M. P. Pileni. Mesoscopic void structures in cobalt nanocrystal films formed from drying concentrated colloidal solutions. *Phys. Rev. Lett.*, 144502:1–4, 2009.
  - [17] G. Held, G. Grinstein, H. Doyle, S. Sun, and C. Murray. Competing interactions in dispersions of superparamagnetic nanoparticles. *Phys. Rev. B*, 64(1):012408, 2001.
  - [18] P. Y. Keng, I. Shim, B. D. Korth, J. F. Douglas, and J. Pyun. Synthesis and self-assembly of polymer-coated ferromagnetic nanoparticles. *ACS nano*, 1(4):279–292, 2007.
  - [19] P. Y. Keng, B. Y. Kim, I. B. Shim, and R. Sahoo. Colloidal polymerization of polymer-coated ferromagnetic nanoparticles into cobalt oxide nanowires. *ACS Nano*, 3(10):3143–3157, 2009.
  - [20] P. Poizot, S. Laruelle, S. Grugeon, L. Dupont, and J. M. Tarascon. Nano-sized transition-metal oxides as negative-electrode materials for lithium-ion batteries. *Nature*, 407(6803):496–9, 2000.
  - [21] W. Y. Li, L. N. Xu, and J. Chen.  $\text{Co}_3\text{O}_4$  nanomaterials in lithium-ion batteries and gas sensors. *Adv. Funct. Mater.*, 15(5):851–857, 2005.
  - [22] M. T. Trinh, A. J. Houtepen, J. M. Schins, T. Hanrath, J. Piris, W. Knulst, A. P. L. M. Goossens, and L. D. A. Siebbeles. In spite of recent doubts carrier multiplication does occur in PbSe nanocrystals. *Nano Lett.*, 8(6):1713–1718, 2008.
  - [23] D. V. Talapin and C. B. Murray. PbSe nanocrystal solids for n- and p-channel thin film field-effect transistors. *Science*, 310(5745):86–9, 2005.
  - [24] T. Rauch, M. Böberl, S. F. Tedde, J. Fürst, M. V. Kovalenko, G. Hesser, U. Lemer, W. Heiss, and O. Hayden. Near-infrared imaging with quantum-dot-sensitized organic photodiodes. *Nat. Photonics*, 3(6):332–336, 2009.
  - [25] W. H. Evers, B. De Nijs, L. Filion, S. Castillo, M. Dijkstra, and D. Vanmaekelbergh. Entropy-driven formation of binary semiconductor-nanocrystal superlattices. *Nano Lett.*, 10(10):4235–4241, 2010.
  - [26] W. H. Evers, B. Goris, S. Bals, M. Casavola, J. de Graaf, R. van Roij, M. Dijkstra, and D. Vanmaekelbergh. Low-dimensional semiconductor superlattices formed by geometric control over nanocrystal attachment. *Nano Letters*, 13(6):2317–2323, 2012.
  - [27] V. K. LaMer and R. H. Dinegar. Theory, production and mechanism of formation of monodispersed hydrosols. *J. Am. Chem. Soc.*, 72(8), 1950.
-

- [28] J. Park, J. Joo, S. G. Kwon, Y. Jang, and T. Hyeon. Synthesis of monodisperse spherical nanocrystals. *Angew. Chem. Int. Ed.*, 46(25):4630–60, 2007.
  - [29] S. G. Kwon and T. Hyeon. Formation mechanisms of uniform nanocrystals via hot-injection and heat-up methods. *Small*, 7(19):2685–2702, 2011.
  - [30] Y. A. Yang, H. Wu, K. R. Williams, and Y. C. Cao. Synthesis of CdSe and CdTe nanocrystals without precursor injection. *Angew. Chem. Int. Ed.*, 44(41):6712–5, 2005.
  - [31] M. Klokkenburg, B. H. Ern e, J. D. Meeldijk, A. Wiedenmann, A. Petukhov, R. P. A. Dullens, and A. P. Philipse. In situ imaging of field-induced hexagonal columns in magnetite ferrofluids. *Phys. Rev. Lett.*, 97(18):185702, 2006.
  - [32] A. Satoh, R. W. Chantrell, K. Shin-Ichi, and G. N. Coverdale. Two-dimensional monte carlo simulations to capture thick chainlike clusters of ferromagnetic particles in colloidal dispersions. *J. Colloid Interface Sci.*, 178(2):620–627, 1996.
  - [33] J. J. Weis. Low density quasi-two-dimensional dipolar hard spheres in an external field. *Mol. Phys.*, 103(1):7–10, 2005.
-



## **In Situ Infrared Spectroscopy of Ligand Adsorption on Colloidal Nanoparticles**

### ABSTRACT

The binding of ligands on a nanoparticle surface is studied using infrared spectroscopy for two different cases.

First, the optical properties of CdTe quantum dots are correlated with the change in capping density when a colloidal dispersion of the nanoparticles is diluted. The luminescence intensity of CdTe quantum dots capped with dodecylamine shows luminescence brightening when stored in the dark, whereas no such brightening is observed for octadecylamine-capped quantum dots. Infrared spectra show that upon dilution of the sample, the capping density for dodecylamine-capped samples decreases with time. Our explanation is that the decrease in capping density of the dodecylamine-capped sample upon dilution creates space for the ligand layer to reorganize, which reduces the strain on the quantum dot surface. The surface can then relax, thereby decreasing the number of defects and as a consequence increasing the luminescence quantum yield.

In the second part of this chapter, the adsorption isotherm of oleic acid ligands on PbSe is measured in comparison to magnetite nanoparticles. The oleic acid binds more weakly to PbSe quantum dots than to magnetite nanoparticles, but the maximum adsorption density is the same for both systems. The maximum ligand adsorption seems to be limited by the size of the ligands rather than by the number of binding sites on the nanoparticle surface.

## 1. Introduction

To create a stable nanoparticle dispersion in an apolar solvent, the nanoparticles are often coated with a layer of hydrocarbon molecules [1]. This layer plays an important role in different aspects of the nanoparticle properties, both during the synthesis [2] of the particle as well in their colloidal [3], magnetic [4], and optical [1] properties. For example, during the growth of the nanoparticle, the presence of ligands can influence the size [5] as well as the shape of the nanoparticles due to their affinity for certain facets [2].

The optical properties of quantum dots are strongly influenced by passivation of the surface. Surface ions that are not fully coordinated by other ions assist non-radiative recombination of the exciton [1]. The binding of ligands to these ions blocks these non-radiative recombination pathways and therefore increases the photoluminescence quantum yield.

As ligands are an important factor that influences the properties of quantum dots, different purposes require different ligands. For example, during the growth of the nanoparticles, the ligand-quantum dot complex should be reversible to allow further growth, but after synthesis, more strongly binding ligands are preferred as they promote the long-term stability. Several ligand exchange methods [6–8] have been developed to tailor the quantum dot properties to fit the requirements. The success of these protocols indicates the dynamic nature of the ligand-quantum dot complexes; however, quantitative information about the binding strengths of the ligands is scarce. The binding strength is coupled to the average residence times of the ligands at the surface; for example, the weakly binding amine ligands have an average exchange rate of  $0.05 \text{ ms}^{-1}$ , whereas the much more strongly binding ligand oleic acid has a residence time on the order of seconds [9].

Infrared spectroscopy is often used as a qualitative tool [10–12], for example to study which complexes are formed by adsorbing molecules [13]. However, quantitative information can be obtained as well. For example, infrared spectroscopy has been utilized to measure the adsorption isotherm of oleic acid on magnetite [14] and the phase diagram of a phase separating colloid-polymer mixture [15, 16].

In this chapter two cases of ligand adsorption are investigated using infrared absorption measurements. First we examine the effect of the ligands on the luminescence-brightening of CdTe quantum dots capped with dodecylamine or octadecylamine, ligands with a similar head group but different chain lengths. The change in luminescence is correlated with the adsorption-desorption equilibrium of the ligands at the quantum dot surface. In the second part of this chapter,

---



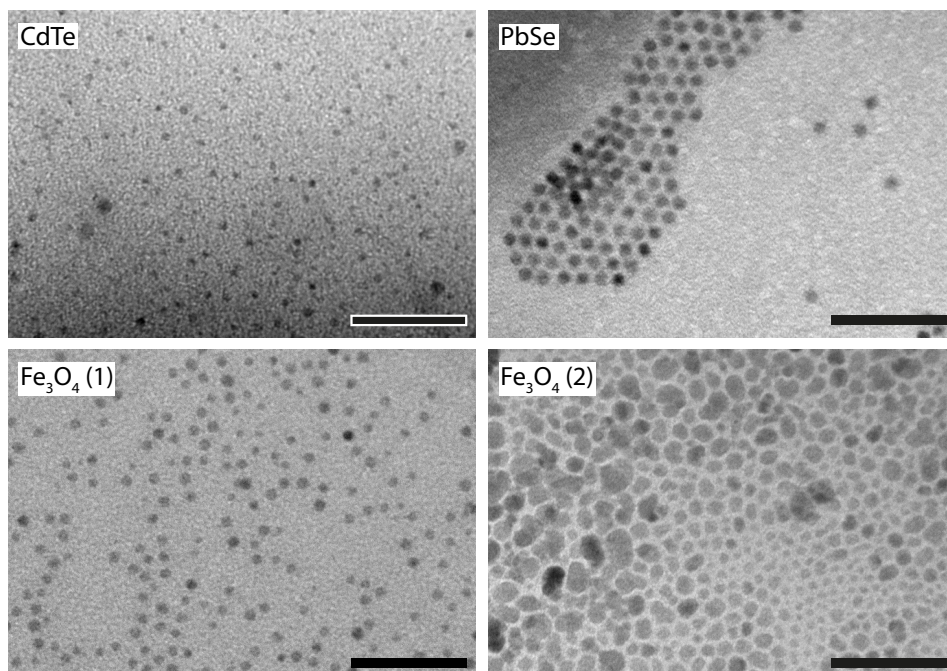


FIGURE 7.1. TEM images of the nanoparticles used in this chapter. (A) CdTe, (B) PbSe, and magnetite synthesized using a high-temperature decomposition (C) or an aqueous coprecipitation (D) method. The scale bar is 50 nm in all images.

the adsorption isotherm of oleic acid molecules on PbSe is measured using in situ spectroscopy and compared to that of magnetite nanoparticles. From these measurements, the capping density and the adsorption free energy are obtained.

## 2. Methods

### 2.1. Nanoparticle Synthesis.

*CdTe.* The CdTe quantum dots were prepared in a nitrogen glovebox using the procedure reported in ref. [17]. In a three-neck flask, 10 g of dodecylamine (Aldrich 98%, DDA) and 7 mL tri-octylphosphine (Aldrich 90%, TOP) was heated to 50°C. A mixture of 0.22 g dimethylcadmium (ARC technologies 99.9%), 7 mL of TOP, and 0.16 g tellurium (Heraeus 99.999%) were added to this solution and heated to 145°C under vigorous stirring. This reaction mixture was kept at this temperature for 2 hours and 10 minutes, after which it was heated to 165°C for 3

hours and 40 minutes. This procedure resulted in particles of 2.9 nm (see fig. 7.1 A). Unreacted tellurium powder was removed from the reaction mixture by 15 minutes of centrifugation at 3000 rpm, and the supernatant was collected. This crude sample was washed by adding an equal amount of toluene and subsequent addition of methanol till the nanoparticles precipitate. This mixture was centrifuged at 3000 rpm for 15 minutes, and the sediment was redispersed in toluene.

Stock solutions of these quantum dots with different capping ligands were prepared. For DDA-capped CdTe quantum dots, 204.6  $\mu\text{L}$  DDA was added to 197  $\mu\text{L}$  of a 4.8  $\mu\text{mol/L}$  quantum dot dispersion and stirred for 14 hours at 55°C. Similarly, for the quantum dots capped with octadecylamine (Fluka >90%, ODA), 0.257 g was heated to 50°C and mixed with 181  $\mu\text{L}$  of the same 4.8  $\mu\text{mol/L}$  QD dispersion and stirred for 14 hours at 55°C. Both stock dispersions contained a ligand concentration of 2 mol/L.

*PbSe.* Standard airless techniques (Schlenk line and nitrogen glove box) were used in the synthesis of PbSe NCs. The synthesis is based on the method of Kovalenko et al. [18] 0.95 g lead chloride (99.999%, Sigma-Aldrich) and 17.5 mL oleylamine (90 %, Aldrich) were combined and the mixture was heated to 140°C. At this temperature a mixture of 1.2 g selenium (99.99%, Strem Chemicals) in 10 mL trioctylphosphine (90%, Sigma Aldrich) and 0.5-4.5 mL  $\text{Sn}[\text{N}(\text{SiMe}_3)_2]_2$  (Sigma-Aldrich) was fast injected. The mixture was reheated to 120°C and afterwards it was allowed to cool to room temperature in 30 minutes. Oleic acid (90%, Sigma-Aldrich, 15 mL) was slowly added, followed by the addition of 40 mL methanol (Sigma-Aldrich, anhydrous, 99.8%) to precipitate the particles. After centrifugation (2500 *g*, 5 minutes), the supernatant was removed and the quantum dots with a diameter of 5.1 nm and a standard deviation of 0.7 nm (see fig. 7.1 B) were dispersed in cyclohexane.

*Magnetite.* Two different magnetite systems are used for these experiments, one system containing nanoparticles prepared via a high temperature decomposition method described as the “sphere” method in ref. [19]. This resulted in spherical particles with a diameter of 4.6 nm and a standard deviation of 0.5 nm (see fig. 7.1 C). The second system was made by coprecipitation in aqueous environment [20] resulting in polydisperse particles with an average diameter of 6.5 nm and a standard deviation of 2 nm (see fig. 7.1 D). In both cases, the particles were capped with oleic acid and dispersed in cyclohexane.

**2.2. Dynamic Light Scattering.** Dynamic light scattering (DLS) measurements were performed using a Malvern zetasizer nano. The samples were prepared

---

by diluting the stock dispersion by a factor of 100 and filtered with a hydrophobic filter with a pore size of 0.2  $\mu\text{m}$  to remove dust particles from the dispersion. Both the forward scattering, at an angle of  $12.8^\circ$ , and backward scattering, at an angle of  $173^\circ$ , were recorded for 29 measurements of about half an hour each, so that in total the particle size was monitored for 18 hours at room temperature. Due to the combination of low scattering cross section and low concentration, the contrast of the correlation function was typically so small (0.2) that the data was analyzed assuming heterodyne scattering rather than homodyne scattering. This implied that the size distributions determined by the program, which assumed homodyne scattering, were overestimated by a factor of two; the average particle sizes indicated by the program were divided by two before interpretation [21].

**2.3. Photoluminescence Spectroscopy.** The photoluminescence time series were collected from dispersions, prepared by diluting the stock dispersions by a factor of 100. The sample was placed in a nitrogen glovebox in a closed compartment to eliminate the influence of external light sources. The light from the excitation source, a 400 nm 10 W LED, was guided via an optical fiber to the sample and the emitted light, collected under an angle of  $90^\circ$  to the excitation beam, was guided via another optical fiber to a liquid nitrogen cooled Princeton Instrument CCD detector with an 0.3 m Acton Research monochromator. Both, the LED and the CCD camera were placed outside the glovebox. The time series were recorded for 25 hours by acquiring the spectra at 5 min time intervals with illumination times of 1 s for each spectrum. Control samples were prepared similarly but stored in the dark, and the spectrum was measured only once after approximately the same period as used for the acquisition of the time series.

**2.4. Infrared Adsorption Spectroscopy.** All infrared absorption measurements were performed using a Perkin Elmer Frontier FTIR spectrophotometer. In situ measurements were done using a liquid cell with KBr windows and an internal path length of 100  $\mu\text{m}$ , and ex situ experiments were performed with KBr pellets.

*Preparation of the KBr pellets.* KBr pellets were prepared by weighing 250 mg dry KBr in a glass vial inside a nitrogen flushed glove box. A drop of 50  $\mu\text{L}$  of the dispersion was added and mixed with the powder till all solvent, cyclohexane, was evaporated. The dry powder was then pressed into the pellets with a Specac pellet-press at a pressure of 10 bar, and the pellets were transferred as quickly as possible to the nitrogen flushed sample chamber of the IR spectrophotometer.

---

*Measurement of the adsorption isotherms.* The adsorption density of oleic acid ligands on the surface of the nanoparticles was measured using in situ IR spectroscopy. The adsorption isotherms were obtained by measuring a series of IR spectra of samples with a known concentration of nanoparticles and varying oleic acid concentration. The total oleic acid concentration was determined from the -CH= vibration at  $3006\text{ cm}^{-1}$  and the concentration of free oleic acid ligands was obtained from the -C=O vibration at  $1713\text{ cm}^{-1}$  (see section 3.2 for details). The extinction coefficient  $\epsilon$  for these peaks was determined from the IR spectra of a series of oleic acid solutions in cyclohexane. The cyclohexane spectrum was recorded as well and subtracted from the sample and calibration spectra before the peaks were analyzed. The peak at  $3006\text{ cm}^{-1}$  is always on top of the -CH vibrations so a baseline was defined as the common tangent connecting both sides of the peak and the peak height was defined with respect to that baseline.

### 3. Results

**3.1. CdTe Photo-Luminescence Brightening.** An increase in the photoluminescence intensity upon continued illumination (photo-brightening) is a well known phenomenon in many QD systems, such as CdTe [22], CdSe [23], PbS [24], and InAs [25]. For the CdTe QDs the photoluminescence intensity is shown in fig. 7.2 as function of time for quantum dots with a diameter of 2.9 nm and capped with dodecylamine or octadecylamine. The stars in fig. 7.2 show the photoluminescence of dispersions of quantum dots capped with ODA or DDA, prepared similarly to the illuminated samples but stored in the dark. Both samples show an increase in the photoluminescence intensity when followed in time, which is discussed in more detail in ref. [26], but it is their behavior in the dark which is of interest here. For the DDA-capped quantum dots, the photoluminescence of the sample stored in the dark is larger than the initial luminescence directly after dilution, whereas for the ODA-capped quantum dots, no increase in the luminescence intensity is observed when stored in the dark. To quantify the time scales of the changes in the luminescence spectra, the time dependence of the luminescence intensity is fitted using exponential functions. As there are two processes present in the case of the illuminated time traces, the process that happens in the dark and the ‘normal’ photo-brightening, a double exponential fit is used:

$$(7.1) \quad I = I_{\infty} - A_1 \exp[-t/\tau_1] - A_2 \exp[-t/\tau_2]$$

---

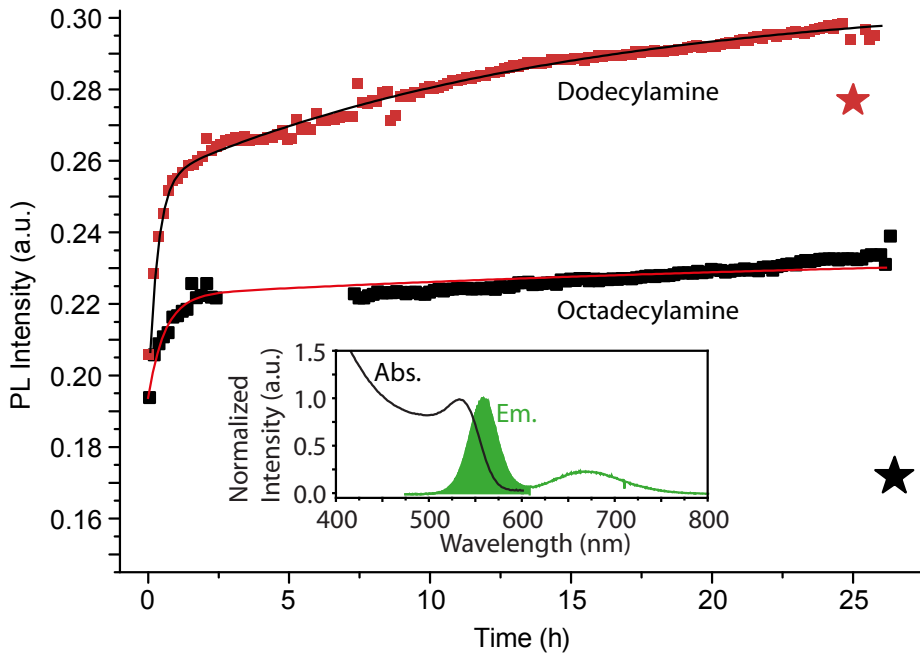


FIGURE 7.2. Integrated photoluminescence intensity of CdTe quantum dots capped with octadecylamine (black) or dodecylamine (red) ligands plotted as function of time. The stars denote similar samples but stored in the dark and only measured once. The inset shows typical absorption (Abs.) and emission (Em.) spectra of the quantum dots normalized to the intensity of the excitonic peak. The shaded area indicates the excitonic luminescence band, whereas the luminescence band at higher wavelength originates from defects.

Here,  $I_{\infty}$  is the equilibrium luminescence intensity, and  $A_1$  and  $A_2$  are the amplitudes of the two contributions with a characteristic time scale  $\tau_1$  and  $\tau_2$ . The two decay times obtained from the fit are 19 min and 860 min for DDA-capped quantum dots, and 36 min and 1859 min for the ODA-capped quantum dots.

In the literature, several mechanisms are proposed to explain this photoluminescence brightening, such as surface passivation by water or methanol [27], passivation by oxygen [28], or surface reconstruction and relaxation [22, 25]. As our experiments are performed in a nitrogen atmosphere ( $< 5$  ppm  $O_2$  and  $H_2O$ ),

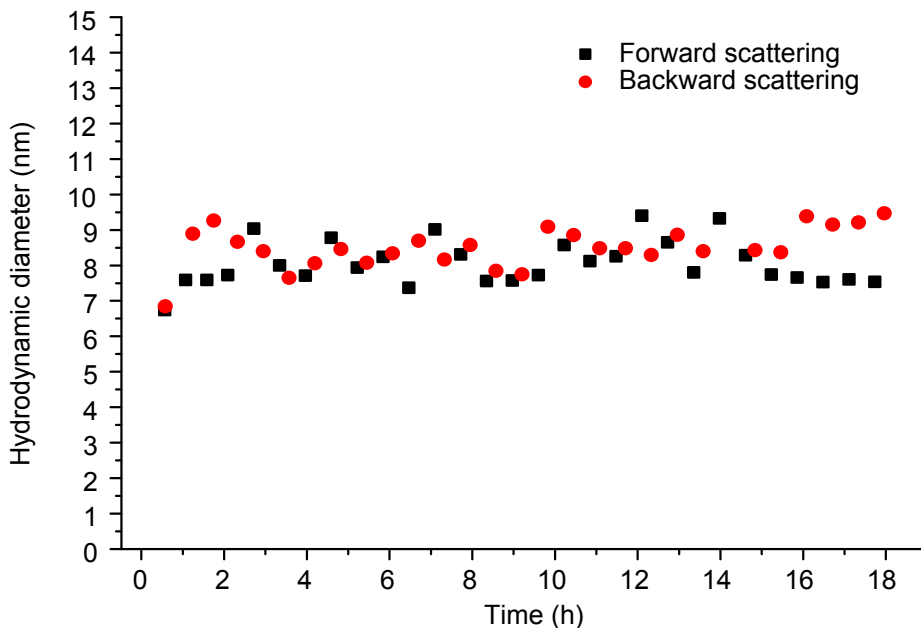


FIGURE 7.3. Hydrodynamic diameter of the 2.9 nm CdTe quantum dots dispersed in toluene at 25°C measured as function of time after dilution.

the influence of oxygen or water can be excluded as cause of the photo-brightening; in fact, exposure of these samples to air reduces the luminescence intensity.

A possible origin of the observed brightening of the DDA-capped quantum dots would be the presence of equilibrium clusters in the stock solutions in which the luminescence is quenched due to energy transfer from luminescent to non-luminescent quantum dots. Because the energy transfer is very sensitive to the distance between the quantum dots, breaking up of the cluster, which increases the distance between the quantum dots, would reduce this energy transfer and thereby increases the photoluminescence intensity. Here, this hypothesis is tested by measuring the average hydrodynamic size with dynamic light scattering as function of time as shown in fig. 7.3. The hydrodynamic diameter of the particles is  $8.3 \pm 0.5$  nm, in good agreement with single quantum dots ( $d = 2.9$  nm) capped with a capping layer of approximately 1.6 nm. The hydrodynamic diameter is

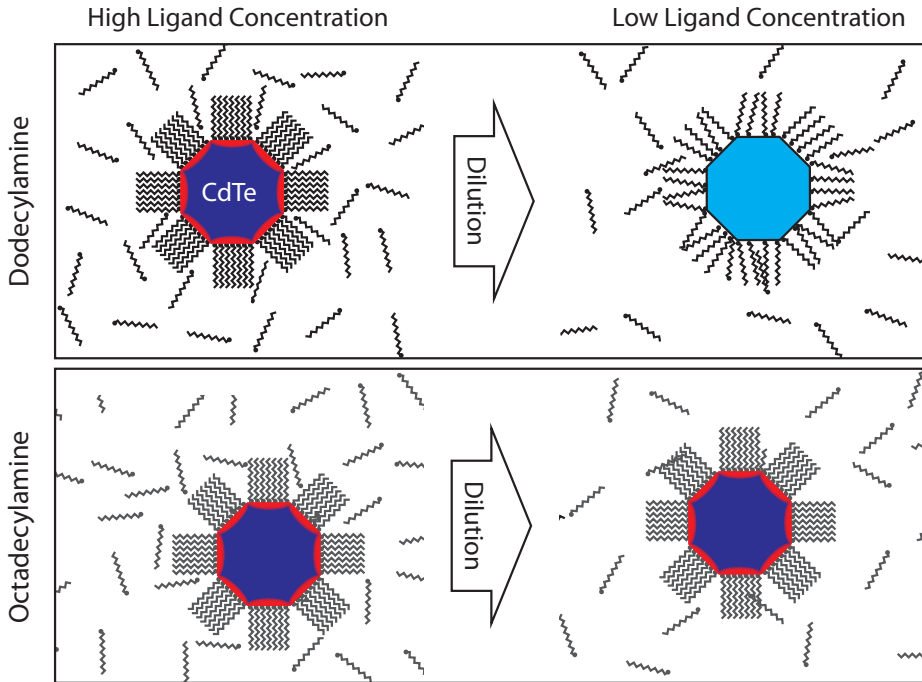


FIGURE 7.4. Schematic picture of the state of the quantum dots at high concentration of ligands (left) and at low ligand concentration (right). For DDA-capped quantum dots, the strain on the surface is reduced after dilution, whereas for ODA it still remains and therefore the quantum yield does not increase.

independent of time, and this excludes that the observed luminescence brightening is due to the breaking up of clusters of quantum dots.

It is well known that the ligands have a strong influence on the luminescent properties of quantum dots [1]. For example, cooling the quantum dot dispersion below a specific temperature quenches the luminescence intensity, likely due to surface defects created by the crystallization of the ligands on the interface [8, 17]. This effect is totally reversible, as on increasing the temperature, the photoluminescence intensity is fully recovered. A similar mechanism can be responsible for the observed photoluminescence-brightening in the present case. In the case of an equilibrium between ligand molecules on the quantum dot surface and free

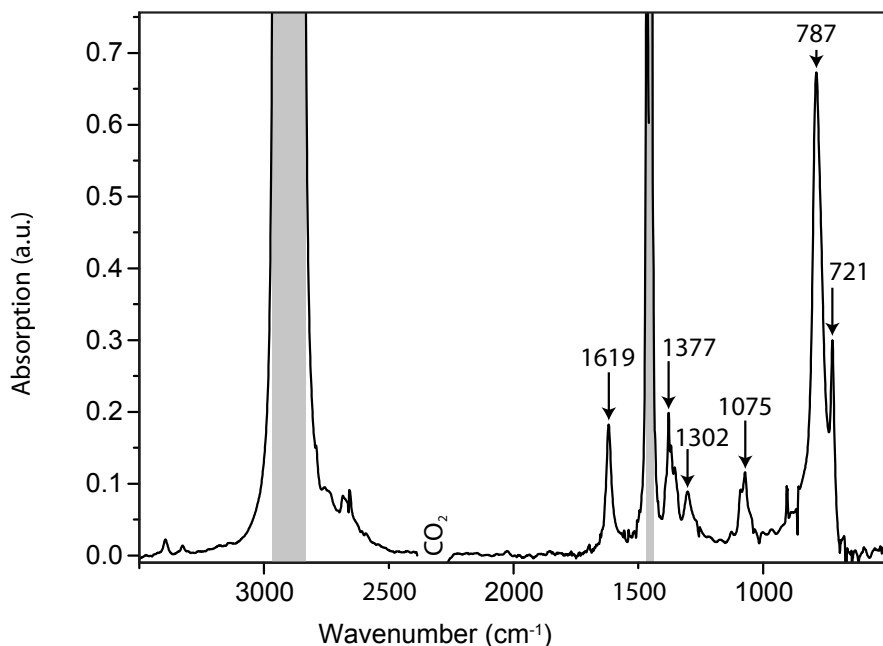


FIGURE 7.5. In situ infrared absorption spectrum of DDA-capped CdTe quantum dots dispersed in cyclohexane, corrected for the adsorption of the cyclohexane. The gray areas denote the regions where the signal is saturated by the solvent. Around  $2350\text{ cm}^{-1}$  the signal was erratic due to  $\text{CO}_2$  vibrations.

ligand molecules dissolved in the bulk liquid, the adsorption density of the capping molecules is related to the free ligand concentration. For high ligand concentrations, as is the case in the stock solutions, the adsorption density is high. Theoretical modeling has shown that, in the case of CdSe, small displacements of the surface atoms are required to prevent electronic surface states with energies in the bandgap that quench the luminescence [29]. If the capping density is too high, the capping ligands will form close packed layers and therefore the position of the ligands on the surface is not only determined by the position of the surface atoms but also by the other ligand molecules. This hampers the relaxation of the quantum dot surface and as a consequence, the surface states are not completely removed. Upon dilution, the adsorption density decreases, and the surface stress



TABLE 7.1. Assignments of the IR-peaks in fig. 7.5

Peak position ( $\text{cm}^{-1}$ )	Vibration	Refs.
2900	-CH	saturated
1619	-NH scissoring	[10]
1450	-CH	saturated
1377	-CH	[30]
1302	-CH	[30]
1075	-NH	
787	-NH	[10]
721	CH rocking	[10]

is reduced, such that it can relax and defects are eliminated, resulting in a higher quantum yield (fig. 7.4 top).

It is known that self-assembled monolayers of these molecules have a phase transition from a locked rotator phase, where all ligands have a fixed angle with the interface, to an unlocked rotator phase where the angle between the ligand and surface is uncorrelated between neighboring ligands [8]. For dodecylamine, this phase transition is below room temperature, indicating that at room temperature the monolayer is liquid-like, while for octadecylamine, this transition temperature is above room temperature and the ligand layer resembles more a crystalline structure. For the ODA monolayer, dilution of the system would in principle lower the adsorption density; however, diffusion from a ligand out of a close-packed layer is a slow process [7], so it takes a long time before the system is equilibrated. In contrast, the DDA-capped particles, which have a more liquid-like capping layer, can respond to dilution of the sample much faster, as is demonstrated by the observed photo-brightening when the sample is stored in the dark.

The dynamics of the DDA capping layer was tested here by taking in situ infrared spectra as function of time. In fig. 7.5, a typical absorption spectrum is shown for DDA-capped CdTe quantum dots dispersed in cyclohexane. The contribution of the solvent is subtracted from the spectrum, leaving only the DDA peaks of which the corresponding vibrations are listed in table 7.1. The signal from the CH stretch vibrations at  $2900 \text{ cm}^{-1}$  and  $1450 \text{ cm}^{-1}$  is saturated due to the absorption of the solvent. At  $1619 \text{ cm}^{-1}$  a peak is visible which is related

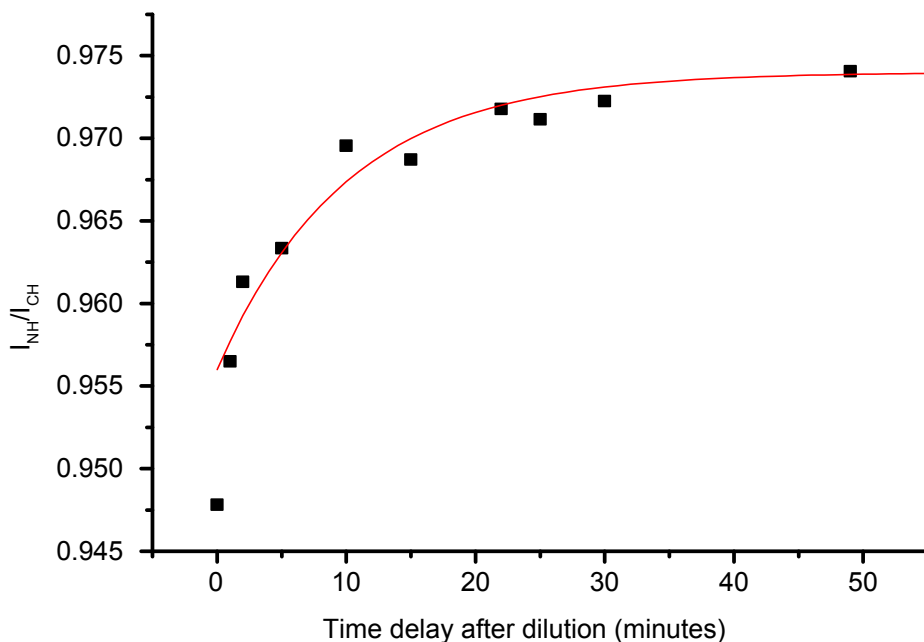


FIGURE 7.6. The peak height ratio of the NH peak at  $1619\text{ cm}^{-1}$  and the CH peak at  $721\text{ cm}^{-1}$  as function of time. The line is an exponential fit (see text for details).

to the NH stretch vibrations. Cooper et al. [10] observed multiple peaks in this region, which they attributed to the vibrations of the amine molecules adsorbed at the quantum dot surface. However, these signals are not observed in this study due to the low concentration of the quantum dots in the sample. The other peaks related to the NH group are located at  $1075\text{ cm}^{-1}$  and  $787\text{ cm}^{-1}$ . The small peak at  $721\text{ cm}^{-1}$  is the rocking vibration of the ligand tail.

To quantify the changes in the capping layer as function of time, we used the ratio between the NH vibration and the CH rocking vibration. As the rocking vibration ( $721\text{ cm}^{-1}$ ) comes from the tail of the ligands and is not influenced by the adsorption on the quantum dot surface, this is a good measure for the total ligand concentration in the sample, and therefore it is used as an internal standard. The absorption peak at  $1619\text{ cm}^{-1}$  comes from the NH head-group, which is involved in the bond between the ligand and the quantum dot. The position of this band shifts for the bound ligands [10] and therefore, this peak can be used as a measure

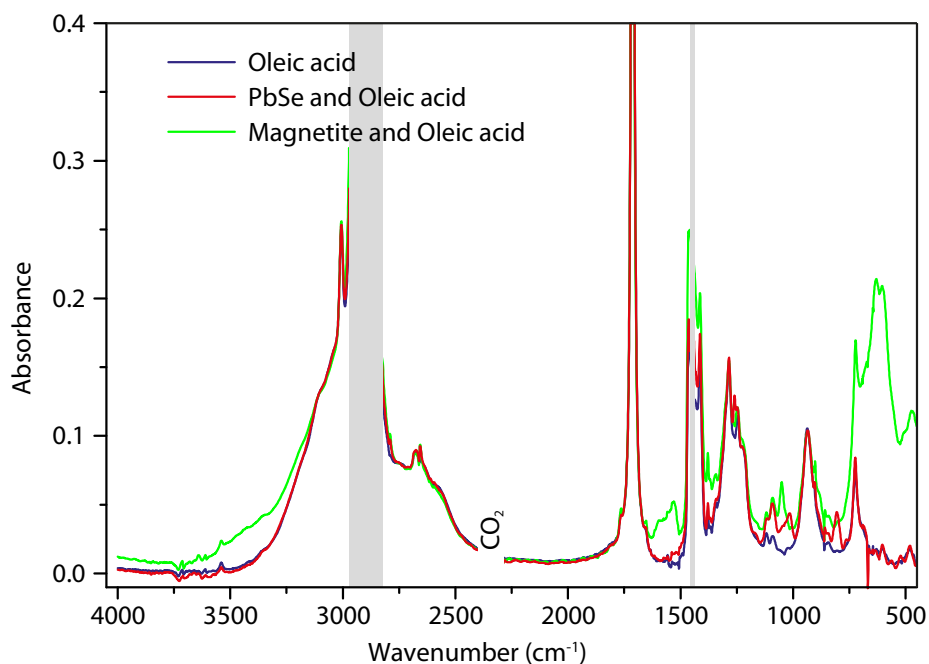


FIGURE 7.7. In situ FTIR spectra of 100 mM oleic acid in cyclohexane (red) to which oleic acid capped nanoparticles of magnetite (green) or PbSe (blue) are added. No information is obtained in the gray areas, where cyclohexane saturates the signal. The spectra are scaled to the peak at  $3006\text{ cm}^{-1}$ .

for the free ligands in solution. This ratio is shown in fig. 7.6 as function of time, and the red line is a fit with  $I_{NH}/I_{CH} = 1 - A \exp[-t/\tau]$  which gives a typical equilibration time  $\tau$  of 13 minutes. This equilibration time obtained is close to the fast equilibration time (19 min) of the luminescence intensity increase, suggesting that they originate from the same underlying process: reduction of the capping density upon dilution of the interface and subsequent surface relaxation. Similar vibration spectroscopy experiments should be carried out for ODA-capped quantum dots as well to confirm that the equilibration process is slower in that case as indicated by the longer equilibration time.

**3.2. Adsorption Isotherms of Oleic Acid on PbSe and Magnetite Nanoparticles.** In fig. 7.7, typical FTIR spectra are shown for oleic acid dissolved in cyclohexane, with and without the presence of PbSe or magnetite nanoparticles.

TABLE 7.2. Assignments of the IR-peaks in fig. 7.7

Peak position ( $\text{cm}^{-1}$ )	Vibration	Refs.
3440 <sup>m</sup>	-OH (EtOH)	
3006	$\nu$ -CH=	[11, 31, 32]
2900	-CH	saturated
2670	$\nu$ OH	[11]
1713	$\nu$ -C=O	[11, 31]
1655	$\nu$ C=C	[11, 33]
1528 <sup>m</sup>	$\nu_a$ COO-metal	[11, 31, 33]
1450	-CH	saturated
1432	$\nu_s$ COO-metal	
1413	in plane bending COH	[31, 34]
1284	$\nu$ C-O	[34]
1116 <sup>P</sup>	unknown	
1087	$\nu$ C-C	[35]
1050 <sup>m</sup>	C-O (EtOH)	
1012 <sup>P</sup>	unknown	
936	$\delta$ OH	[35]
722	CH=CH	[35]
630 <sup>m</sup>	Fe-O	[35, 36]

<sup>m</sup> Only in the magnetite spectrum

<sup>P</sup> Only in the PbSe spectrum

In table 7.2 the main peak assignments are listed. The spectra are normalized to the total oleic acid concentration determined from the peak at  $3006 \text{ cm}^{-1}$ . Although the magnetite particles used were synthesized using different methods, no qualitative difference is observed in the IR spectra of these nanoparticles.

In the region from  $4000 \text{ cm}^{-1}$  to  $2500 \text{ cm}^{-1}$  the spectra are almost indistinguishable, except for the small broad band around  $3300 \text{ cm}^{-1}$  in the case of the magnetite sample. This, in combination with the presence of the characteristic peak at  $1050 \text{ cm}^{-1}$ , which is also only visible in the magnetite spectrum, supports the assignment of these peaks to the presence of ethanol in the sample remaining from the washing procedure. The absorption saturates in the region where the hydrocarbon stretching vibrations of the solvent are present; however, on the sides

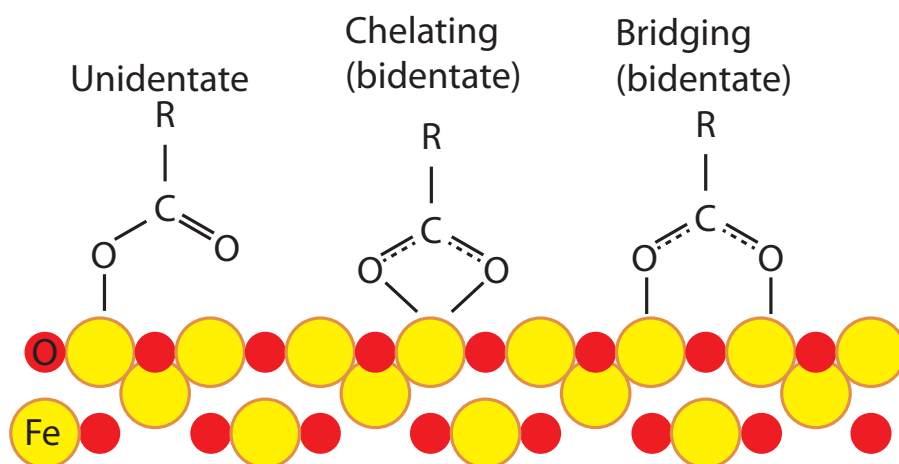


FIGURE 7.8. Possible ligand-iron complexes for the binding of oleic acid on magnetite surfaces [13].

of this band a few peaks can be distinguished. At  $3006\text{ cm}^{-1}$  a peak is visible corresponding to the asymmetric stretching of the  $-\text{CH}$  groups next to a double bond [11], whereas the symmetric stretching mode of the carboxylic-acid  $\text{OH}$  group is visible as a shoulder at  $2670\text{ cm}^{-1}$ .

For lower wavenumbers more differences are visible between the spectra. Between the clear  $-\text{C}=\text{O}$  stretch vibration at  $1713\text{ cm}^{-1}$  and the  $-\text{CH}$  vibrations at  $1450\text{ cm}^{-1}$ , a clear peak is present in the magnetite spectrum at  $1530\text{ cm}^{-1}$ . According to Lee and Condrate [11] these peaks correspond to the asymmetric stretching vibrations of the  $-\text{COO}^-$  group in the iron-oleate species present at the surface of the nanoparticles. From the splitting between the symmetric ( $1432\text{ cm}^{-1}$ , barely visible) and asymmetric stretching vibrations of the  $-\text{COO}^-$  ions, the type of the nanoparticle-ligand complex can be determined [13], see fig. 7.8. For the samples containing magnetite, the splitting  $\Delta$  is  $98\text{ cm}^{-1}$ , which points to a chelating configuration. The asymmetric stretching mode has a shoulder at  $1596\text{ cm}^{-1}$  which points to the presence of several distinguishable binding sites, and the position with a  $\Delta$  of  $160\text{ cm}^{-1}$  indicates the presence of a bridging complex.

In contrast to the clear peaks observed in the magnetite spectrum, no clear peaks corresponding to the  $-\text{COO}^-$  stretch vibrations are visible in the IR spectrum of the lead-selenide nanoparticles, except for a weak shoulder at  $1540\text{ cm}^{-1}$ .

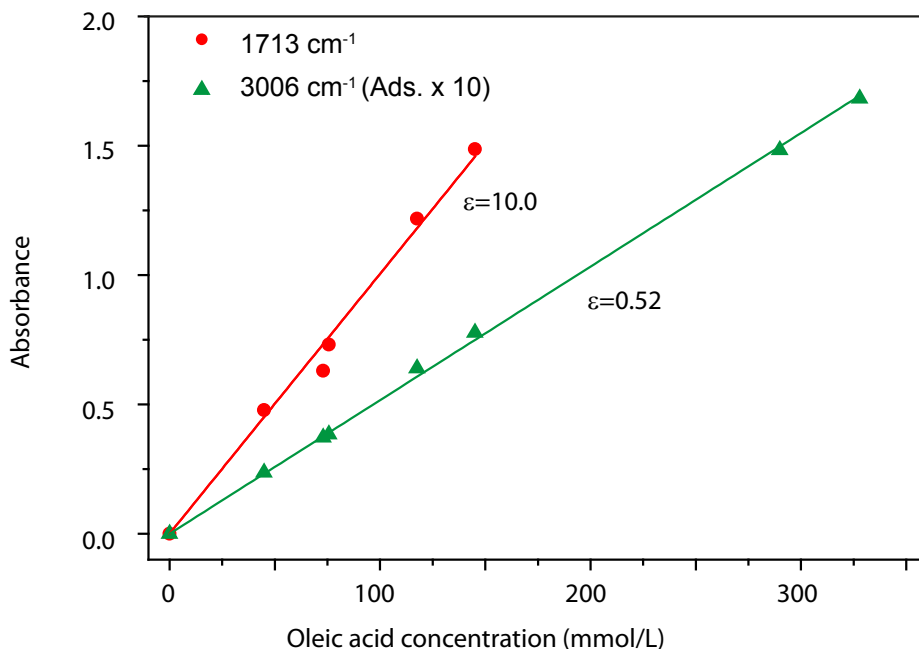


FIGURE 7.9. Absorbance of oleic acid dissolved in cyclohexane for the peaks corresponding to the total ( $3006\text{ cm}^{-1}$ ) and free oleic acid ( $1713\text{ cm}^{-1}$ ) plotted as function of oleic acid concentration; the corresponding extinction coefficients  $\epsilon$  are given.

In a recent paper by Cass et al. [12] similar features are reported for PbSe as shown here for magnetite and are interpreted as the presence of chelating and bridging complexes.

In the region between  $1450\text{ cm}^{-1}$  and  $500\text{ cm}^{-1}$ , the iron oxide band at  $603\text{ cm}^{-1}$  is clearly present. Furthermore, unidentified peaks are present in the PbSe nanoparticle spectrum at  $1259\text{ cm}^{-1}$ ,  $1116\text{ cm}^{-1}$ ,  $1012\text{ cm}^{-1}$ , and  $806\text{ cm}^{-1}$ , probably traces of chemicals from particle synthesis or sample preparation.

The adsorption isotherms of oleic acid on magnetite and PbSe are obtained from IR spectra recorded of samples with fixed nanoparticle concentration and varying oleic acid concentrations. The peak at  $3006\text{ cm}^{-1}$  which corresponds to the CH vibration next to the double bond in the tail of the ligand [11, 31, 32], is not influenced by the complex formation with the nanoparticle and therefore can be used as an internal reference for the total oleic acid concentration. The

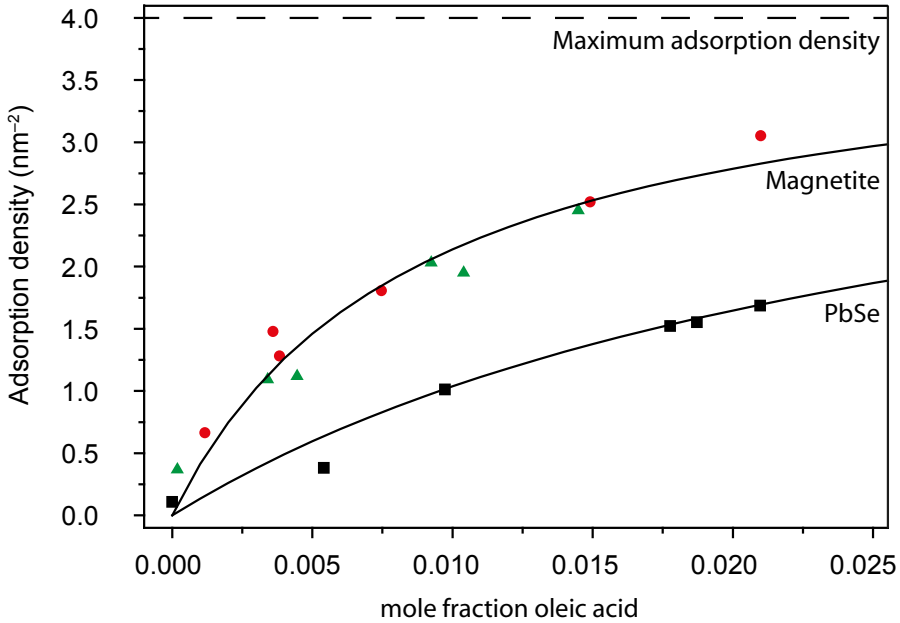


FIGURE 7.10. Adsorption isotherms of oleic acid on magnetite prepared via the high temperature decomposition method (circles) or aqueous co-precipitation method (triangles) and PbSe (squares); the solid lines are fits with the Langmuir isotherm (eq. 7.2) and the dashed line represents the maximum adsorption density as obtained from the fits, within error the same in both cases. A mole fraction of 0.025 corresponds to a 250 mmol/L oleic acid solution.

concentration of unbound oleic acid molecules can be determined from the peak at  $1713\text{ cm}^{-1}$ , which corresponds to the aprotic dimer [11, 31]. In fig. 7.9, the absorbances of these peaks are plotted as function of the concentration in pure oleic acid solutions without nanoparticles, and the extinction coefficient is obtained from the slope of these plots.

The adsorption of ligands on the surface of the nanoparticles is described using the Langmuir isotherm [37]:

$$(7.2) \quad K = \exp(-\Delta F/k_B T) = \frac{\theta_B}{x_F(1 - \theta_B)}$$

where  $K$  is the equilibrium constant, related to the binding free energy  $\Delta F$ ,  $k_B T$  is the thermal energy,  $\theta_B$  is the fraction of the nanoparticle surface covered with ligands, and  $x_F$  is the mole fraction of the free ligands in solution. The surface fraction is defined as:

$$(7.3) \quad \theta = \frac{C_B}{C_{NP} A \Gamma}$$

where  $C_B$  is the concentration of ligands bound to the quantum dot surface,  $C_{NP}$  the concentration of nanoparticles,  $A$  the surface area of a quantum dot, and  $\Gamma$  the maximum adsorption density of the ligands. In fig. 7.10 the adsorption isotherms are shown for magnetite and PbSe. The solid lines are fits based on the Langmuir isotherm, from which the maximum adsorption density and the equilibrium constant are obtained. For magnetite the equilibrium constant is 115, corresponding to an adsorption free energy of  $-12$  kJ/mol. No difference is observed between the two magnetite batches, indicating that the surface of the nanoparticles was similar for both synthesis routes. The measured adsorption free energy agrees well with previous studies [14, 35] and also the maximum adsorption density is in good agreement [14, 38]. In our case, we do not observe the strong binding sites as found by Klokkenburg et al. [14] and Dubois et al. [38]. The agreement of our results with previous data obtained for magnetite proves that our method to measure the adsorption isotherms is reliable and can be used to obtain the adsorption isotherm for other materials as well.

For PbSe,  $K$  equals 35, which corresponds to an adsorption free energy of  $-9$  kJ/mol. Qualitatively, the difference in adsorption free energy compared to magnetite can be understood from a Lewis acid-base reaction model; oleic acid is a hard Lewis base, which would bind more strongly to strong Lewis acids, such as  $\text{Fe}^{3+}$ , than to weak Lewis acids such as  $\text{Fe}^{2+}$  and  $\text{Pb}^{2+}$  [39].

The maximum adsorption density of oleic acid is similar for magnetite and PbSe nanoparticles, namely  $4 \text{ nm}^{-2}$ . The maximum adsorption density can be determined by two factors: the number of binding sites or steric interactions between the ligands themselves. For PbSe, the highest number density of cation sites, and therefore the maximum possible adsorption density, is present on fully lead terminated 111 facets. Using the lattice constant of the rock-salt crystal lattice of PbSe ( $0.612 \text{ nm}$ ), the density of  $\text{Pb}^{2+}$  ions on these facets is  $8 \text{ nm}^{-2}$ , much higher than the experimentally determined maximum adsorption density of oleic acid molecules. Also for the 100 facets, which are a mixture of lead and selenium ions the density of lead ions is  $5 \text{ nm}^{-2}$ , still higher than the maximum adsorption

---



density observed. In the sterically limited case, the maximum adsorption density can be estimated by the number of oleic acid molecules in a volume with an area of  $1 \text{ nm}^2$  and a thickness of the oleic acid length of  $2 \text{ nm}$ . Using the room temperature density ( $0.895 \text{ g/mL}$ ), an adsorption density of  $3.8 \text{ nm}^{-2}$  is calculated, in good agreement with the experimental values.

These calculations indicate that the maximum adsorption density is determined by the steric interactions between the ligand molecules themselves rather than limited by the number of binding sites on the nanoparticle. Comparing the experimental adsorption density with the maximum cation density of the PbSe 111 planes reveal that only 50% of the cations sites can be capped with the ligands. As all cation sites have a positive charge, those 111 facets would be strongly charged and have a great influence on the colloidal interactions as discussed in chapters 2 and 4. However, purely lead terminated crystal facets are highly unfavorable [40] due to their high charge density and the free energy of these facets is lowered by adsorbing either ligands or selenium ions or these crystal facets are eliminated via a step-like arrangement of 100 facets [41]. As ligands can only compensate the charge of a fraction of the Pb-ions at the surface, it is likely that another part of the net charge of these interfaces is compensated by selenium ions, such that only a limited number of net charges on each facet might remain.

#### 4. Conclusions

In the first part of this chapter, it is shown that the photoluminescence quantum yield of dispersions of CdTe capped with dodecylamine and octadecylamine increases over time after dilution of the initial stock dispersion by a factor of 100. CdTe quantum dots capped with dodecylamine or octadecylamine show photobrightening when illuminated but only the dodecylamine-capped quantum dots show photoluminescence brightening when stored in the dark. It is shown that the equilibration time of the DDA ligand layer as obtained from in situ IR measurements is in reasonable agreement with the short equilibration time of the luminescence increase, suggesting that both are due to the same process. The liquid-like state of the DDA ligands allows for response to the changes in concentration upon dilution, and high energy surface states can be eliminated via surface reconstruction. For CdTe quantum dots capped with octadecylamine, the ligand layer cannot respond to the change in concentration and surface reconstruction is much slower, although this has been confirmed via infrared spectroscopy.

---

The second part of this chapter concerns the adsorption of ligands on magnetite and PbSe nanoparticles. It is shown that oleic acid adsorbs more strongly to magnetite than to PbSe, which is in agreement with the harder Lewis acidity of  $\text{Fe}^{3+}$  with respect to that of  $\text{Pb}^{2+}$ . The maximum adsorption density is the same for both PbSe and magnetite nanoparticles, and it is determined by the steric repulsion between the ligands, rather than the number of binding sites on the surface of the nanoparticle. This implies that on the surface of a PbSe nano-crystal, a fraction of the  $\text{Pb}^{2+}$  ions is uncapped which can contribute to the colloidal interactions between the nanoparticles.

### Bibliography

- [1] C. de Mello Donegá. Synthesis and properties of colloidal heteronanocrystals. *Chem. Soc. Rev.*, 40(3):1512–46, 2011.
  - [2] X. Peng, L. Manna, W. Yang, J. Wickham, E. Scher, A. Kadavanich, and A. P. Alivisatos. Shape control of CdSe nanocrystals. *Nature*, 404(6773): 59–61, 2000.
  - [3] A. Dubavik, V. Lesnyak, W. Thiessen, N. Gaponik, T. Wolff, and A. Eychmüller. Synthesis of amphiphilic CdTe nanocrystals. *J. Phys. Chem. C*, 113(12):4748–4750, 2009.
  - [4] Y. Tanaka, S. Saita, and S. Maenosono. Influence of surface ligands on saturation magnetization of FePt nanoparticles. *App. Phys. Lett.*, 92(9):093117, 2008.
  - [5] N. Pradhan, D. Reifsnnyder, R. Xie, J. Aldana, and X. Peng. Surface ligand dynamics in growth of nanocrystals. *J. Am. Chem. Soc.*, 129(30):9500–9, 2007.
  - [6] I. L. Medintz, H. Mattoussi, and A. R. Clapp. Potential clinical applications of quantum dots. *Int. J. Nanomedicine*, 3:151–67, 2008.
  - [7] R. Koole, P. Schapotschnikow, C. De Mello Donegá, T. J. H. Vlugt, and A. Meijerink. Time-dependent photoluminescence spectroscopy as a tool to measure the ligand exchange kinetics on a quantum dot surface. *ACS Nano*, 2(8):1703–14, 2008.
  - [8] S. F. Wuister, A. van Houselt, C. de Mello Donegá, D. Vanmaekelbergh, and A. Meijerink. Temperature anti-quenching of the luminescence from capped CdSe quantum dots. *Angew. Chem. Int. ed.*, 43(23):3029–33, 2004.
  - [9] B. Fritzing, I. Moreels, P. Lommens, R. Koole, Z. Hens, and J. Martins. In situ observation of rapid ligand exchange in colloidal nanocrystal suspensions
-

- using transfer NOE nuclear magnetic resonance spectroscopy. *J. Am. Chem. Soc.*, 131(8):3024–3032, 2009.
- [10] J. K. Cooper, A. M. Franco, S. Gul, C. Corrado, and J. Z. Zhang. Characterization of primary amine capped CdSe, ZnSe, and ZnS quantum dots by FT-IR: determination of surface bonding interaction and identification of selective desorption. *Langmuir*, 27(13):8486–93, 2011.
- [11] D. H. Lee and R. A. Condrate. FTIR spectral characterization of thin film coatings of oleic acid on glasses: I. coatings on glasses from ethyl alcohol. *J. Mat. Sci.*, 4:139–146, 1999.
- [12] L. C. Cass, M. Malicki, and E. A. Weiss. The chemical environments of oleate species within samples of oleate-coated PbS quantum dots. *Anal. Chem.*, 85(13):6974–6979, 2013. doi: 10.1021/ac401623a.
- [13] K. Nakamoto. *Infrared and Raman spectra of inorganic and coordination compounds*. Wiley, 1978. ISBN 9780471744931.
- [14] M. Klokkenburg, J. Hilhorst, and B. H. Ern e. Surface analysis of magnetite nanoparticles in cyclohexane solutions of oleic acid and oleylamine. *Vibr. Spectr.*, 43(1):243–248, 2007.
- [15] B. H. Ern e, E. van den Pol, G. J. Vroege, T. Visser, and H. H. Wensink. Size fractionation in a phase-separated colloidal fluid. *Langmuir*, 21(5):1802–1805, 2005.
- [16] B. H. Ern e, J. H. van der Maas, B. W. M. Kuipers, T. Visser, and A. P. Philipse. Vertical concentration profiles in colloidal fluids measured by FTIR-ATR spectroscopy. *Langmuir*, 19(11):3081–3083, 2003.
- [17] S. F. Wuister, C. de Mello Doneg a, and A. Meijerink. Luminescence temperature anti-quenching of water-soluble CdTe quantum dots: role of the solvent. *J. Am. Chem. Soc.*, 126(33):10397–10402, 2004.
- [18] M. V. Kovalenko, D. V. Talapin, M. A. Loi, F. Cordella, G. Hesser, M. I. Bodnarchuk, and W. Heiss. Quasi-seeded growth of ligand-tailored pbse nanocrystals through cation-exchange-mediated nucleation. *Angew. Chem. Int. ed.*, 47(16):3029–33, 2008.
- [19] B. Luigjes, S. M. C. Woudenberg, R. de Groot, J. D. Meeldijk, H. M. Torres Galvis, K. P. de Jong, A. P. Philipse, and B. H. Ern e. Diverging geometric and magnetic size distributions of iron oxide nanocrystals. *J. Phys. Chem. C*, 115:14598–14605, 2011.
- [20] D. Bica. Preparation of magnetic fluids for various applications. *Rom. Rep. Phys.*, 47(3-5):265, 1995.
-

- [21] W. Brown. *Dynamic light scattering: the method and some applications*. Clarendon Press, Oxford, 1993.
  - [22] C. Carrillo-Carrión, S. Cárdenas, B. M. Simonet, and M. Valcárcel. Quantum dots luminescence enhancement due to illumination with uv/vis light. *Chem. Commun.*, (35):5214–26, 2009.
  - [23] Y. Wang, Z. Tang, M. A. Correa-Duarte, I. Pastoriza-Santos, M. Giersig, N. A. Kotov, and L. M. Liz-Marza. Mechanism of strong luminescence photoactivation of citrate-stabilized water-soluble nanoparticles with CdSe cores. *J. Phys. Chem. B*, 108:15461–15469, 2004.
  - [24] J. J. Peterson and T. D. Krauss. Photobrightening and photodarkening in PbS quantum dots. *Phys. Chem. Chem. Phys.*, 8(33):3851, 2006.
  - [25] D. V. Talapin, A. L. Rogach, E. V. Shevchenko, A. Kornowski, M. Haase, and H. Weller. Dynamic distribution of growth rates within the ensembles of colloidal II-VI and III-V semiconductor nanocrystals as a factor governing their photoluminescence efficiency. *J. Am. Chem. Soc.*, 124(20):5782–90, 2002.
  - [26] E. Groeneveld. *Synthesis and optical spectroscopy of hetero-nanocrystals*. PhD Thesis, Utrecht University, 2012.
  - [27] M. Jones, J. Nedeljkovic, R. J. Ellingson, A. J. Nozik, and G. Rumbles. Photoenhancement of luminescence in colloidal CdSe quantum dot solutions. *J. Phys. Chem. B*, 107(41):11346–11352, 2003.
  - [28] Z. Zhelev, R. Jose, T. Nagase, H. Ohba, R. Bakalova, M. Ishikawa, and Y. Baba. Enhancement of the photoluminescence of CdSe quantum dots during long-term uv-irradiation: privilege or fault in life science research? *J. Photochem. and Photobio. B*, 75(1-2):99–105, 2004.
  - [29] K. Leung and K. B. Whaley. Surface relaxation in cdse nanocrystals. *J. Chem. Phys.*, 110(22):11012, 1999.
  - [30] R. Sokoll and H. Hobert. Infrared study of the adsorption of octadecylamine at the MgO/CCl<sub>4</sub> interface. *J. Chem. Soc., Faraday Trans.*, 1(82):1527–1535, 1986.
  - [31] P. J. Thistlethwaite, M. L. Gee, and D. Wilson. Diffuse reflectance infrared fourier transform spectroscopic studies of the adsorption of oleate/oleic acid onto zirconia. *Langmuir*, 12(10):6487–6491, 1996.
  - [32] N. Shukla, C. Liu, P. M. Jones, and D. Weller. FTIR study of surfactant bonding to FePt nanoparticles. *J. Magn. Magn. Mat.*, 266(1-2):178–184, 2003.
  - [33] J. A. Mielczarski, J. M. Cases, P. Tekely, and D. Canet. structure of adsorption layer on apatite contacted with oleate solutions. 2. In situ and ex
-

- situ fourier transform infrared, NMR, and x-ray photoelectron spectroscopy. *Langmuir*, pages 3357–3370, 1993.
- [34] Y. Hou, H. Kondoh, M. Shimojo, E. O. Sako, N. Ozaki, T. Kogure, and T. Ohta. Inorganic nanocrystal self-assembly via the inclusion interaction of beta-cyclodextrins: toward 3D spherical magnetite. *J. Phys. Chem. B*, 109(11):4845–4852, 2005.
- [35] V. V. Korolev, A. G. Ramazanova, and A. V. Blinov. Adsorption of surfactants on superfine magnetite. *Rus. Chem. Bull.*, 51(11):2044–2049, 2002.
- [36] B. Gržeta, M. Ristić, I. Nowik, and S. Musić. Formation of nanocrystalline magnetite by thermal decomposition of iron choline citrate. *J. All. Comp.*, 334:304–312, 2002.
- [37] R. J. Hunter. *Introduction to modern colloid science*. Oxford University Press, 1st edition, 1993. ISBN 0198553862.
- [38] E. Dubois, V. Cabuil, F. Boué, and R. Perzynski. Structural analogy between aqueous and oily magnetic fluids. *J. Chem. Phys.*, 111(15):7147, 1999.
- [39] R. G. Pearson. Hard and soft acids and bases. *J. Am. Chem. Soc.*, 265(3):3533–3539, 1963.
- [40] C. Fang, M. A. van Huis, D. Vanmaekelbergh, and H. W. Zandbergen. Energetics of polar and nonpolar facets of PbSe nanocrystals from theory and experiment. *ACS Nano*, 4(1):211–8, 2010.
- [41] P. Schapotschnikow, M. A. van Huis, H. W. Zandbergen, D. Vanmaekelbergh, and T. J. H. Vlugt. Morphological transformations and fusion of PbSe nanocrystals studied using atomistic simulations. *Nano Lett.*, 10(10):3966–71, 2010.
-



## Summary

In this thesis, the main topic is the interactions of nanoparticles in apolar liquids. These includes both the colloidal interactions between nanoparticles and the interaction of the nanoparticles with an external potential from a liquid/air interface or a magnetic field. The understanding of these interactions would allow for better understanding of their colloidal properties, for instance the formation of self-assembled superlattices.

In **chapter 1** a short overview of colloidal interactions between nanoparticles is presented and their interaction energy is estimated. Furthermore, the use of cryogenic transmission electron microscopy (cryo-TEM) to visualize dispersions on the nanometer scale and the influence of the environment on sample preparation are discussed. To image the dispersion in three dimensions, electron tomography is used, as explained in the last part of the chapter.

Colloidal semiconductor nanoparticles, the so-called quantum dots, are known to form equilibrium clusters in liquid dispersions due to colloidal interactions, and these clusters are the topic of **chapter 2**. From quantitative analysis of cryo-TEM images, the surface fractions of the clusters are measured for clusters with different numbers of particles and varying morphologies. From these surface fractions, the particle coupling free energy is determined as a function of temperature and quantum dot size. From the temperature dependence of the coupling free energy, the entropic and enthalpic parts of the interaction free energy are separated using Van 't Hoff's equation. The enthalpic component corresponds to the magnitude of the contact interaction, crucial information in understanding the energetics of the self-assembly of nanoparticles into ordered structures.

In the cryo-TEM experiments, the nanoparticles are dispersed in a thin liquid film with a thickness of only about ten times the particle diameter; as a result, the interfaces can have a strong influence on the distribution of the nanoparticles. In **chapter 3** the three-dimensional distribution of nanoparticles at the liquid/air interface is imaged by cryogenic electron tomography. Depending on the surface

tension of the liquid, the particles either (a) strongly adsorb to the interface, (b) show an equilibrium distribution between the interface and the bulk of the liquid, or (c) are fully immersed in the bulk liquid. The conventional method to investigate the adsorption of molecules at liquid interfaces is the measurement of the macroscopic interfacial tension as function of concentration; however in the case of quantum dots, it does not reveal the adsorption-desorption transition but instead indicates an adsorption density that is much higher than a single monolayer of nanoparticles. This is due to the presence of free lead oleate, a surface active species related to the capping ligands of the nanoparticles.

A well-known method to quantify interactions for both molecules and colloids is the determination of the second virial coefficient ( $B_2$ ), which we use in **chapter 4** to compare the results obtained by cryo-TEM, small angle X-ray scattering, and analytical centrifugation, which within error yield similar values of  $B_2$ . For particles smaller than 5.5 nm, a positive  $B_2$  is found, showing that the repulsion between capping layers is the dominant interaction, while negative virial coefficients are measured for the larger particles due to the increasing attractions of the nanoparticles. The size dependence of the second virial coefficient is fitted with a dipolar hard sphere model, and the obtained interaction parameters are compared with the measured coupling free energies from the analysis in chapter 2.

Another way to quantify the interactions of nanoparticles is to study their response to an external field; for example, the measurement of the magnetization curve for magnetic nanoparticles. In **chapter 5**, a non-regularized inversion method is applied to the analysis of magnetization curves of ferrofluids. With this method, originally used for the analysis of static light scattering measurements, the magnetic size distribution is determined from an experimental magnetization curve without prior knowledge of the shape of the size distribution derived for example from TEM. The applicability of this method is demonstrated using magnetite dispersions with a known size distribution, as well as simulated magnetization curves. In this way the magnetic size distribution is obtained directly from the magnetization curves and is less model-dependent than when the shape of the distribution is assumed from the start.

Knowledge of the interactions between nanoparticles is especially important for the self-assembly of these nanoparticles into superlattices. In **Chapter 6** this self-assembly is explored for a system containing magnetic cobalt nanoparticles and PbSe quantum dots, which form superlattices with a AIB<sub>2</sub> type structure on an ethylene glycol interface. When these assemblies are prepared in the presence

---



---

of a magnetic field, the cobalt nanoparticles align with the field, which results in the formation of anisotropic binary superlattices still with the  $\text{AlB}_2$  type internal structure. For the formation of these superlattices, high quality monodisperse nanoparticles are required. A minimalistic new method is presented for the synthesis of monodisperse cobalt nanoparticles, based on the well known decomposition of dicobalt-octacarbonyl now performed in a glass test tube as reaction vessel. The large surface-to-volume ratio of the test tube allows for efficient heating of the reaction mixture, which makes this method rapid and robust. This method is demonstrated by investigating the influence of the solvent and capping ligands on the formation of the nanoparticles.

In **chapter 7**, infrared spectroscopy is used to study the adsorption of ligands on the surface of nanoparticles. The first part of this chapter deals with the correlation between ligand adsorption and the observed increase of the photoluminescence upon dilution of the dispersion. It is shown that the typical time scale of the increase in luminescence corresponds to the time scale on which the capping density of the nanoparticles changes after dilution. In the second part of the chapter, the adsorption isotherm of oleic acid on PbSe quantum dots is measured. To compare our results with previous methods, the adsorption isotherm of oleic acid on magnetite is taken as a reference. It is shown that oleic acid binds much more strongly to magnetite than to PbSe; however, the maximum adsorption density is similar for both nanoparticles. This similarity indicates that the maximum adsorption density is determined by the size of the ligand molecules rather than the atomic structure of the nanoparticle.

In conclusion, it is shown in this thesis that cryo-TEM is a very suitable method to study the interactions of nanoparticles in liquid media. The thus determined thermodynamic interaction parameters of colloidal nanoparticles in apolar solvent agree well with those obtained via other methods. Not only the interactions between the nanoparticles but also the interaction of the nanoparticles with the liquid/air interface was revealed by cryo-TEM, an interaction that was masked by other surface active species when studied with macroscopic surface tension measurements. It is shown that the ligands that are reversibly adsorbed on the nanoparticle surface have a significant influence on the interactions between the nanoparticles, especially for the smaller particles. For the larger nanoparticles, the interactions of the core of the particles become dominant.

---



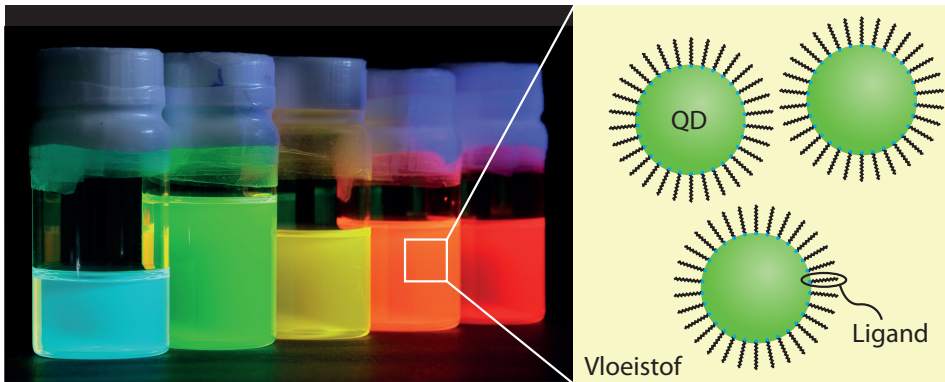
# Samenvatting in het Nederlands

De titel van dit proefschrift bestaat uit drie kernbegrippen namelijk: quantum dots, apolaire vloeistoffen en colloïdale wisselwerkingen. Voor het begrijpen van deze begrippen uit dit proefschrift worden deze hierna kort geïntroduceerd. Daarna worden de onderwerpen van de hoofdstukken kort uitgelegd.

## 1. Quantum dots

In de meeste gevallen zijn de materiaal eigenschappen van een voorwerp onafhankelijk van de vorm. Bijvoorbeeld, goud verandert niet van kleur als je er een ring van maakt maar is altijd geel en glimmend. Dit verandert als we de voorwerpen kleiner en kleiner gaan maken, en er zogenaamde nanodeeltjes van maken. Deze nanodeeltjes zijn voorwerpen met een grootte tussen ongeveer 100 en 1 nm, ongeveer 10.000 tot 1.000.000 keer kleiner dan een millimeter. Als we kleine goudbolletjes maken van deze grootte valt het op dat de kleur verandert van geel naar blauw voor bolletjes met een diameter van 150 nm en zelfs rood voor bolletjes met een diameter van 5 nm. Dit effect was al bekend bij de Romeinen die dit gebruikten om gekleurd glas te maken. Zo was bekend dat glas een rode kleur kreeg door goud toe te voegen tijdens het smelten.

Niet alleen goud heeft dit verschijnsel maar veel materialen kennen dit. In dit hoofdstuk worden nanodeeltjes van het materiaal lood-selenide gebruikt, een halfgeleider materiaal dat licht kan absorberen, en vervolgens licht van een specifieke kleur weer uitzend (emitteren). Dit soort halfgeleider nanodeeltjes worden ook wel quantum dots genoemd. De invloed van de grootte van deze deeltjes is voor halfgeleider deeltjes niet alleen zichtbaar in de kleur, maar ook in de kleur van het uitgezonden licht. Hoe kleiner de deeltjes hoe blauwer de kleur van het geëmitteerde licht, terwijl grotere deeltjes een meer rode kleur hebben (zie figuur 1). In het geval van lood-selenide quantum dots is het emissie licht in het infrarood, en dus altijd onzichtbaar voor ons oog maar ook hier wordt de energie van het geëmitteerde infrarode licht bepaald door de grootte van de deeltjes.



FIGUUR 1. Links: een foto van CdSe quantum dots met van links naar rechts een diameter variërend van 1.7 nm tot 4.5 nm. Rechts: Schematische weergave van de QDs in de vloeistof. De foto is beschikbaar gesteld door Mark Vis.

## 2. Apolaire vloeistoffen

De quantum dots die bestudeerd worden in dit proefschrift zijn zogenaamde colloïdale quantum dots. De toevoeging ‘colloïdale’ betekend dat de quantum dots gedispergeerd zijn in een vloeistof zoals schematisch weergegeven in figuur 1. Deze vloeistof kan zowel water, een ‘polaire’ vloeistof zijn maar ook een ‘benzine’-achtige vloeistof, wat we een apolaire vloeistof noemen. Welke vloeistof wordt gebruikt is van belang voor de wisselwerkingen tussen de deeltjes. In de vloeistof hebben de quantum dots altijd de neiging om aan elkaar te plakken. Daarom moet er altijd een tegenwerkende kracht zijn die de deeltjes uit elkaar houdt. In ons geval zijn de deeltjes bedekt met een laag ‘zeep’ moleculen, de zogenaamde liganden, die als een soort borstels de deeltjes uit elkaar duwen.

Kort gezegd bestaan er twee methoden om deze quantum dots en andere nanodeeltjes te maken, namelijk door het opbreken van grotere objecten in steeds kleinere fragmenten of door het opbouwen van de nanodeeltjes vanuit losse atomen. Deze laatste procedure is flexibeler en geeft over het algemeen betere kwaliteit nanodeeltjes dan de eerste methode. Deze methode is gebruikt voor de synthese van de nanodeeltjes bestudeerd in dit proefschrift. De vorming van de quantum dots via deze methode kan worden verdeeld in drie stappen. In de eerste stap worden de bouwstenen voor de nanodeeltjes gevormd door het uit elkaar laten vallen van grotere moleculen. In de tweede stap vormen deze bouwstenen kleine clusters

die vervolgens uitgroeien tot nanodeeltjes van de gewenste grootte. Dit proces gebeurt in de aanwezigheid van de liganden die de nieuwgevormde nanodeeltjes beschermen.

### 3. Colloïdale wisselwerkingen

**3.1. Tussen de nanodeeltjes.** De focus van dit proefschrift is het bestuderen van de colloïdale wisselwerkingen tussen de deeltjes. Bij deze wisselwerkingen gaat het om de beïnvloeding van het gedrag van deze deeltjes in de vloeistof door de aanwezigheid van andere nanodeeltjes. Bijvoorbeeld, een veelgebruikt model voor deze wisselwerkingen is de zogenaamde harde bollen wisselwerking. Dit is dezelfde manier waarop knikkers zich gedragen; zodra de knikkers elkaar niet raken kan een van de knikkers zonder moeite bewogen worden zonder dat de andere knikker daar iets van merkt. Dit is duidelijk anders voor magnetische of statische wisselwerkingen. Als de knikkers bijvoorbeeld magnetisch waren, zouden de knikkers vanzelf naar elkaar toe rollen als ze dicht bij elkaar waren. Als een van de knikkers daarna bewogen wordt beweegt de andere mee. Dezelfde wisselwerkingen treden ook op bij de kleine nanodeeltjes bestudeerd in dit proefschrift. Alleen doordat er honderden tot duizenden deeltjes elkaar beïnvloeden is het resultaat lang niet altijd zo voorspelbaar als in het geval van enkele knikkers of magneten.

**3.2. Van de nanodeeltjes en hun omgeving.** Naast wisselwerkingen tussen de deeltjes gaat het in dit proefschrift ook over de wisselwerkingen van quantum dots met hun omgeving, bijvoorbeeld een magnetisch veld of een vloeistof oppervlak.

Bij de wisselwerking met een vloeistof oppervlak kijken we of de nanodeeltjes in de buurt van het oppervlak willen blijven of juist er vandaan willen. In de macroscopische wereld is het vooral de massa van een object dat bepaald of iets blijft drijven of niet, hoewel de uitzonderingen al merkbaar zijn bij bijvoorbeeld watervlooiën of paperclips. Een paperclip is zwaarder dan water en zou dus moeten zinken, maar als je de paperclip voorzichtig op het water legt blijft hij juist drijven. Dit wordt veroorzaakt doordat het water oppervlak vervormt en werkt als een soort veer die de paperclip terug duwt. Zolang de veerkracht groot genoeg is om de paperclip te dragen blijft deze drijven. Deze veerkracht wordt de oppervlakte spanning genoemd. Zodra een kleine druppel zeep aan het water wordt toegevoegd waarop de paperclip drijft zal deze alsnog zinken doordat de zeep de veerkracht van het water vermindert. Ditzelfde gebeurt op de kleine schaal van de quantum dots, waar het de oppervlakte spanning is die bepaald of de quantum

---

dots bij het oppervlak willen blijven, bij een hoge grensvlakspanning, of bij een lage grensvlakspanning juist niet bij het oppervlak blijven.

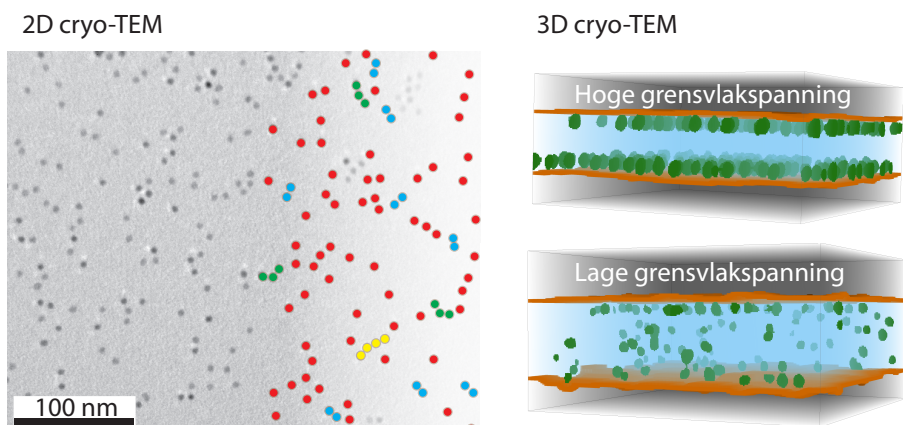
#### **4. Colloïdale wisselwerkingen van quantum dots in apolaire vloeistoffen**

Wat is nu het eigenlijke onderwerp van dit proefschrift? Het bestuderen van de wisselwerkingen tussen de deeltjes was tot nu toe vooral indirect zodat de wisselwerkingen moesten worden afgeleid van de gezamenlijke eigenschappen van heel veel (typisch honderden miljarden) losse deeltjes. Dit was net zoals het schudden aan een dichte doos om te onderzoeken of er magneten of knikkers inzitten omdat die op een andere manier rammelen. Dit gaat goed zolang het of alleen maar magneten of alleen maar knikkers zijn maar zodra het een combinatie van beide is, wordt dit lastig. Het mooiste is natuurlijk als je de doos open kunt doen en zien wat voor deeltjes er nu in de doos zitten. Dit is precies wat we in de eerste hoofdstukken van dit proefschrift doen.

Omdat de quantum dots die hier gebruikt zijn zo klein zijn is het niet mogelijk om deze met een gewone licht microscoop te bekijken maar is een zogenaamde elektronen microscoop nodig die heel nauwkeurige beelden kan maken. Het grote nadeel van deze microscoop is dat de elektronen in een heel sterk vacuüm moeten blijven om een scherp beeld te vormen en dat daardoor alle vloeistoffen heel snel verdampen als ze in de microscoop worden geplaatst. Hier hebben wij een biologische techniek (cryogene transmissie elektronen microscopie, cryo-TEM) onderzocht die dit probleem omzeilde door de monsters vooraf heel snel in te vriezen, zo snel dat je ervan uit kunt gaan dat de structuur van het monster in die tijd niet veranderd. Als zo'n monster dan in de microscoop wordt geplaatst is het net of je naar een foto kijkt van de vloeistof zoals die was voor het invriezen. Voor dit onderzoek zijn op deze manier foto's gemaakt van dunne films van de vloeistof met daarin de deeltjes, films die ongeveer tien keer dikker zijn dan de deeltjes zelf.

In het tweede hoofdstuk van dit proefschrift laten we zien dat aan de hand van deze foto's de wisselwerkingen van de deeltjes kunnen worden bestudeerd. We zagen bijvoorbeeld dat de deeltjes zich gedragen als magneetjes omdat ze vooral in korte lijntjes aan elkaar plakken (zie figuur 2) en uit de lengtes van deze ketentjes kon uitgerekend worden hoe sterk deze wisselwerking was. Door dit proces te herhalen bij verschillende temperaturen, hebben we laten zien dat de fundamentele wetten die moleculaire reacties beschrijven ook opgingen voor onze nanodeeltjes.

---



FIGUUR 2. Links: Standaard 2D cryo-TEM afbeelding. Aan de linker kant zijn de verschillende ketentjes weergegeven in het rood voor losse deeltjes, blauw voor ketens van twee deeltjes, groen voor drie deeltjes en geel voor vier deeltjes. Rechts: twee afbeelding van een drie dimensionale film met een hoge (boven) en een lage (onder) grensvlakspanning. Het is duidelijk te zien dat de deeltjes een voorkeur hebben voor een oppervlak met een hoge grensvlak spanning.

Voor het tweede hoofdstuk is gebruik gemaakt van twee dimensionale afbeeldingen van de vloeistoflaag, in werkelijkheid kunnen de deeltjes ook op verschillende hoogten in de film zitten. In het derde hoofdstuk wordt gekeken naar deze drie-dimensionale verdeling van de deeltjes en vooral naar de verdeling van de afstand van het deeltje tot het vloeistof oppervlak. Net zoals de paperclip soms bleef drijven en in andere gevallen zonk, zagen we een vergelijkbaar verschijnsel in onze systemen. Hoe sterker de veerkracht van de vloeistof hoe meer quantum dots aan het oppervlak bleven plakken; en hoe meer pentanol toegevoegd werd hoe lager de grensvlak spanning werd en hoe minder nanodeeltjes aan het oppervlak bleven plakken (zie figuur 2). Dit verschijnsel werd gecontroleerd met de gangbare techniek om deze verschijnselen te bestuderen maar met deze methode was dit niet te zien. Het blijkt dat de resultaten van deze laatste techniek sterk beïnvloed wordt door de aanwezigheid van zeep moleculen (de liganden) en dat die het effect van de quantum dots volledig bedekken.

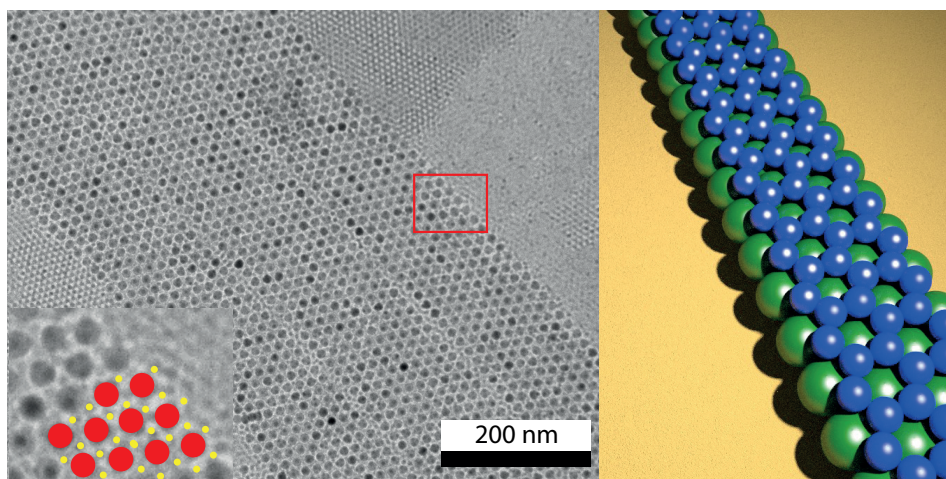
Om de resultaten van de cryo-TEM methode te controleren is het nodig om deze te vergelijken met andere experimenten. Een goede methode om dat te doen is het bepalen van de zogenaamde tweede viriaal coëfficiënt, een getal dat afhangt van de sterkte en type wisselwerkingen van de nanodeeltjes. Dit getal kan worden bepaald met röntgen verstrooiing, centrifugatie en de cryo-TEM techniek. In hoofdstuk 4 wordt de tweede viriaal coëfficiënt bepaald met deze methodes voor nanodeeltjes met verschillende groottes en de drie methodes geven allemaal dezelfde resultaten. Dit geeft aan dat ook cryo-TEM een betrouwbaar beeld geeft van de deeltjes.

In hoofdstuk vijf bestuderen we de wisselwerkingen tussen magnetische nanodeeltjes en een extern magnetisch veld. De magnetische nanodeeltjes draaien altijd in de richting van een magnetisch veld als dat sterk genoeg is. Door nu de totale richting te meten van heel veel magneetjes kan de sterkte van deze magneetjes worden berekend. In een gewoon monster met nanodeeltjes hebben de deeltjes allemaal een andere magnetische sterkte, het zogenaamde magnetisch dipool moment. Tot nu toe werd voor de berekening aangenomen dat men wist hoe de onderlinge verhouding was van de verschillende dipool momenten en hiervoor werd een wiskundige functie gebruikt. In dit hoofdstuk wordt een nieuwe methode gepresenteerd die deze aanname overbodig maakt. Hierdoor kunnen de metingen worden geanalyseerd zonder het risico dat de verkeerde wiskundige functie wordt gebruikt en het resultaat daardoor niet klopt met de werkelijkheid. Dit principe wordt gedemonstreerd door verschillende deeltjes, met een bekend dipool moment, te mengen en vervolgens vanuit de magnetische metingen de verhouding van deze deeltjes te berekenen. We laten zien dat de berekende verdeling overeen komt met de verhouding waarin de deeltjes waren gemengd.

Het doel waarvoor de wisselwerkingen tussen quantum dots worden bestudeerd is het begrijpen van de vorming van zogenaamde binaire kristallen. Net zoals gewone kristallen bestaan uit atomen op goed gedefinieerde posities, bestaan de binaire kristallen uit goed geordende structuren van nanodeeltjes, zie bijvoorbeeld figuur 3. In hoofdstuk 6 wordt eerst een methode beschreven om van het magnetische materiaal cobalt nanodeeltjes te maken met een hoge kwaliteit. Vervolgens wordt de vorming van de binaire structuren bekeken als de magnetische deeltjes worden gecombineerd met de quantum dots. Omdat de nanodeeltjes magnetisch zijn kunnen ze worden geordend in een magnetisch veld en dit wordt zichtbaar in de langgerekte vorm die de kristallen hebben.

---





FIGUUR 3. Links, een elektronen microscopie afbeelding van een binair kristal met grote kobalt nanodeeltjes en kleine lood selenide quantum dots. Links onderin is een vergroting van het gebied in de rode rechthoek waarin de deeltjes gekleurd zijn aangegeven (rood: kobalt, geel: lood selenide). Rechts is een schematische weergave te zien van de drie dimensionale structuur van een binair kristal. De blauwe PbSe kristallen omringen de groene kobalt nanodeeltjes.

In het laatste hoofdstuk wordt de vorming van de borstels op het oppervlak bestudeerd. Zoals hiervoor al uitgelegd zijn deze borstels belangrijk voor de levensduur van de nanodeeltjes. Deze borstels zitten niet permanent vast aan het oppervlak van de deeltjes maar kunnen steeds wisselen tussen vast aan het oppervlak of los in de vloeistof. Hoe sterker de binding is tussen de borstel en het oppervlak van de quantum dot, hoe langer de tijd is dat de binding blijft bestaan. In dit hoofdstuk wordt de verhouding tussen de vaste en losse borstels bestudeerd met infrarood spectroscopie. Vanuit de verhouding bij verschillende concentraties van de borstels in de vloeistof is de energie van de binding uit te rekenen.



## Dankwoord

In dit proefschrift is het onderzoek beschreven dat ik in de afgelopen vier jaar heb kunnen uitvoeren. Dit onderzoek zou nooit geworden zijn wat het is zonder de bijdrage van anderen die ik hier wil bedanken.

Als eerste wil ik mijn promotor en copromotor bedanken. Ben, als co-promotor had jij de dagelijkse leiding bij het project wat ik heb kunnen doen. Je was altijd bereid om advies te geven of de nieuwste data te bekijken. De grote vrijheid die ik van je kreeg om de dingen te onderzoeken die ik interessant vond is terug te zien in de variatie van de hoofdstukken van dit proefschrift. Ik heb deze vrijheid zeer gewaardeerd. Albert, iedere keer dat we een overleg hadden om een deel van het project te bespreken kwamen er weer nieuwe suggesties en mogelijke experimenten naar voren. Ik wil je hartelijk bedanken voor deze suggesties en adviezen die je in de afgelopen vier jaar hebt gegeven.

Aan bijna alle hoofdstukken hebben anderen een bijdrage geleverd in verschillende vormen. For example, the synthesis of the quantum dots used in this thesis was mainly carried out by Marianna Casavola or Relinde Moes, thank you for the use of the vast library of available particles. Bob Luigjes bedankt voor het gebruik van jouw voorraad aan magnetiet nanodeeltjes die door de grote variatie altijd wel een monster met de optimale grootte en polydispersiteit bevatte. Ook bedankt voor de niet werk gerelateerde gesprekken die we gevoerd hebben.

Ik heb heel veel te danken aan de hulp van de elektronen microscopie afdeling, met name Hans Meeldijk. Hans, zonder jouw expertise met cryo-TEM was veel van dit werk onmogelijk geweest. Hartelijk dank voor de vele uren die je in dit project hebt gestoken.

Veel van de experimenten in dit proefschrift zijn mogelijk gemaakt door Bonny Kuipers (H5), Jaakko Timonen (H6) en Esther Groeneveld (H7), thanks for all your contributions. Verder wil ik Andries Meijerink, Daniël Vanmaekelbergh, Celso De Mello-Donaga en Remco Tuinier nog bedanken in hun rol bij het tot stand komen van de verschillende manuscripten.

Tijdens de vier jaar promotie tijd heb ik de kans gehad om verschillende studenten te begeleiden. Veel van jullie werk is ergens terecht gekomen in dit proefschrift. Tamara Valkenburg, Marte van der Linden, Vincent Peters, Tim Gombault, Bas Salzmann, en Remco Dalebout allemaal hartelijk bedankt voor jullie bijdragen. Arnoud Onnink, ook jij bedankt voor je bijdrage aan hoofdstuk 6 hoewel je niet direct mijn student was.

Ook wil ik nog de vele collega's en oud collega's bedanken die de tijd hier in het van 't Hoff laboratorium een succes gemaakt hebben. Mijn kamergenoten Maurice Mourad, Lia Verhoeff, Julius de Folter, Joost Wolters en Chris Evers bedankt voor de gezelligheid en gesprekken. Verder wil ik Emile, Bonny, Kanvaly, Dominique en Marina voor alle ondersteuning bij het werk wat hier is gedaan. De andere labgenoten Anke, Sonja, Ping, Dima, Dzina, Agnieszka, Andrei, Gert-Jan, Henk, Hans, Mark, Mikal, Roccio, Laura, Bob, Rob, Susanne, Esther, Jan, Willem, Janne Mieke, Jan, Antara, Bas en Esther bedankt voor alles.

Ook mijn ouders en zusjes zijn tot steun geweest in de afgelopen jaren. Marijke jij bedankt voor de voorkant van dit proefschrift. Ook al was niet altijd duidelijk waar ik aan werkte, toch waren jullie altijd geïnteresseerd in wat ik deed. Dank jullie wel voor alles.

Maar boven alles gaat mijn dank uit naar de Heere God, de Schepper van alles. U gaf mij het verstand en kracht om dit werk te mogen doen.

Soli Deo Gloria

---

## List of Publications

**This thesis is partly based on the following publications:**

- J. van Rijssel, B.H. Erné, J.D. Meeldijk, M. Casavola, D. Vanmaekelbergh, A. Meijerink and A.P. Philipse, *Enthalpy and entropy of nanoparticle association from temperature-dependent cryo-TEM*, Phys. Chem. Chem. Phys., **13**, 12770-12774, (2011) (Chapter 2)
- J. van Rijssel, M. van der Linden, J.D. Meeldijk, R. van Dijk-Moes, A.P. Philipse, B.H. Erné, *Spatial distribution of nanocrystals imaged at the liquid/air interface*, Phys. Rev. Lett., **111**, 108302, (2013) (Chapter 3)
- J. van Rijssel, B.W.M. Kuipers, B.H. Erné, *Non-Regularized Inversion Method from Light Scattering Applied to Ferrofluid Magnetization Curves for Magnetic Size Distribution Analysis*, submitted, (2013) (Chapter 5)
- J. van Rijssel, B.H. Erné, A.P. Philipse, *Second Virial Coefficient of Colloidal PbSe Nanoparticles studied with Cryogenic Electron Microscopy*, in preparation (Chapter 4)
- J. Timonen, T. Gombault, J. van Rijssel, B.H. Erné, *Synthesis and Self Assembly of Cobalt Nanoparticles*, in preparation (Chapter 6)
- E. Groeneveld, A. Onnink, J. van Rijssel, B.H. Erné, C. de Mello-Donaga, A. Meijerink, *Ligand Adsorption on CdTe nanocrystals*, in preparation (Chapter 7)

**Other publications:**

- M.M. van Schooneveld, C. Campos-Cuerva, J. Pet, J.D. Meeldijk, J. van Rijssel, A. Meijerink, B.H. Ern e, F.M.F. de Groot, *Composition tunable cobalt-nickel and cobalt-iron alloy nanoparticles below 10 nm synthesized using acetonated cobalt carbonyl*, J. Nanopart. Res., **14**, 991, (2012)
  - D. Grodzinska, W.H. Evers, R. Dorland, J. van Rijssel, M.A. van Huis, A. Meijerink, C. de Mello Donega, D. Vanmaekelbergh, *Two-Fold Emission From the S-Shell of PbSe/CdSe Core/Shell Quantum Dots*, Small, **7**, 3943, (2011)
  - V.A. Vlaskin, N. Janssen, J. van Rijssel, R. Beaulac and D.R. Gamelin, *Tunable Dual Emission in Doped Semiconductor Nanocrystals*, Nano Lett., **10**, 3670-3674, (2010)
  - D. Oron, A. Aharoni, C. de Mello Donega, J. van Rijssel, A. Meijerink, U. Banin, *Universal Role of Discrete Acoustic Phonons in the Low-Temperature Optical Emission of Colloidal Quantum Dots*, Phys. Rev. Lett., **102**, 177402, (2009)
  - R. Beaulac, P.I. Archer, J. van Rijssel, A. Meijerink, and D.R. Gamelin, *Exciton Storage by Mn<sup>2+</sup> in Colloidal Mn<sup>2+</sup>-Doped CdSe Quantum Dots*, Nano Lett., **8**, 2949, (2008)
  - A.A. Verhoeff, J. van Rijssel, V.W.A. de Villeneuve and H.N.W. Lekkerkerker, *Orientation dependent Stokes drag in a colloidal liquid crystal*, Soft matter, **4**, 1602, (2008)
-

## Curriculum Vitae

Jos van Rijssel was born on the 24<sup>th</sup> of September 1986 in Utrecht, The Netherlands. In 2004 he graduated from the Van Lodenstein College in Amersfoort, and started to study Chemistry at Utrecht University. In 2007 he obtained his bachelors degree after finishing a bachelors thesis about the sedimentation of spheres in a isotropic-nematic rod system in the Van 't Hoff laboratory in Utrecht under supervision of Lia Verhoeff, Volkert de Villeneuve, and Henk Lekkerkerker. In 2007 he started his master thesis research in the condensed matter and interfaces group on the investigation of the optical properties of PbSe nanocrystals under supervision of Andries Meijerink. In 2009 he performed a 5 month internship at the University of Washington, Seattle, United States, under supervision of Daniel Gamelin. Here he investigated the temperature dependent emission of manganese doped nanocrystals. He received his masters degree cum laude in september 2009. In Oktober 2009 he started as a PhD researcher in the Van 't Hoff Laboratory for physical and colloid Chemistry under supervision of Ben Ern  and Albert Philipse. The main results of this project are presented in this thesis and were presented at several national and international conferences both as oral and poster presentations.